University of Copenhagen

Master Thesis

DARK
Niels Bohr Institute

---

# Statistics, Properties and Origin of Massive Quiescent Galaxies at High Redshifts in the IllustrisTNG Universe

---

*Author:*
Matthieu Williams

*Supervisors:*
Michaela M. Hirschmann
*Steen H. Hansen*

September 27th, 2021

# Declaration of Authorship

I, Matthieu Williams, declare that this thesis titled, "Statistics, Properties and Origin of Massive Quiescent Galaxies at High Redshifts in the IllustrisTNG Universe" and the work presented in it are my own. I confirm that:

- This work was done wholly or mainly while in candidature for a research degree at this University.
- Where any part of this thesis has previously been submitted for a degree or any other qualification at this University or any other institution, this has been clearly stated.
- Where I have consulted the published work of others, this is always clearly attributed.
- Where I have quoted from the work of others, the source is always given. With the exception of such quotations, this thesis is entirely my own work.
- I have acknowledged all main sources of help.
- Where the thesis is based on work done by myself jointly with others, I have made clear exactly what was done by others and what I have contributed myself.

Total number of pages (excl. appendices): 51

Total number of pages (incl. appendices): 55

Signed: Matthieu Williams 

Date: 27/09/2021

UNIVERSITY OF COPENHAGEN

# *Abstract*

DARK
Niels Bohr Institute

Master of Astrophysics

**Statistics, Properties and Origin of Massive Quiescent Galaxies at High Redshifts in the IllustrisTNG Universe**

by Matthieu Williams

Recent observations have found an increasingly large amount of massive galaxies which had already ceased their star formation at redshift $z = 3 - 2$ (i.e. when the universe was young, between $2.15 - 3.29\,\mathrm{Gyr}$ old), i.e. which have become quiescent. In this thesis, we investigate to what extent the modern cosmological simulation IllustrisTNG can reproduce statistics and basic properties of these observed high-$z$ massive quiescent galaxy populations. We also studied the possible physical driving mechanism for quenching star formation in these high-$z$ galaxies. When making reasonable assumptions on how to define a galaxy and its quiescence, IllustrisTNG predictions are in rough agreement with observed stellar mass functions of quiescent galaxies at $z = 2 - 3$, and observed quiescent fractions $f_{QG}$ at a given stellar mass. The TNG100-1 run is more frequently in agreement with observations than TNG300-1 run. Yet in the stellar half-mass radius-to-velocity dispersion and $f_{QG}$ planes, both simulation runs are not so consistent with observations. Taking advantage of the full assembly histories of massive quiescent galaxies at $z = 2 - 3$ in the IllustrisTNG simulation, allows us to explore the possible origin for star formation quenching at these early cosmic epochs. Our results show that the central supermassive black holes are typically seeded earlier and are growing faster in quiescent galaxies at given stellar mass, compared to the star-forming counterparts at $z = 2 - 3$. This finding indicates that feedback from accreting supermassive black holes may be one of the main drivers for suppressing star formation via heating and expelling gas in/from a galaxy. Instead, there seems to be no relevant contribution from major or minor mergers to stop star formation in these galaxies (via gas consumption due to triggering a star burst), as, however, often suggested in observational studies.

# *Acknowledgements*

We would like to start by thanking Michaela M. Hirschmann for her guidance, help and support throught out this 2020-2021 academic year. In addition, we thank the team behind IllustrisTNG simulation as this entire research rested on the use of the data files of this simulation. This study was also made possible using the multi-processing powers of Copenhagen University's HPC (High Performance Computing) system attributed to the DARK research team. Last but not least, we used Copenhagen University's ERDA (Electronic Research Data Archive) to store our results.

# Contents

**Declaration of Authorship** i

**Abstract** ii

**Acknowledgements** iii

**1 Introduction** 1
- 1.1 Observed High-$z$ Galaxies . . . 1
- 1.2 High-$z$ Surveys and Associated Telescopes . . . 2
- 1.3 Observed High-$z$ Quiescent Galaxies . . . 2
- 1.4 Properties of Observed MQGs . . . 3
  - 1.4.1 Galaxy Emission Lines . . . 3
  - 1.4.2 Galaxy Stellar Mass Functions . . . 4
  - 1.4.3 Galaxy Stellar Mass Densities . . . 4
  - 1.4.4 Galaxy Radii . . . 5
  - 1.4.5 Galaxy Stellar Velocity Dispersion . . . 5
- 1.5 Candidate Quenching Mechanisms . . . 6
- 1.6 Cosmological Galaxy Formation Simulations . . . 7

**2 IllustrisTNG Simulations** 9
- 2.1 Initial Conditions and Conventions . . . 9
- 2.2 Illustris Simulation Base . . . 10
- 2.3 Galaxy Formation Processes . . . 11
- 2.4 Galaxy Definition Criteria with IllustrisTNG . . . 13
- 2.5 Previous Results of MQGs with IllustrisTNG . . . 13

**3 Results** 15
- 3.1 Galaxy Stellar Mass Functions of IllustrisTNG Galaxies . . . 15
- 3.2 Quiescent Galaxies with IllustrisTNG . . . 18
  - 3.2.1 Quiescent Galaxy Definitions . . . 18
  - 3.2.2 Quiescent Galaxy Stellar Mass Functions . . . 23
  - 3.2.3 Quiescent Galaxy Fractions . . . 23
  - 3.2.4 Physical Properties of Quiescent Galaxies . . . 26
    - Stellar Half Mass Radii . . . 26
    - Velocity Dispersion . . . 28
    - Velocity-Size Planes . . . 29
- 3.3 Origin of Massive Quiescent at High-Redshift . . . 31
  - 3.3.1 Redshift Evolution of Galaxy Properties . . . 33
  - 3.3.2 Redshift Evolution of Black Hole Properties and Role of Black Holes . . . 34
  - 3.3.3 Role of Major and Minor Merger Events . . . 37
- 3.4 Rejuvenation of Massive Quiescent Galaxies After z=2/3 . . . 38

**4 Discussion** **41**
4.1 Different Definitions for Galaxies . . . 41
4.2 Different Criteria for Quiescence . . . 42
4.3 Origin of Mass-Size and Mass-Velocity Dispersion Relation . . . 42
4.4 Origin of Massive Quiescent Galaxies at High-Redshift . . . 43
4.5 Caveats of IllustrisTNG Simulation . . . 44
4.6 Caveats of Observational Data . . . 44
4.6.1 Observational Estimates of $SFR$ . . . 44
4.6.2 Observational Estimates of Galaxy Sizes . . . 45
4.6.3 Observational Estimates of Stellar Velocity Dispersion . . . 45
4.6.4 Observational Criteria for Quiescence Selection . . . 45

**5 Conclusion** **49**

**A Impact of Galaxy Definition** **51**

**B Galaxy Stellar Mass Distribution of $sSFR$** **53**

**Bibliography** **55**

# List of Abbreviations

| | |
|---|---|
| **AB** | **A**ll-**B**ound |
| **AGN** | **A**ctive **G**alactic **N**uclei |
| **CMB** | **C**osmic **M**icrowave **B**ackground |
| **GSMF** | **G**alaxy **S**tellar **M**ass **F**unction |
| **HDM** | **H**ot **D**ark **M**atter |
| **HLR** | **H**alf-**L**ight **R**adius |
| **IR** | **I**n-**R**adius |
| **ΛCDM** | **L**ambda **C**old **D**ark **M**atter |
| **MHD** | **M**agneto-**H**ydro-**D**ynamics |
| **MQG** | **M**assive **Q**uiescent **G**alaxy |
| **MSFS** | **M**ain **S**tar- **F**orming **S**equence (or **MS**) |
| **QAB** | **Q**uiescent **A**ll- -**B**ound |
| **QIR** | **Q**uiescent **I**n- -**R**adius |
| **QG** | **Q**uiescent **G**alaxy |
| **SFAB** | **S**tar-**F**orming **A**ll-**B**ound |
| **SED** | **S**pectral **E**nergy **D**istribution |
| **SFG** | **S**tar **F**orming **G**alaxy |
| **SFIR** | **S**tar-**F**orming **I**n-**R**adius |
| **SFR** | **S**tar **F**ormation **R**ate |
| **SHMR** | **S**tellar **H**alf-**M**ass **R**adius |
| **sSFR** | **S**pecific **S**tar **F**ormation **R**ate |

# Chapter 1

# Introduction

Cosmic inflation is a commonly accepted theory added to the standard Big Bang model, relating to one of the earliest major phases of the universe ending about $10^{-32}s$ after the Big Bang. During this extremely short epoch, the universe experiences an exponential expansion along with a significant cooling. Quantum fluctuations, prior to cosmic inflation, are thought to have been expanded by a factor of at least $10^{26}$ and resulted in over and under density structures.

Once the universe enters into its recombination era, temperatures have dropped sufficiently ($\sim 10^3$K) to allow electrons to decouple from photons, and thus combine with primordial atomic nuclei to build neutral atoms. With this decoupling of the radiation and baryonic matter, the universe starts becoming transparent to photons as they would no longer interacted with electrons. These released photons are behind the detection of the cosmic microwave background (CMB) radiation 380 000 yr after the Big Bang. From this point on, baryonic matter would be gravitationally pulled towards over densities where dark matter had already been amassed.

After the time of the CMB and as a result of self-gravity, the contrast between over dense and under dense regions intensifies. In other words, these gravitational instabilities explain why over dense areas densify with time by depleting the under dense regions. These regions then collapse producing virialised dark matter halos within which the average kinetic energy amounts to minus the half of the average potential energy.

It is within these dark matter halos that baryonic gas, trapped inside due to their gravitational potential wells, starts to cool down. As it does so, it forms dense molecular clouds which later collapse producing stars in large numbers before assembling into galaxies.

Galaxies grow in mass through continual accretion of matter and galaxy merging, two galaxies colliding and forming a larger galaxy. This leads to growth of structures and galaxies being described as hierarchical or bottom-up meaning, in the case of galaxies, smaller galaxies via galaxy merging form more and more massive galaxies (Schneider, 2015).

## 1.1 Observed High-$z$ Galaxies

Recent studies have recorded, through the recognition of a 1.47 $\mu m$-continuum break as the Lyman-$\alpha$ break (Oesch et al., 2016) and of 3 ultraviolet emission lines as CIII doublets and OIII single (Jiang et al., 2021), the highest-$z$ observed galaxy to be at $z \sim 11$ (when the universe reached its first 400Myr). Large galaxy populations have also been found to be already formed later in cosmic time as Bouwens et al., 2015 confirmed the uncovering of nearly 10400 galaxies at $4 \lesssim z \lesssim 10$, which stands to be the largest HST-detected set of high-$z$ galaxies.

## 1.2 High-$z$ Surveys and Associated Telescopes

Studies of deep high-$z$ surveys such as the MUSYC survey (Kriek et al., 2006) of the Gemini South Telescope, the Great Observatories Origins Deep Survey (GOODS, Fontana et al., 2009) from the collaboration of Hubble Space Telescope (HST) and Spitzer Space Telescope (Spitzer), the UltraVISTA survey (Muzzin et al., 2013) with the Visible and Infrared Survey Telescope for Astronomy (VISTA, Ilbert et al., 2013; Martis et al., 2016), the 3D-HST survey (Fumagalli et al., 2014; van der Wel et al., 2014) and the Cosmic Assembly Near-infrared Extragalactic Legacy Survey (CANDELS, Popping et al., 2015) of the HST (Santini et al., 2012; Bouwens et al., 2015; Barro et al., 2016; Oesch et al., 2016) and the Ultra Deep Survey (Tasca et al., 2015) from the European Southern Observatory-Very Large Telescope (ESO–VLT) have led the way to giving meaning to the particularities of galaxies and large structures of the Universe since $z \sim 10$.

This understanding has been further developed with findings from the Cosmic Evolution Survey of the COSMOS field (Domínguez Sánchez et al., 2011; Muzzin et al., 2013; van der Wel et al., 2014) viewed with the Subaru Telescope (Kajisawa et al., 2009; Ilbert et al., 2013), the Spitzer (Santini et al., 2012; Fumagalli et al., 2014) and the HST, the Sloan Digital Sky Survey (SDSS, Cheung et al., 2016)-IV with the Sloan Foundation Telescope and the installation of the Multi-Object Spectrometer for Infra-Red Exploration (MOSFIRE, Kriek et al., 2016; Belli et al., 2017; Schreiber et al., 2018; Belli et al., 2019; Tanaka et al., 2019; Valentino et al., 2020; Esdaile et al., 2021) in 2012 on the Keck I telescope (Bezanson et al., 2009; Newman et al., 2010; Belli et al., 2014). The NEWFIRM Medium-Band Survey's (NMBS), with the National Optical Astronomical Observatory, (NOAO) medium-bandwidth near-IR filters has shown high resolution improvments in the estimation of $1.5 < z < 3.5$ photometric redshifts through the determination of the 4000 Å-Balmer break (Whitaker et al., 2010). The X-Shooter Spectroscopy instrument (Vernet et al., 2011) on the VLT has played a role in the measurement of galaxy stellar dynamics and structure of high-$z$ quiescent galaxies (Tanaka et al., 2019; Stockmann et al., 2020; Valentino et al., 2020).

More concretely, among some of the results obtained through these surveys were the estimations of the scale height of the Galactic thick disk (900 parsecs) and the halo power law distribution coefficient ($-3.5$ to $-4.5$). This was achieved by MUSYC survey from the photometric properties of K (orange) dwarf stars and M (red) dwarf stars, with life expectancies along the main star-forming sequence ($MSFS$) of at least $2-3$ times that of the Sun's[1]. As well as the definite bi-modal color-color distribution of galaxies with high and low levels of star formation was proved with the SDSS survey[2] (Strateva et al., 2001). But also, van Dokkum et al., 2011, using data collected from the 3D-HST survey, showed that at $1 < z < 1.5$ ($\sim 30-40\%$ of its current age) massive ($> 10^{11} M_{\odot}$) galaxies were more diversified in terms of their detected $H\,\alpha$ emission lines, morphology and velocity dispersion than local similarly massive galaxies. CANDELS survey, on the other hand, targets objects and structures belonging to the Cosmic Dawn[3]. As such, this survey made possible the observation of the first black hole seed candidates at $z > 6$ with expected masses of at least $10^5 M_{\odot}$. They are thought to have originated from primordial clouds of atomic-cooling metal-free gas collapsing at $10 < z < 15$ (Pacucci et al., 2016).

## 1.3 Observed High-$z$ Quiescent Galaxies

Galaxies have frequently been categorized according to their associated color magnitude, mainly originating from their stellar population, in reason of the observed bi-modality of

[1] See MUSYC Results
[2] See SDSS Results
[3] See CANDELS Epochs

the global color distribution (Strateva et al., 2001; Bell et al., 2003; Budavári et al., 2003; Blanton et al., 2003; Hogg et al., 2003; Baldry et al., 2004b; Baldry et al., 2004a; Cirasuolo et al., 2007). Hotter blue stars have shorter lifespans than colder and redder counterparts making them good indicators of recent ongoing star-formation. Suppression of star formation within galaxies results in the reddening of their observed color as the relative fraction of older red stars increases and the number of short-lived blue stars diminishes. However, regions of current galaxy star formation obscured by dust, belonging to the galaxy or present along the observational line of sight, have shifted the detected galaxy color towards the reds (Kriek et al., 2006; Ilbert et al., 2013; Glazebrook et al., 2017; Santini et al., 2020). Simple UV selection has been reported to misidentify up to half of star-forming galaxies at $z > 2.5$ as dusty ones were grouped with galaxies with suppressed star formation (Muzzin et al., 2013). As it was highlighted in Martis et al., 2016, these types of star-forming galaxies dominate the massive ($\log(M) > 10.3$) galaxy population at $z > 2$.

In the local Universe it has been known, for some time, that massive blue star-forming (SFGs with high star-forming rates $SFR$) and red quiescent (QGs with low $SFR$) galaxies coexist (Tully et al., 1982; Bell et al., 2003). Recently, deeper observations have shown that this color bi-modality remains up to $z \sim 5$ (Kriek et al., 2016; Glazebrook et al., 2017; Merlin et al., 2018; Girelli et al., 2019; Merlin et al., 2019; Tanaka et al., 2019; Santini et al., 2020; Valentino et al., 2020; Esdaile et al., 2021) as massive QGs (MQGs) were already present at these times although less numerous than in the local Universe. As of $z = 2.5$, quenched galaxies have become the majority population, first amongst the most massive ones and later on amongst less and less massive galaxies. Indeed at $0.2 < z < 0.5$, the quiescent population was predominant for all galaxies with stellar masses above $10^{10.5} M_{\odot}$ (Muzzin et al., 2013).

A set of extremely red $z \sim 3 - 6$ galaxies initially revealed by the Spitzer IRAC intrument, will soon[4] be studied by the James Webb Space Telescope's (JWST) NIRSpec instrument to distinguish between QGs and dusty SFGs (Barrufet et al., 2021). JWST/NIRSpec will have the ability to differentiate these two galaxy types thanks to its broad $0.6 - 5.3\mu$m coverage range and reveal galaxy kinematics (Nanayakkara et al., 2021). Additionally, JWST will provide a better basis for separating high-$z$ QGs and low-$z$ dusty SFGs through the monotoring of 4000 Åbreak and $20\mu$m rest-frame band (Merlin et al., 2018). In the near future, the European Extremely Large Telescope (ELT) will become the largest optical near-IR telescope. It will deliver spectral data for some of the faintest of objects and will allow for strong morphological analysis (Merlin et al., 2019). Its atmospheric distortions-corrected images will be significantly sharper than HST[5].

## 1.4 Properties of Observed MQGs

We will now go over a few physical properties associated to MQGs present in literature from detected emission lines to inferred stellar mass densities and velocity dispersion.

### 1.4.1 Galaxy Emission Lines

To start, we will focus on characteristic emission lines of such galaxies at high-$z$. First off, $H\alpha$ emission lines have been known to originate from H II regions, clouds of ionized hydrogen atoms, with young ($< 10^7$yr) star clusters. As such, the width of measured $H\alpha$ emission lines has been interpreted as a present-to-past $SFR$ indicator. As it turns out, some MQGs have been found to not exhibit any $H\alpha$ emission lines which further confirmed the lack of ongoing star formation (Kriek et al., 2006). Other QGs were caught emitting faint mid-IR light, with

[4]The announced launch date is December 18 2021 from Europe's Spaceport in French Guyana on an Ariane 5 (JWST Launch).

[5]See EELT Announcement and Facility

a weak stellar contribution at these wavelengths. This is in net contrast with the intense mid-IR light arising from dust re-emission of UV-absorbed light observed in the case of SFGs (Fontana et al., 2009).Additionally, strong $H\beta$, $H\gamma$ and $H\delta$ Balmer emission lines that likely originated from short-lived A-type stars were spotted in the near-IR spectrum of a MQG at $z = 3.717$. This revealed the galaxy's past starburst history (Glazebrook et al., 2017). Finally, a few recently quiescent galaxies have exhibited high ratios of $[NII]/H\alpha$, low emission levels of $[OIII]/H\beta$ and $[OIII]/[OII]$ and the ionised gas' large line width. This is in agreement with shocked gas stemming from AGN-driven outflows although AGN photoionisation is also another possible cause in some cases. Such outflows may be considered as quenching processes since they lead to the heating of the interstellar medium (Newman et al., 2018).

### 1.4.2 Galaxy Stellar Mass Functions

Then we have a look at the galaxy stellar mass of these MQGs. The Stellar Population Synthesis (SPS, Bruzual et al., 2003) model has provided an assessment of the spectral evolution of stars. This has made possible the capture of galaxy rest-frame colors which in turn served to establish blue and red galaxy populations. By assuming red galaxies to be quiescent, a galaxy stellar mass function (GSMF) of quiescent populations is finally obtained (Ilbert et al., 2013). Now, these color quiescent GSMF's almost invariant high mass end slope has been interpreted as proof of insignificant mass growth for highly massive quiescent galaxies at $z < 1$ once the star formation has been quenched and major galaxy-galaxy mergers are infrequent. Moustakas et al., 2013 has further confirmed this implication finding that mergers do not represent a decisive player in galaxy mass growth. At $z \sim 3.75$, the quiescent GSMF, approximated by a single Schechter, has shown a considerable MQG population with a characteristic Schechter stellar mass $M^\star$ increasing with decreasing redshift amounting to $10^{10.52} M_\odot$ at $z = 2$. The less massive quiescent group only becomes noticeable at later cosmic times ($z < 1.5$) with the then GSMF being fitted with double Schechter functions. Additional validation is required to confirm $z = 1.5$ as a pivotal epoch for quiescent galaxies (McLeod et al., 2021). The strong evolution of the GSMF deduced in Davidzon et al., 2017 has supported the emergence of MQGs at $z = 3$ while Santini et al., 2020 has pushed it to even earlier times ($z = 4$).

### 1.4.3 Galaxy Stellar Mass Densities

Thirdly, we turned our attention to the stellar mass density of these MQGs (either in terms of the surface density $\Sigma_\star$ or the volume density $\rho_\star$). To begin, the average $\rho_\star$ within the effective radius has been measured to be $\sim 100$ times higher in MQGs at $z = 2.3$ than in nearby massive elliptical galaxies often taken as nowadays quiescent descendants (Bezanson et al., 2009). In addition, four newly analysed MQGs at $3 < z < 4$ were discovered to be more compact in the $HLR - M$ plane (with $HLR$ the half-light radius) than MQGs at $z = 2$ (Esdaile et al., 2021). This should imply that, since $z = 4$, MQGs have become severely less and less compact within the effective radius with decreasing redshift. Interestingly, within a 1kpc-radius, the $\rho_\star$ and the $\Sigma_\star$ of MQGs, since $z \approx 2$, have halved or decreased by no more than a third (Bezanson et al., 2009; Mosleh et al., 2017). For comparison, during that same period, the $\Sigma_\star$ within a 1kpc-radius of massive SFGs has almost doubled (Mosleh et al., 2017). These trends for MQGs have been interpreted as supporting an inside-out stellar mass growth evolution; the central regions of nearby massive ellipticals being the remains of compact MQGs (Bezanson et al., 2009). For such a growth scenario, an expulsion of the central star formation towards the outer regions, within these galaxies, is expected to have occurred as early as $z = 2.5$ (Tacchella et al., 2017). More generally, as of $z = 3.5$, the redshift evolution of the $\rho_\star$ of MQGs has been predicted to be $(1 + z)^{-4.7}$. This actually corresponds to the squared of the redshift evolution of the $\rho_\star$ of massive SFGs. This implies that the quenched

population since $z = 3.5$ has experienced a more rapid $\rho_\star$ growth than was recorded for the star-forming population (Muzzin et al., 2013). Finally, a recent study has concluded in the possible existence of a minimal mass-and-redshift dependent threshold of $\Sigma_\star \geqslant 10^{10} \mathrm{M}_\odot \mathrm{kpc}^2$ within $1kpc$ for quenching to start. This verdict was reached after galaxies showing substantial levels of central $\Sigma_\star$ were found to be predominantly quiescent. Adding to this was an apparent drop in the $\Sigma_\star - sSFR$ plane at this specific $\Sigma_\star$. However, a direct causal link between $\Sigma_\star$ and $sSFR$ has been hard to confirm (Mosleh et al., 2017). Previously in van Dokkum et al., 2015, AGN feedback or other mechanisms coupled to stellar density were thought to kick in once a stellar mass density threshold was reached and then cause star-formation to cease.

### 1.4.4 Galaxy Radii

Fourthly, we give a view of the galaxy radii evolution of these MQGs through cosmic time. Typically, there have been two distinct galaxy radii in literature even if one is more regularly stated.

The first characteristic size, most frequently deduced from observations, has been the effective radius $R_{eff}$. The effective radius refers to the semi-major axis radius of the ellipse within which half of the total light, emitted from a galaxy, is found. It has often been inferred by semi-major axis of the half-light ellipse of Sersic model fits of light profiles (van der Wel et al., 2014). This has allowed the detection of a much greater increase in the number density associated to small-sized passive early-type galaxies than of small late-type SFGs from $z = 3$ to $z = 1.5$. Subsequently, the small massive compact late-type galaxy population was suggested to be a likely intermediate state between massive but less compact late and early type galaxies (van der Wel et al., 2014). For context, by strictly comparing the average radius evolution between QGs and SFGs, observations, from $z = 3$ to $z = 0$, have revealed the size growth to be faster in the case of QGs than for SFGs. Indeed, the exponent of its radius' redshift evolution ($R_{eff} \sim (1+z)^{-1.48}$) was found to be twice that of SFGs (van der Wel et al., 2014).

The second galaxy size commonly used has been the stellar half-mass radius $SHMR$. As the name suggest, $SHMR$ indicates the radius that halves the integrated stellar mass density profile, previously extrapolated to 100kpc (Mosleh et al., 2017) or less. By insisting on massive compact dusty SFGs at $z = 2.5$ being progenitors of $z = 2$ quiescent galaxies, $SHMR$ of these galaxies has been expected to experienced a 37.5% decrease following nuclear starburst events (Barro et al., 2016). Thus, quiescent galaxies at $z = 2$ are suggested to be more compact than their progenitors at $z = 2.5$.

A comparison between $SHMR$ and $H_{160}$-band $R_{eff}$ confirmed that $SHMR < R_{eff}$, when it comes to MQGs, as $SHMR$ amounted to $30 - 50\%$ of $R_{eff}$ (Mosleh et al., 2017).

### 1.4.5 Galaxy Stellar Velocity Dispersion

Finally, we address MQGs' stellar velocity dispersion $\sigma_{e,\star}$, defined as the statistical scatter or dispersion of the stellar velocities relative to its mean stellar velocity. Balmer absorption lines are crucial for the estimations of $\sigma_{e,\star}$ at high-$z$ ($z > 1$) however, it is no longer the case at $z < 1$. This was recently confirmed in Belli et al., 2017.

First of all, at $3 < z < 4$, observations of MQGs have shown that the $\sigma_{e,\star}$ range between $200 - 300$km/s (Tanaka et al., 2019; Esdaile et al., 2021). These high $\sigma_{e,\star}$ are correlated to high levels of stellar mass and small radii (Esdaile et al., 2021). Later on at $1.5 < z < 2.5$, the inferred dissimilarities in $\sigma_{e,\star}$ between edge-on and face-on in some MQGs have appeared to suggest that they host rotational disks within them. Further confirmation of these disks at high-$z$, have come with today's MQGs having only half the $V/\sigma_{e,\star}$ ratio (with the circular velocity $V$) of those at high-$z$ (Belli et al., 2017). This later evolution of these disks inside MQGs has been understood to be the result of dry mergers at $z < 1.5$ which diminished

the angular momentum of the disks (Belli et al., 2019). The disappearance of rotational disks implies that galaxy morphological evolutions, from disk galaxies to nowadays ellipticals, were not necessarily synchronized with quenching mechanisms (Belli et al., 2019). Such a conclusion stands in clear conflict with common understanding (see Bezanson et al., 2009). At $0.9 < z < 1.6$, MQG population has been observed with smaller radii but larger $\sigma_{e,\star}$ than nearby massive galaxy populations (Belli et al., 2014).

Finally, ionized gas disks, derived from gas dynamics and $H\alpha$ emission lines, were found within compact massive SFGs at $z > 2$, potential progenitors of compact MQGs at $z > 1.5$, have a tendency to lower the estimated $\sigma_{e,\star}$. These disks, in fact, cover regions up to twice those covered by stars (van Dokkum et al., 2015).

## 1.5 Candidate Quenching Mechanisms

The true mechanisms responsible for the quenching of star formation in high-$z$ galaxies have not yet been established (Belli et al., 2017) and are still up for debate. Though, concerning massive ($\gtrsim 10^{10.5} M_\star$) galaxies, quenching has been observed to be efficient since $z = 2.5$ (Fumagalli et al., 2014). In addition, the drop in the high mass end of the $SFR$-mass relation as of $z = 3.5$ has been seen as a sign of substantial quenching and fast growth in galaxies at high-$z$ (Tasca et al., 2015). Amongst the multiple processes and scenarios envisioned for suppressing star formation, feedback from low level active galactic nuclei (AGN) is the most likely candidate (Cheung et al., 2016; Belli et al., 2019) triggering early quenching (as of $z \approx 4.5$, Girelli et al., 2019).

AGN feedbacks are observed to happen in two major modes: jet/radio mode, directly detectable by X-ray imaging, and radiative/quasar/bright mode. In the first mode (radio mode), quenching occurs through relativistic particles-based collimated jets warming up the supply of cold halo gas. In the second mode (quasar mode), however, it is the result of mergers, fast black hole growth and quasar winds expelling gas beyond central regions (Girelli et al., 2019). Mergers tend to be recurrent in proto-clusters where galaxy number densities are significant and velocity dispersion are weak (Sherman et al., 2020). Repeated mergers combined with AGN and stellar feedback could over stimulate star formation leading to its suppression in central regions. In the young universe ($2.5 < z < 3$), such mechanisms could act as another remarkable quenching processes Sherman et al., 2020). Strong nuclear starbursts with depletion times of $\sim 0.1 Gyr$ could also allow massive and large dusty SFGs at $z = 2.5$ to be the direct progenitors of compact MQGs at $z = 2$ (Barro et al., 2016). This is known as a dissipation-driven formation scenario.

Observations suggest two different timescales for quenching: one slow essentially concerning large galaxies, and one fast backed up by gas-rich mergers and producing compact post-starburst galaxies. Slow quenching is primarily the product of cold gas depletion following the appearance of stable virial shocks coupled with the AGN radio-mode feedback heating. It may also result from the receding of gas inflows towards galaxies or other cosmological or gravitational effects (Belli et al., 2019). Throughout the Universe, cold dense intergalactic filaments ensure the flow of gas from the ionized intergalactic medium towards galaxies. This is expected to contribute to quick star formation in galaxies(Sherman et al., 2020). Following observations of large gas reservoirs in some post-starbursts and quiescent galaxies, Schreiber et al., 2018 proposed that quenching within galaxies may start before gas depletion. This hints towards other possible quenching processes other than gas depletion as favorable candidates of slow quenching.

Some quenching processes, such as gas disk stabilization, have been described as morphological processes. Gas disk stabilization, supported by a deep potential well and a removal of

stellar disk structure, would prevent perturbation and fragmentation of the gas disk and its collapse into star-forming gas clouds (Martig et al., 2009).

Looking at a specific population of MQGs, dead galaxies, it has been shown that extremely low $SFR$s measured in dead galaxies at $z > 1.5$ may be explained by inefficient gas recycling (star formation sustained by the mass loss of old stars) (Belli et al., 2019). This entails that quenching processes are restraining the cooling of the to-be recycled gas or perhaps ejecting it to outer regions. This phenomenon could explain a 60% increase in the stellar radius from $z = 2$ to present day (Belli et al., 2019). Supplementary evidence is needed to support the case of inefficient quenching mechanisms in massive halos at $z > 3$. At those times, star formation is monopolized by inefficient baryonic cooling (Davidzon et al., 2017). Yet, signatures of efficient quenching processes are already reported at $z = 2$.

In Peng et al., 2010 two phenomenological quenching paths are introduced. The first path would be via environment quenching, associated to a galaxy migration towards high over density zones while large cosmological structures form. This path is efficient for low mass galaxies and results in recently quenched galaxies being interpreted as a primary quenching transitional state (Ichikawa et al., 2017). Environmental quenchings include ram pressure stripping (stripping of cold gas in the outer low stellar mass dense regions), gravitational harassment (overall impact of frequent high speed tidal interactions) and starvation / strangulation (Moustakas et al., 2013). Gravitational harassment is thought to be effective for old cluster galaxies with high velocity dispersion, in so far as gravitational torques imply gas inflow to central regions fueling only central star formation (Querejeta et al., 2016). The second phenomenological path is mass quenching intrinsic to the total galaxy stellar mass and appears to be the dominant path taken by massive ($> 10^{10.2} M_{\odot}$) quiescent galaxies.

Future minor mergers, will, in the case of passively evolving galaxies, contribute to mass growth in the outer regions while leaving the central regions almost unchanged (Mendel et al., 2020).

## 1.6 Cosmological Galaxy Formation Simulations

In recent years, state of the art cosmological simulations, Illustris (Vogelsberger et al., 2014; Genel et al., 2014; Sijacki et al., 2015), EAGLE (Schaye et al., 2015; Furlong et al., 2017), SIMBA (Davé et al., 2019) and IllustrisTNG (The Next Generation, Pillepich et al., 2018b; Pillepich et al., 2018a, Springel et al., 2018, Nelson et al., 2018, Naiman et al., 2018, Marinacci et al., 2018) have been developed and later used as virtual laboratories to study various aspects of galaxy formation and evolution over large cosmic timescales otherwise unobtainable through simple analysis of observations and smaller models. As a result, they have been employed to interpret the predicted mechanisms behind suppression of star-formation in quiescent galaxy populations in EAGLE (Schaye et al., 2015), SIMBA (Rodríguez Montero et al., 2019) and IllustrisTNG (Weinberger et al., 2018).

The goal of this work is to understand the extent to which modern cosmological simulations, such as IllustrisTNG, can replicate observed populations of MQGs as early as $z \sim 3$ and their basic properties. Now, having such a cosmological simulation at hand, we take a further step to identify the mechanisms and reasons behind the quenching of star-formation at these early cosmic epochs. As such, this report is divided into four parts. We start off, in chapter 2, with a presentation of the IllustrisTNG cosmological simulation used in our study of MQGs at high-$z$. Our IllustrisTNG results and predictions are presented in chapter 3. In chapter 4, we discuss and analyse our outcomes before summarizing our general conclusions in chapter 5.

# Chapter 2

# IllustrisTNG Simulations

In this section, we will introduce the IllustrisTNG simulation. We will first look at the assumed initial conditions. Then, we will present the Illustris simulation as the basis for the newer updated version whilst considering some of the physical processes implemented into the simulation. And finally, we will address previous results linked to quiescent populations and obtained using the IllustrisTNG simulation.

## 2.1 Initial Conditions and Conventions

IllustrisTNG's cosmological parameters, selected from the Planck Collaboration et al., 2016, are as indicated in Table 2.1. .

| $\Omega_\Lambda$ | $\Omega_B$ | $\Omega_{DM}$ | $h$ | $n_s$ |
|---|---|---|---|---|
| 0.6911 | 0.0486 | 0.3089 | 0.6774 | 0.9667 |

Table 2.1: IllustrisTNG cosmological parameters: the vacuum density $\Omega_\Lambda$, the cosmological baryonic density $\Omega_B$, the dark matter density $\Omega_{DM}$, the scaled Hubble constant $h = H_0/100$km/s/Mpc and the spectral index $n_s$ selected from the Planck Collaboration et al., 2016

The Illustris Simulation is a ab initio ($z = 127$ under the Zedovich approximation accounting for the non-linear epochs of the simulated universe's gravitational evolution) magneto-hydrodynamical ΛCDM cosmological simulation with a flat curvature presupposing a three-constituent universe: baryonic matter, dark matter and dark energy which sustains the simulated universe's accelerated expansion.

Cold Dark Matter (CDM) and Hot Dark Matter (HDM) are two distinct approaches based on the velocity of dark matter components. HDM supposes relativistic velocity dispersion while CDM presumes weaker speeds. This difference in nature of dark matter leads to clear disparities. Under the HDM paradigm, its dark matter components are subject to free streaming namely the ability to flow unaffected by gravitational potential wells induced by over-dense regions that inevitably dissipate. This favors the early forming of large cosmological structures before the appearance of galaxies emerging from the fragmentation of these super structures. These features and evolutionary stages do not arise with CDM defined dark matter. On the one hand, such HDM predictions are in obvious disagreement with observations of high-$z$ galaxies and quasars as well as the flat rotation profiles of spiral galaxies. The CDM theory, on the other hand, clearly justifies the cosmic microwave background radiation (CMB), the Universe's expansion history and some characteristics of large cosmological structures (SpringerBook).

In the following study, we use $\mathcal{M}$ as $\log_{10}(M_\star/M_\odot)$ with $M_\star$ in solar masses $M_\odot$.

## 2.2 Illustris Simulation Base

IllustrisTNG is cosmological magneto-hydrodynamic simulation conducted with the AREPO code.

Illustris' first particularity is its galilean-invariant, gridless moving mesh provided by the AREPO code (Springel, 2010) which allows for a finite volume approach and a second order unsplit Godunov scheme along with an exact Riemann solver. Such a code avoids fluid instability suppression stemming from Langrangian smoothed particle hydrodynamic (SPH) approaches and over-mixing combined with galilean-invariance loss from Eularian hydrodynamics with cartesian adaptive mesh refinement (AMR) systems. This unstructured moving mesh is tessellated with Voronoi cells. The Voronoi tesselation attributes to a given cell center, without overlapping, the area closest to it. These center points may also be viewed as triangle vertices adding up to form a Delaunay tesselation of space. The fundamental requirement of Delaunay triangulation is that a trangle's associated circumcircle may not inclose other mesh points. If a mesh point were to be added or moved, this no-point-within-circumcircle property would need to remain valid for every newly drawn connecting link. Then, the Voronoi underlying characteristic would be applied to reach a new evolved mesh.

The AREPO code was upgraded to allow for quasi-Langrangian magnetohydrodynamics (MHD, Pillepich et al., 2018b). With the addition of magnetic fields and the ideal MHD assumption, an 8-wave Powel cleaning algorithm was implemented to maintain the null divergence. Taking magnetic fields into consideration is a major improvement to the Illustris simulation. The Green-Gauss spatial gradient estimator has also been replaced by a Least-Squares Fit estimator (LSF) to limit strong center of mass and mesh point location deviations in the case of strongly irregular geometry cells.

The gravitational force is numerically calculated using a Tree-PM (Particle Mesh) scheme with a hierarchical octree algorithm when dealing with short range forces and a particle mesh method when longer. The simulation volume is a comoving box with periodic boundaries which is expressed in comoving kpc (ckpc). Multiplying a comoving length by the scale factor $a = \frac{1}{1+z}$ converts it to a physical length.

Cosmologically simulated haloes are indentified using Friend-Of-Friend algorithm with a linking length of 20% of the mean inter-particle distance (Pillepich et al., 2018a). The later identification of subhaloes is accomplished using the numerical method SUBFIND as in Subhalo Finder (Springel et al., 2001). This algorithm assumes subhaloes to be locally over dense self-connected particles. For this, it begins by establishing a density map associated to all particles bound to the halo. With this distribution obtained, the algorithm will first determine all possible candidate subhaloes with a high-to-low density binding analysis and then it confirms those candidates satisfying the substructure definition with a low-to-high density unbinding. During the identification phase, it links, at each iteration, the highest unbound point to one or two of its nearest most bound neighbors until all points have been checked. If a point unites two previously unconnected particle groups then both groups are categorized as possible subhalo candidates and the algorithm goes on to find the next most dense unbound point. During the confirmation phase, candidates are subject to unbinding scheme. For this procedure, the most bound particles within substructures are classified as subhalo center and their velocity as the candidates' mean velocities. By appending the Hubble flow, due to universe expansion, to the velocity of the other bound particles, the algorithm then unbinds all of the positive total energy particles. Non-repeated candidates are finally confirmed as subhalos if more than a certain number of points remain bounded.

For each simulation run and time iteration, whole volume information is stored in a snapshot file and a group catalog file. Snapshots contain data simulated headers, parameters, configurations and five PartType packages. PartTypes include gas, dark matter, tracer, star with wind and black hole particles. For every PartType group, certain physical traits are stored.

Group catalogs are composed of overall halo or subhalo properties. A third characteristic is the dark matter and subhalo merger trees.

Merger trees are connections between groups and subgroups of different snapshots. They are obtained using the LHaloTree and and SubLink algorithms respectively. The SubLink procedure is subdivided into three steps (Rodriguez-Gomez et al., 2015). First of all, for each subhalo at snapshot $S_i$, the algorithm determines all the possible descendant subhaloes at $S_{i+1}$ with which it shares common particles. Then, each candidate subhalo is graded with regards to a particle mass and particle binding energy rank. Finally, the candidate with the highest merit score is recognized as the unique descendant. If a descendant subhalo moves so close to a larger structure that difference in density is weak, the subhalo may be skipped. In this case, a descendant in the following snapshot will be identified as the descendant. However, if it remains in the larger structure for more snapshots, the search for a descendant will stop and it will be added to the larger structure. A chain of progenitor and descendant galaxies form progenitor or descendant branches respectively. The main progenitor branch is the progenitor branch composed of all the first progenitors that is the progenitors with the most massive past history.

## 2.3 Galaxy Formation Processes

The IllustrisTNG Simulation, is based on the strength of the Illustris Simulation. However, numerous changes have been made. The simulation has three distinct simulated volumes with cubic sides of $35\,h^{-1} \approx 50\,\mathrm{Mpc}$ (TNG50-X), $\approx 100\,\mathrm{Mpc}$ (TNG100-X) and $\approx 300\,\mathrm{Mpc}$ (TNG300-X). In the following study, we focus only on the TNG100-1 and TNG300-1 runs since they have the highest baryonic and dark matter resolution while still being the largest simulated volumes. Their physical and numerical parameters are displayed in Table 2.2. The simulation was built to ensure that the smaller the volume the higher the baryonic particle mass $m_B$ and dark matter particle mass resolution $m_{DM}$. The 100 stored snapshots now start at $z \sim 20$ (0.179 Gyr) and finish at $z \sim 0$ (13.8 Gyr) with a range of $\sim 0.05 - 0.2\,\mathrm{Gyr}$ between snapshots.

| **Parameter** | **Unit** | **TNG100-1** | **TNG300-1** |
|---|---|---|---|
| $L_{Com.Cub}$ | $\mathrm{cMpc\,h^{-1}}$ | 75 | 205 |
| $L_{Phys.Cub}$ | Mpc | 110.7 | 302.6 |
| $N_G$ | – | $1820^3$ | $2500^3$ |
| $N_{DM}$ | – | $1820^3$ | $2500^3$ |
| $m_B$ | $10^6 M_\odot$ | 1.4 | 11 |
| $m_{DM}$ | $10^6 M_\odot$ | 7.5 | 59 |

Table 2.2: Physical and numerical parameters from TNG100 and TNG300 simulation runs: the comoving cubic size length $L_{Com.Cub}$, the physical cubic size length $L_{Phys.Cub}$, the total number of gas cells $N_G$ and dark matter particles $N_{DM}$, the average baryonic mass $m_B$ and the average dark matter mass $m_{DM}$

One of the first major astrophysics-related improvements concerns supermassive black holes and their low accretion rate feedback. The previous thermal bubble model was replaced by black hole-driven winds. The black hole seeding mass has been increased by a factor 8 to $1.18 \times 10^6 M_\odot$ as soon as the halo reaches a mass of $7.38 \times 10^{10} M_\odot$ which implies a stronger and sooner impact of the black hole on its host. In the IllustrisTNG simulation, galactic winds now have the ability to flow isotropically. This is in contrast with previous bipolar constraints applied onto these winds. This still produces galactic fountains due to the spreading in the direction of minimum resistance. The evolution of stars was modified as well to better agree

with observations. Simulated stars evolve along the asymptotic giant branch before core collapse (Ia or II), once they have reached a mass threshold of $8\,M_\odot$ ($6\,M_\odot$ with Illustris). A notable novelty is the gas-metallicity dependent parametrisation of the injection mass loading.

As mentioned in Pillepich et al., 2018b, IllustrisTNG simulation features not tuned to fit observations as well as not negatively impacted by numerical adaptation may be interpreted as predictive. The IllustrisTNG simulation was calibrated to imitate certain $z = 0$ observation relations among which are the GSMF, the stellar mass to size relation, the black hole to galaxy mass relation and the $z < 10$ cosmic star formation rate density.

As soon as a Voronoi gas cell reaches a density threshold of $0.1\mathrm{cm}^{-3}$, it becomes star forming (Donnari et al., 2019). This gas cell is then attributed a disk-averaged star formation rate density $\Sigma_{SFR}$ according to the empirical Kennicutt-Schmidt law (Springel et al., 2003; Kennicutt, 1998):

$$\Sigma_{SFR} = (2.5 \pm 0.7) \times 10^{-4} \left( \frac{\Sigma_{gas}}{1\,\mathrm{M}_\odot\,\mathrm{pc}^{-2}} \right)^n \frac{\mathrm{M}_\odot}{\mathrm{yr}^{-1}\,\mathrm{kpc}^{-2}}$$

with $n = 1.4 \pm 0.15$ and $\Sigma_{gas}$ the gas cell's associated surface density. The star particles produced have a Chabrier Initial Mass Function (Chabrier, 2003) and are common-aged stellar populations. Minimum non zero $SFR$s are star forming time dependent. $SFR$s increase with the cell's cold gas mass (Donnari et al., 2019).

Once the black hole particle is seeded, and maintained in its host's minimum gravitational potential even in the event of black hole mergers, it accretes following a non-boosted Bondi-Hoyle accretion $\dot{M}_{Bondi}$ with a superior Eddington accretion $\dot{M}_{Edd}$ limit (Weinberger et al., 2018):

$$\dot{M}_{Bondi} = \alpha \frac{4\pi G^2 M_{BH}^2 \rho}{c_S^3} \qquad \text{with} \qquad \alpha = 1$$

$$\dot{M}_{Edd} = \frac{4\pi G M_{BH} m_p}{\varepsilon_r \sigma_T} c \qquad \text{with} \qquad \varepsilon_r = 0.2$$

with the gravitational constant $G$, the black hole mass $M_{BH}$, the kernel-weighted surrounding density $\rho$, the kernel-weighted surrounding sound speed $c_S$, the mass of a proton $m_p$, the light speed $c$, the radiative efficiency of the black hole $\varepsilon_r$ and the Thompson cross section $\sigma_T$.

The black hole feedback has two modes: one for the high accretion rates and another for low accretion rates. In the high accretion state, feedback occurs through thermal injection with an associated energy of:

$$\dot{E}_{HA} = 0.02 \dot{M} c^2$$

Alternatively, in the low accretion state, kinetic winds stemmed from the black hole amounting to an overall kinetic energy of:

$$\dot{E}_{LA} = min \left( \frac{\rho}{0.05 \rho_{CSF}}, 0.2 \right) \dot{M} c^2$$

with the critical star forming density $\rho_{CSF}$. The $min$ function assigns a value to the weakness of the AGN feedback energy-environment coupling. The Eddington ratio $f_{Edd} = \dot{M}_{Bondi}/\dot{M}_{Edd}$ relative to:

$$f_{crit} = min \left( 0.002 \left( \frac{M_{BH}}{10^8\,\mathrm{M}_\odot} \right)^2, 0.1 \right)$$

stands as the separation line between both accretion states.

To guarantee a time efficient chemical enrichment of the interstellar medium (ISM), the enrichment process only materializes if one out of two conditions are fulfilled: the star particle-to-total galaxy stellar mass ratio surpasses 0.0001 or the star particle is newly formed

($<$ 100Myr). Such a modification in the implementation of chemical enrichment does not affect the overall simulation results. The modelling of gas cooling (from the ionizing UV background radiation field, metal lines and AGN radiation field), self-shielding for dense ISM and stellar feedback (driving galactic outflows) are also required and so added to the Illustris and IllustrisTNG simulations (Pillepich et al., 2018b).

## 2.4 Galaxy Definition Criteria with IllustrisTNG

The simulation allows for two distinct galaxy definitions based on aperture. All particles bound to a unique subhalo are considered to form an all-bound (AB) galaxy, whereas for an in-radius (IR) galaxy, only those contained within twice the stellar half mass radius (SHMR) are kept. We expect the properties of IR-defined galaxies to be more in agreement with observations as the IR galaxy definition describes galaxies in a way which is closer to the one adopted by observations. Initially, three additional galaxy definitions were taken with spherical apertures of 10ckpc/h, 30ckpc/h and 100ckpc/h. Galaxies are also required to have a stellar mass 1000 times the simulation's average stellar particle mass which means $\mathcal{M} = 9.15$ for TNG100-1 and $\mathcal{M} = 10.04$ for TNG300-1 to be properly resolved. The last galaxy criterion adopted avoids the inclusion of flagged galaxies with doubtful cosmological origins. These suspicious galaxies formed while they were satellites with low dark matter fraction ($< 80\%$) within a halo's virial radius. In addition, the stellar formation time ($SFT$) provides an adequate distinction between stars ($SFT > 0$) and wind phase gas cells ($SFT \leqslant 0$) combined to form the fourth particle type.

There are three different approaches to studying IllustrisTNG simulation data: an analysis of downloadable data files, a web-based interface approach with requests and a JupyterLab technique. We have found the second way of analysis to be most suited for the study of merger trees as it presents the best apparent data stored-to-analysis time ratio.

## 2.5 Previous Results of MQGs with IllustrisTNG

Finally, we will introduce a few of the latest published results (2018, 2019) of research relating to the study of MQGs achieved with the IllustrisTNG simulation.

Some of the published results (Donnari et al., 2019) have already emphasized the importance and effects of the quiescent criterion and of the galaxy definition criterion on the QG and SFG populations. As it turns out, the level of the bending of the main star-forming sequence ($MSFS$) at the high mass end ($\mathcal{M} = 10.7 - 11.5$) strongly depends on the quiescent criterion used. However, UVJ-defined QGs and 1dex-below-$MSFS$-defined QGs have almost identical quiescent galaxy fractions. This likely implies that both quiescent criteria classify the same galaxies as part of the QG population. Furthermore, results have shown that non negligeable amounts of star formation takes place in the outer regions of galaxies. This explains the $MSFS$'s overall drop in terms of $SFR$ when smaller apertures are selected. Thus, smaller galaxy apertures lead to more galaxies being categorized as quiescent. This negatively impacts IllustrisTNG's ability to reproduce observations.

Other findings, from Nelson et al., 2019 using TNG50 runs, have highlighted several properties of galactic outflows from MQGs at $1 < z < 6$. All galaxies with $SFR$ below the $MSFS$ have been categorized as quiescent. First of all, MQGs, from TNG50, have been found to have the most powerful black hole driven-outflows although they are only comparable to those of highly starburst galaxies. It has also been shown that at constant galaxy stellar masses, the velocity of outflows in MQGs diminishes with cosmic time. Secondly, it has been documented that the central black hole feedback intervenes more and more in the mass loading of outflows after MQGs have reached stellar masses of $10^{10.5} M_\star$. This is coherent with an ever

increasing mass loading onto the outflow, coming from the black hole feedback, as we turn our attention to increasingly massive ($> 10^{10.5} M_\star$) QGs. Interestingly, for low mass ($< 10^{10.5} M_\star$) QGs the mass loading of outflows is supported by stellar feedback. In this instance, the outflow mass loading gradually reduces with a mass increase in those low mass QGs.

We would also like to present the circumstances behind the past quenching of MQGs at $z = 0$ that have already been explored. To start with, progenitors of small-sized and low-mass QGs at $z = 0$ have been quenched at earlier epochs than large MQGs. Indeed, these large MQGs were noticed to remain longer on the $MSFS$ (Genel et al., 2018). Another publication (Weinberger et al., 2018) claims that the central supermassive black hole, while in its kinetic and low accretion state, is responsible for the existence of a QG population at $z = 0$. This same paper also mentions that black hole growth and feedback (for those with $\log(M_{BH}/M_\odot) > 8.5$) is sustained by gas accretion from black hole mergers (Weinberger et al., 2018).

Interestingly, some research, carried out with IllustrisTNG simulation, are in disagreement with observations. The IllustrisTNG simulation data suggests an apparent underestimation of the $MSFS$ at $0.75 < z < 2.0$ and a need for an improvement of the stellar feedback model (Donnari et al., 2019). In clear disagreement with observations, early-type galaxy sizes are greater than those of late-type galaxies (Rodriguez-Gomez et al., 2019). Weinberger et al., 2018 noticed an over-prediction of the quasar luminosity function monopolized by quickly thermally accreting moderately massive black hole.

# Chapter 3

# Results

For this study, we are exploring the quenching processes behind the observed existence of a high-$z$ quiescent galaxy population. To do so, we have decided to use the IllustrisTNG simulation and more specifically TNG100-1 and TNG300-1. All results are obtained through the investigation of IllustrisTNG data files and should not be treated as observations.

First of all, we focus on IllustrisTNG's ability to reproduce observational GSMFs, quiescent galaxy fractions and different galaxy properties at high and low redshifts so as to specifically test to what extent IllustrisTNG is able to replicate quiescent galaxy populations at high z. Secondly, we review various definitions of quiescence and check their effect on the results mentioned above. Subsequently, we investigate the predictions of simulations on the origins of massive quiescent galaxies at high redshifts. These are heavily debated in observations.

This first part was done using downloaded data files associated to $z = 0$, $z = 0.5$, $z = 1$, $z = 2$, $z = 3$ and exclusively for TNG300-1 $z = 3.5$. This underlying work warrants our decision to direct our attention to IllustrisTNG's time evolution predictions of selected massive quiescent $z = 2$ and $z = 3$ galaxies. Unless specified otherwise, we only display mass bins with a minimal count of 10 elements and the default IllustrisTNG uncertainty range corresponds to the $16^{th}/84^{th}$ percentiles intervals.

## 3.1 Galaxy Stellar Mass Functions of IllustrisTNG Galaxies

We start with studying the GSMFs. For this, we start off by obtaining the global (SFGs and QGs combined) GSMFs for $z = 0$ (Figure 3.1), $z = 2$ (Figure 3.2) and $z = 3$ (Figure 3.3). For every GSMF line, we logarithmically divide the galaxy sample according to their stellar masses into $18-21$ bins for the high redshift samples and $26-27$ bins for $z = 0$ group. Then we divide the number of galaxies per bin by the volume of the simulation and by the logarithmic bin size. This allows for a comparison between different volumes and observations. We assumed different galaxy definitions: the all-bound (AB), the in-radius (IR) and three spherical apertures of within-10 ckpc/h, within-30 ckpc/h and within-100 ckpc/h. Fixed mass bins for every galaxy definition provides a qualitative view of the definition effect. To contextualise the GSMF curves, we compute Poisson error ranges and added observationally fitted simple and double Schechter GSMF functions (Schechter, 1976; Baldry et al., 2008; Bernardi et al., 2013; McLeod et al., 2021).

A clear difference arises in the high mass end ($\gtrsim 10^{11} M_{\odot}$) of the GSMF between Baldry et al., 2008 and Bernardi et al., 2013. As mentioned in Bernardi et al., 2013[1], this noticeable difference in $\phi(M_{\star})$ has to be the result of the stellar mass-to-light ratio ($M_{\star}/L$) only. As a matter of fact, both studies used the same initial mass function (IMF, Chabrier, 2003) to estimate GSMF but their $M_{\star}/L$ vary.

In Figure 3.1 and for $\mathcal{M} \lesssim 10.5$, all of our GSMF curves are in agreement $\lesssim 0.1$dex with observations. At higher masses $10.5 \gtrsim \mathcal{M} \gtrsim 11.2$, the GSMF of the AB TNG100-1 galaxy

[1]The following comments were actually written regarding disparities between Baldry et al., 2012 and Bernardi et al., 2013. However, Baldry et al., 2008 and Baldry et al., 2012 make similar assumptions.

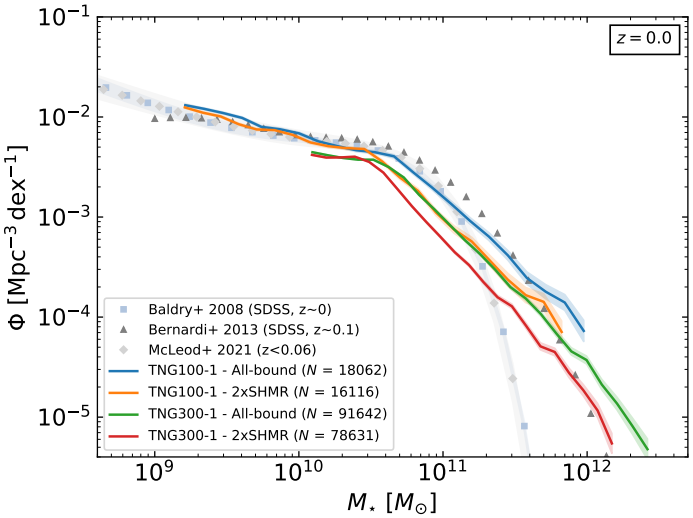


Figure 3.1: IllustrisTNG global galaxy stellar mass function (GSMF) at $z = 0$. Four distinct GSMFs are drawn for all-bound TNG100-1 galaxies (blue), in-radius TNG100-1 galaxies (orange), all-bound TNG300-1 galaxies (green), in-radius TNG300-1 galaxies (red) as well as their associated Poisson error range. The number of galaxies used for each GSMF calculations is noted $N$. A set of double Schechter function fits of observational data points is shown with grey and blue symbols (Bernardi et al., 2013) along with their respective error-propagated uncertainty range in shaded areas (Baldry et al., 2008; McLeod et al., 2021).

sample is the only one consistent with observations. For the high mass end, both AB galaxies are above Bernardi et al., 2013's. For $\mathcal{M} \gtrsim 10.5$, we notice that the GSMF is shifted by $\lesssim 0.2$dex towards higher stellar masses in the case of AB-galaxies compared to IR-galaxies for both TNG100-1 and TNG300-1. This tendency is to be expected since IR-galaxies only account for a fraction of the particles included in the AB definition.

For both $z = 2$ and $z = 3$, we separated TNG100-1 (bottom sub-figures) and TNG300-1 (top sub-figures) curves for more readability. In Figure 3.2, all TNG100-1 GSMFs reproduces almost perfectly the observations. TNG300-1 GSMFs are also in agreement with observations with IR and the within-30 ckpc/h GSMFs among the closest. For both TNG100-1 and TNG300-1, the IR GSMF is enclosed by the within-10 ckpc/h and the within-30 ckpc/h GSMFs suggesting a $SHMR = 5 - 15$ ckpc/h. In Figure 3.3, the significant spread of the observational GSMFs helps all $z = 3$ IllustrisTNG GSMFs to be in clear coherence with observations. Such strong variations in observations do not put any constraint on IllustrisTNG predictions. It is, thus, left unclear how well IllustrisTNG galaxy populations at $z = 3$ replicate reality. For all GSMF regardless of the redshift, we see that TNG300-1 produces a greater number of highly massive $\mathcal{M} \gtrsim 11.2$ galaxies. This is thanks to a larger-sized virtual volume. There in an overlap between both runs in the mass interval $10.0 \lesssim \mathcal{M} \lesssim 11.2$.

As presented in Peng et al., 2010, global GSMFs are expected to resemble double Schechter functions at $z = 0$. This is a direct consequence of the galaxy stellar mass distribution of the star-forming (simple) and quiescent (double) populations. The likely causes of their respective GSMF shapes is discussed in subsection 3.2.2. For the TNG300-1 within-$X$ ckpc/h GSMFs (with $X = 10, 30, 100$), $\sim 5\%$ ($z = 3$) and $\sim 33\%$ ($z = 2$) of galaxies were not available computationally[2] for study. This leads to a clear drop in the $\mathcal{M} \gtrsim 10.5$. The overall GSMF is moved to lower values with increasing redshift meaning the number of simulated galaxies, at or above a given mass, increases with cosmic time.

[2]due to an unfixed Python built-in OSError error when analysing the data

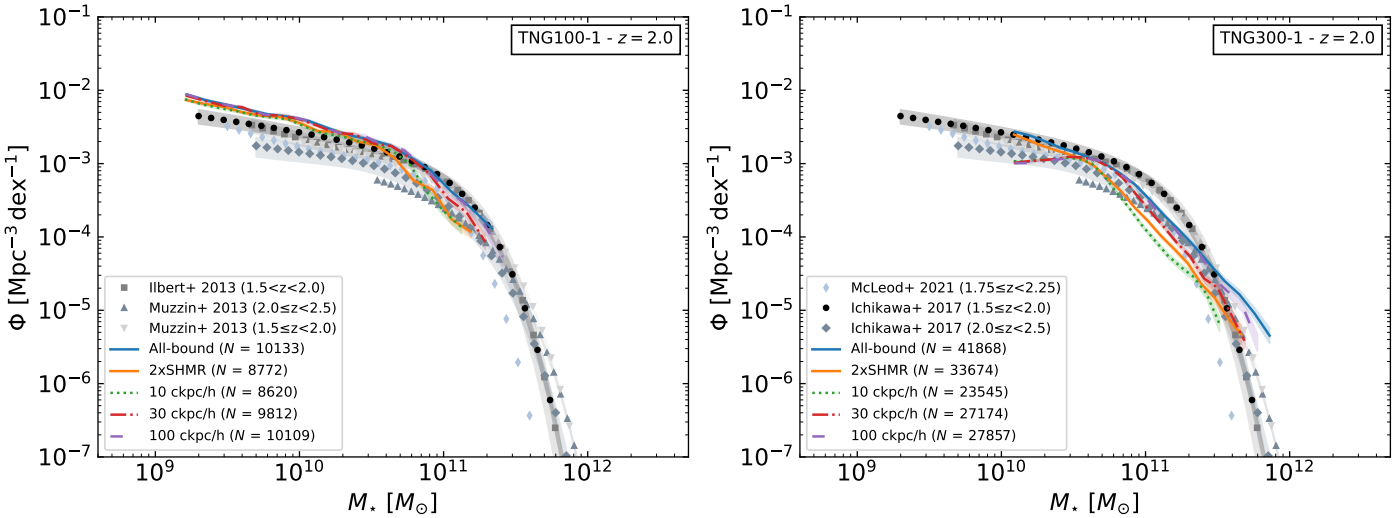


Figure 3.2: IllustrisTNG global galaxy stellar mass function (GSMF) at $z = 2$. Five distinct GSMFs are drawn for both TNG100-1 (top) and TNG300-1 (bottom) for all-bound galaxies (blue), in-radius galaxies (orange), within-10 ckpc/h galaxies (dotted green), within-30 ckpc/h galaxies (dash-dotted red) and within-100 ckpc/h galaxies (dashed purple) as well as their associated Poisson error range. The number of galaxies used for each GSMF calculations is noted $N$. A set of simple (Muzzin et al., 2013; Ichikawa et al., 2017) and double (Ilbert et al., 2013; McLeod et al., 2021) Schechter function fits of observational data points is shown with grey, blue and black symbols along with their respective error-propagated uncertainty range in shaded areas.

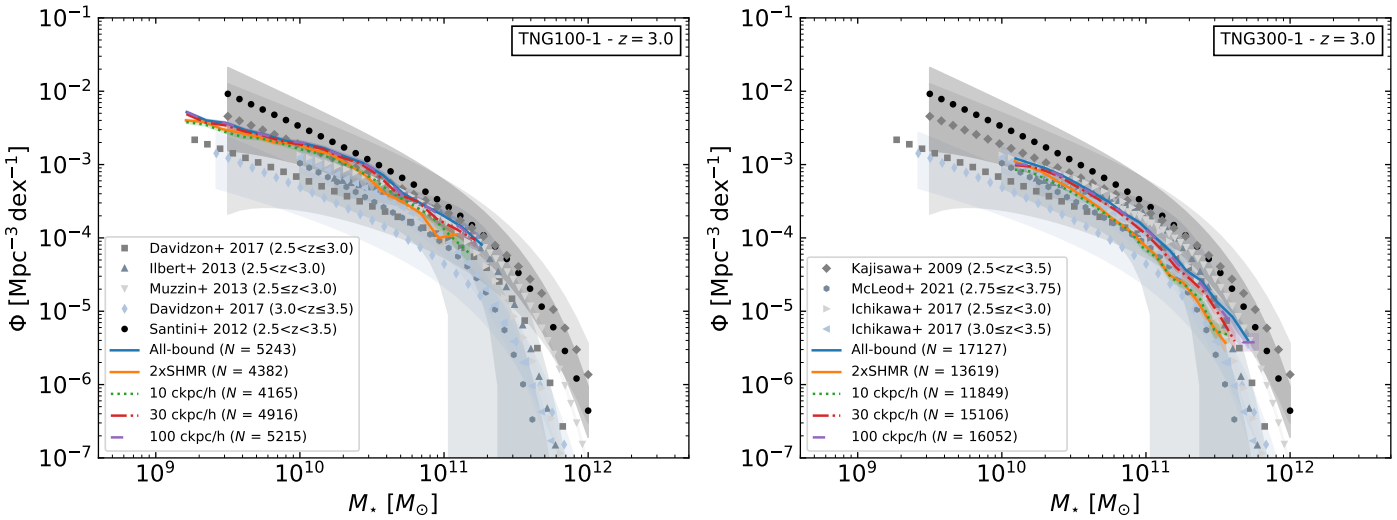


Figure 3.3: IllustrisTNG galaxy stellar mass function (GSMF) at $z = 3$. Five distinct GSMFs are drawn for both TNG100-1 (top) and TNG300-1 (bottom) for all-bound galaxies (blue), in-radius galaxies (orange), within-10 ckpc/h galaxies (dotted green), within-30 ckpc/h galaxies (dash-dotted red) and within-100 ckpc/h galaxies (dashed purple) as well as their associated Poisson error range. The number of galaxies used for each GSMF calculations is noted $N$. A set of simple (Davidzon et al., 2017; Muzzin et al., 2013; Santini et al., 2012; Kajisawa et al., 2009; Ichikawa et al., 2017) and double (Davidzon et al., 2017; Ilbert et al., 2013; McLeod et al., 2021) Schechter function fits of observational data points is shown with grey, blue and black symbols along with their respective error-propagated uncertainty range in shaded areas.

## 3.2 Quiescent Galaxies with IllustrisTNG

We now concentrate on defining the quiescence criterion and visualising its effect on galaxy properties.

### 3.2.1 Quiescent Galaxy Definitions

The redshift evolution of two chosen quiescent criteria are shown in Figure 3.4. Both criteria depend on the specific star formation rate ($sSFR = SFR/M$) of IllustrisTNG galaxies. We

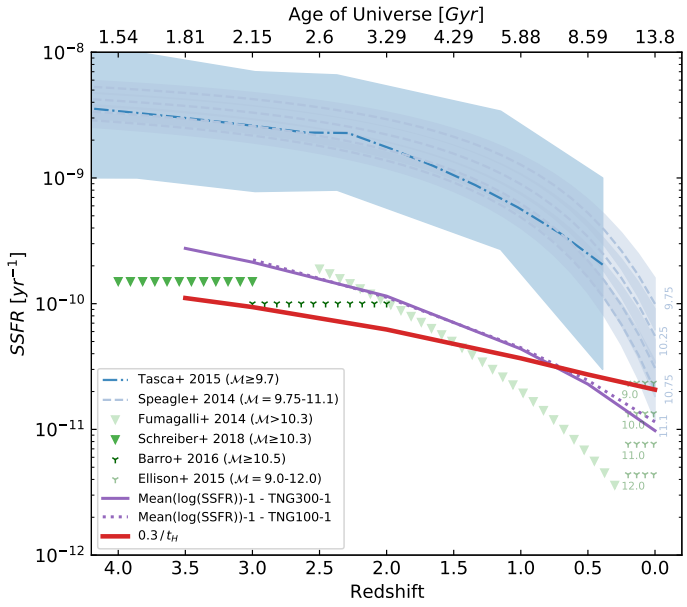


Figure 3.4: Redshift evolution of the specific star formation rate ($sSFR$). The $0.3/t_H$ critical $sSFR$ (red) chosen to distinguish IllustrisTNG quiescent galaxies from star-forming ones. We indicate the critical $sSFR$ using the method selected by Genel et al., 2018 for TNG300-1 (solid purple) and TNG100-1 (dotted purple). In addition, both the star-forming main sequence from Tasca et al., 2015 and Speagle et al., 2014 are shown in dash-dotted and dashed blue lines. We also display the upper $sSFR$ limits of color-defined quiescent galaxies in green triangles (Fumagalli et al., 2014 and Schreiber et al., 2018) and other adopted $sSFR$ threshold in green three-line symbol (Barro et al., 2016 and Ellison et al., 2015).

set $0.3/t_H$, with $t_H$ the Hubble time, as our main critical specific star formation rate ($sSFR_c$, Franx et al., 2008) to separate quiescent galaxies from star-forming ones. We do so in the following way:

$$\text{Quiescent Galaxies}: \quad sSFR < 0.3/tH$$
$$\text{Star-Forming Galaxies}: \quad sSFR > 0.3/tH$$

We also use a main star-forming sequence-based ($MSFS$) quiescent description to split IllustrisTNG galaxies into quiescent and star-forming populations. In other words, all galaxies with a $sSFR$ falling below the mean $sSFR$ of the $MSFS$ at $\mathcal{M} = 9.15 - 10.5$ ($sSFR_{MSFS}$) by at least 1dex are classified as quiescent. In the rest of the report, we will refer to this definition of quiescence using the MS $-$ 1 notation. More explicitly, this MS $-$ 1 quiescent

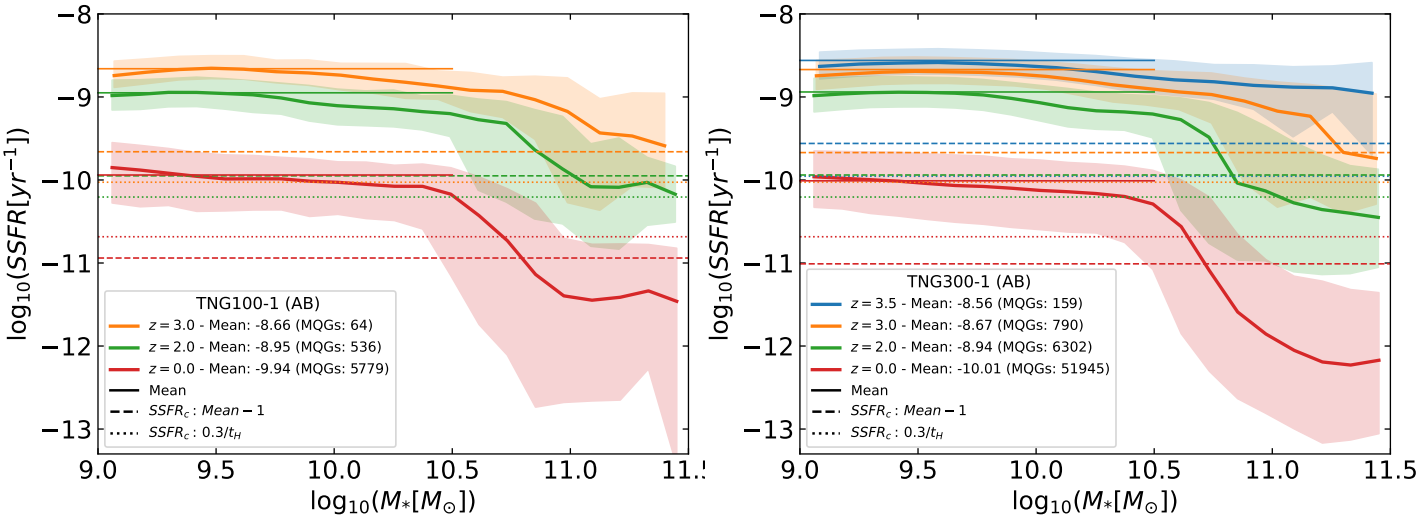


Figure 3.5: Specific star formation rate $sSFR$ versus the all-bound (AB) galaxy stellar mass ($M_\star$) at $z = 0$ (red), $z = 2$ (green), $z = 3$ (orange) and $z = 3.5$ (blue, for TNG300-1 only). For each redshift, we display the median $sSFR$ (solid evolving line) and its $16/84^{th}$ percentile range (shaded area), the mean $sSFR$ in the logarithmic mass range $9 - 10.5$ (solid vertical line), the 1dex below mean $sSFR$ (dashed line) and the $0.3/t_H$ critical $sSFR$ (dotted line). The top panel represents TNG100-1 galaxies while the bottom panel shows TNG300-1 galaxies.

definition divides galaxies as follows:

$$\text{Quiescent Galaxies}: \quad sSFR < sSFR_{MSFS} - 1\,\text{dex}$$
$$\text{Star-Forming Galaxies}: \quad sSFR > sSFR_{MSFS} - 1\,\text{dex}$$

This selection is displayed in Figure 3.5 and inspired by Genel et al., 2018's approach with $18 - 23$ non-empty logarithmic bins. For all running median $sSFR$ curves, there is a weakly downward trend which ends at $\mathcal{M} \sim 10.5$ and followed by a significant fall before stabilising after $\mathcal{M} \sim 11.0$. The global mass evolution of the $sSFR$ rises and flattens with increasing redshift. At $z = 0$, MS $- 1$ is a more conservative threshold than $0.3/t_H$ by $\sim 0.3$dex whereas the inverse is true at high redshift.

We also review the redshift evolution of both these SFG-QG separators in Figure 3.4. For context, other chosen quiescent interpretation (Ellison et al., 2015; Barro et al., 2016) are added to the figure. The MS $- 1$ threshold of $\mathcal{M} = 9.15 - 10.5$ is coherent with observational main star-forming sequences ($MSFS$) (Speagle et al., 2014; Tasca et al., 2015). $0.3/t_H$ is inferior to the upper $sSFR$ limits of color-defined quiescent galaxies (Fumagalli et al., 2014, Schreiber et al., 2018) until $z \sim 1.5$ and to MS $- 1$ until $z \sim 0.75$. This suggests the Hubble time-based criterion is adapted for quiescent galaxies at $z > 0.75$ and so will be used for the remaining of the study. With this threshold, we have $\log(sSFR(z = 2)) = -10.21$ and $\log(sSFR(z = 3)) = -10.04$. However the $MS - 1$ criterion should be considered a better option for selecting low-$z$ ($z < 0.75$) quiescent galaxies.

After this, we take a look at the $sSFR$-mass relation of quiescent and star-forming categories at $z = 3$, $z = 2$ and $z = 0$ with Figure B.1 and Figure 3.6 for TNG100-1 and TNG300-1 respectively. At high-$z$, quiescent IR (QIR) galaxies are found between $\mathcal{M} = 10.4 - 11.1$. We notice a lowering of the galaxy stellar mass of new quiescent galaxies as redshifts decreases from $z = 3$ to $z = 0$. As anticipated, the total number of galaxies is higher for the TNG300-1 run than it is for TNG100-1 since volume is about 9 times greater. This explains quiescent galaxies being up to 10 times more numerous in TNG300-1 than in TNG100-1 at all redshifts.

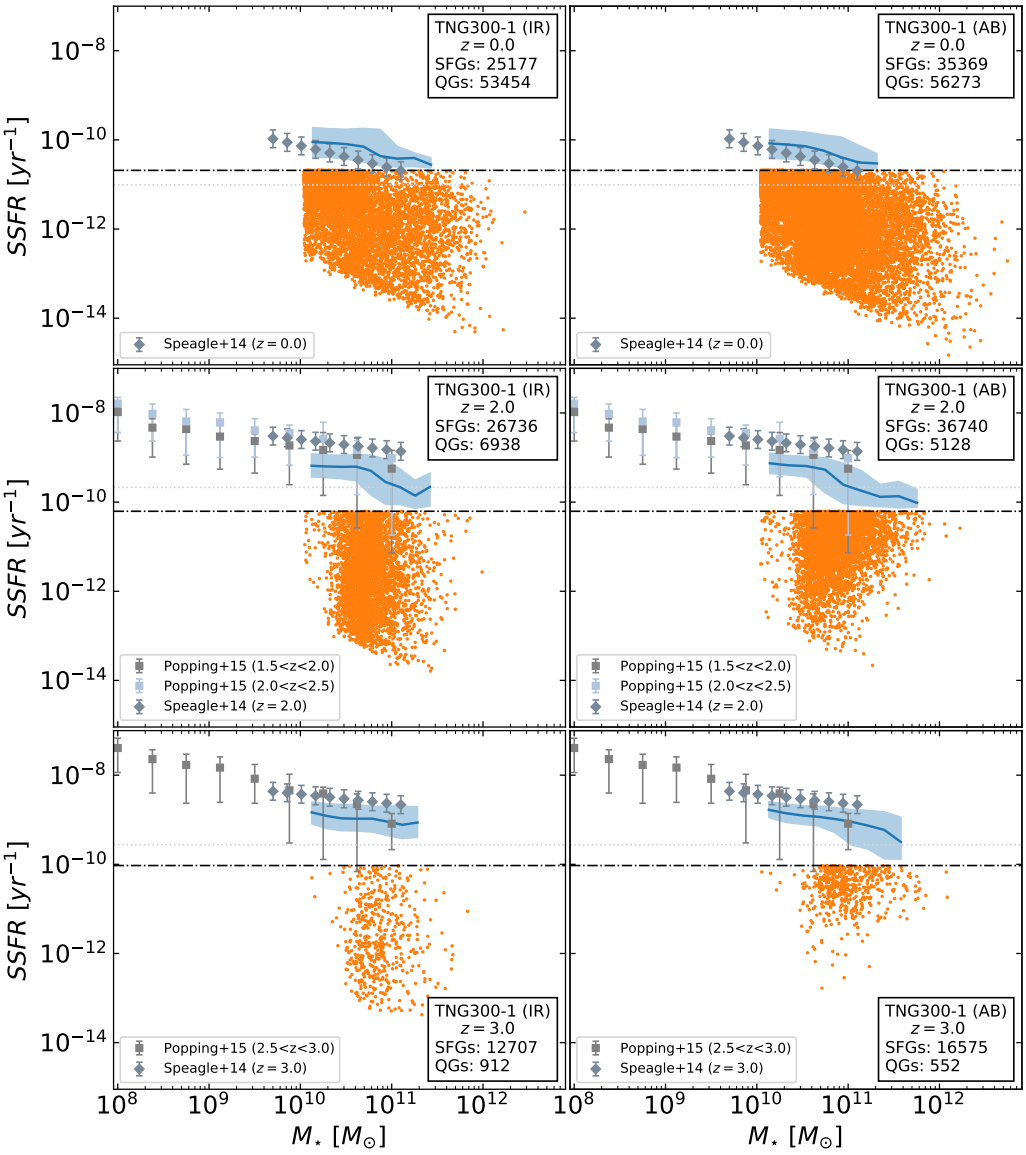


Figure 3.6: Specific star formation rate $sSFR$ distribution as a function of the in-radius (left panels) and all-bound (right panels) galaxy stellar mass ($M_\star$). In these plots, we present the $z = 0$ (top panels), $z = 2$ (center panels) and $z = 3$ (bottom panels) TNG300-1 galaxies. For each redshift, we report the median (solid blue) and the $16/84^{th}$ percentile ranges (blue shaded area) of the IllustrisTNG main star-forming sequence and quiescent galaxies (orange dots). The adopted $0.3/t_H$ critical $sSFR$ and the one using Genel et al., 2018's method are represented as black dash-dotted lines and the grey dotted lines respectively. We also show the main star-forming sequence from Speagle et al., 2014 and Popping et al., 2015's $sSFR$ distribution.

The $MSFS$ from Speagle et al., 2014 is better reproduced at $z = 0$ than at higher redshifts. At $z = 3$ and $z = 2$, the $MS - 1$ quiescent criterion because less conservative could possibly be in better agreement with observations. Data from Popping et al., 2015 corresponds to

the global $sSFR$-mass relation and so is coherent with IllustrisTNG. We can clearly see the numerical lower non-zero $sSFR$ limit that decreases with increasing galaxy stellar mass.

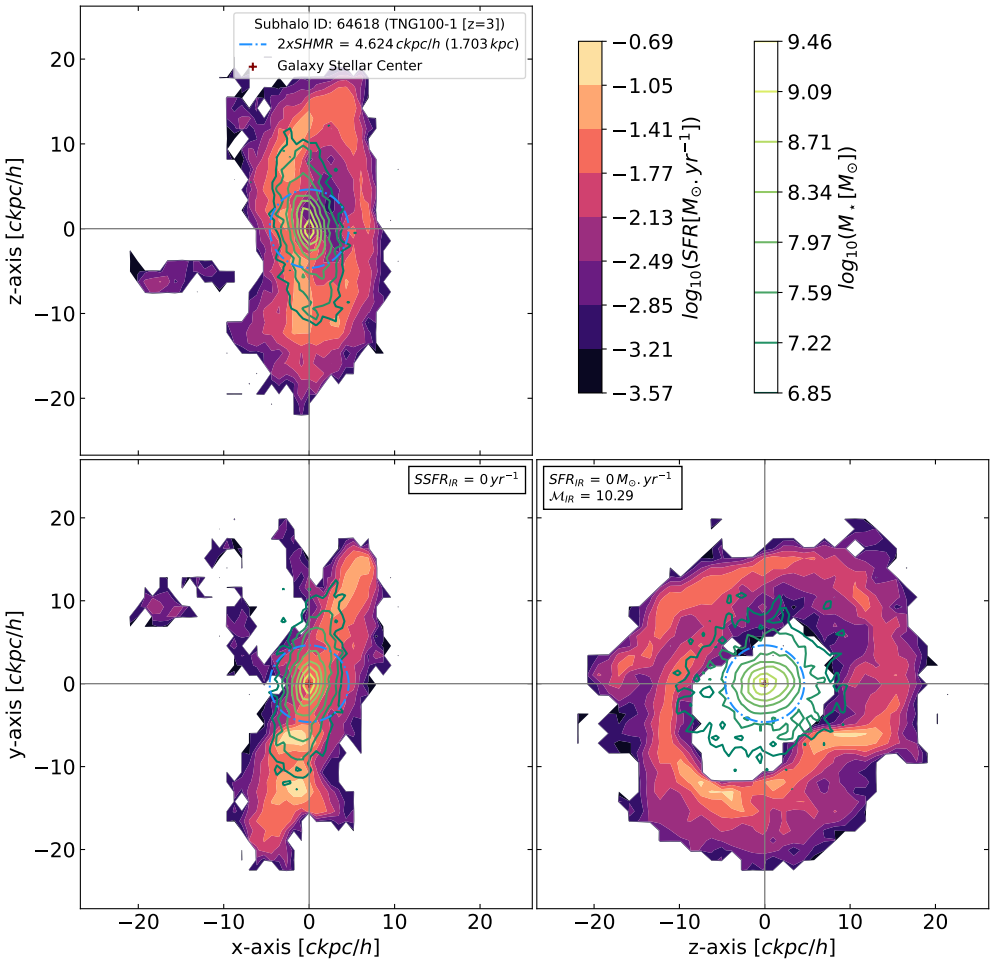


Figure 3.7: Spatial comoving distributions within $10 \times SHMR$ of the star formation rate ($SFR$) (black-to-purple-to-yellow shaded areas) and of the galaxy stellar mass ($M_\star$) (green-to-yellow contour lines). The galaxy's stellar center of mass (red symbol) is taken as the origin of all three plots. The blue circle indicates the $2 \times SHMR$ perimeter. We also specify the total $SFR$, specific $SFR$ and galaxy stellar mass within $2 \times SHMR$.

We were also attentive to the galaxy definition's impact, AB and IR, on the star-forming and quiescent classification. We selected all of the high-$z$ QIR and star-forming IR (SFIR) galaxies and extracted the $sSFR$ for the same indexed but AB-defined galaxies. A maximum of 0.05% of SFIRs are interpreted as quiescent AB (QAB) galaxies. This means that the star-forming AB (SFAB) galaxies, also selected as SFIRs, do not have significant fraction of stellar mass outside the central regions and if otherwise, it is accompanied by star formation in the outer regions. However, we also discovered 40% of TNG300-1 and 50% of TNG100-1 $z = 3$ QIRs (galaxies that are quiescent within twice $SHMR$) were also considered to be SFABs (galaxies that are star-forming under the all-bound galaxy definition). Both fractions dropped by $\sim 12\%$ at $z = 2$. These findings support the inside-out quenching scenario which

advocates the participation of black hole, for high mass galaxies, and stellar, for low mass galaxies, feedbacks in the suppression of central star formation as discussed by Nelson et al., 2019. The one (three) high-$z$ massive galaxies in Figure 3.7 (Figure A.2 and Figure A.1) are regarded as both QIR and SFAB. We detect a ring distributed $SFR$ within a $10 \times SHMR$ spherical aperture within 3% of the galaxy virial radius (Huang et al., 2017). In addition, we plot the galaxy stellar mass spatial distribution on top. For smoother contour lines, we decided to fix the lower $\mathcal{M}$ limit to 5 times the initial stellar particle mass. To better grasp these 3D distributions, we also show the same galaxy through three orthogonal projections. In Figure A.1, the reason behind the spiral structure of the star-forming region goes beyond the scope of this thesis. As it would require a closer follow-up of this galaxy's internal mechanisms.

All findings presented above lead us to affirm the necessity for a cautious choice of definitions of quiescence and of galaxy aperture. As seen earlier, both of them significantly affect the QG and SFG populations and IllustrisTNG's ability to duplicate observational properties of each population.

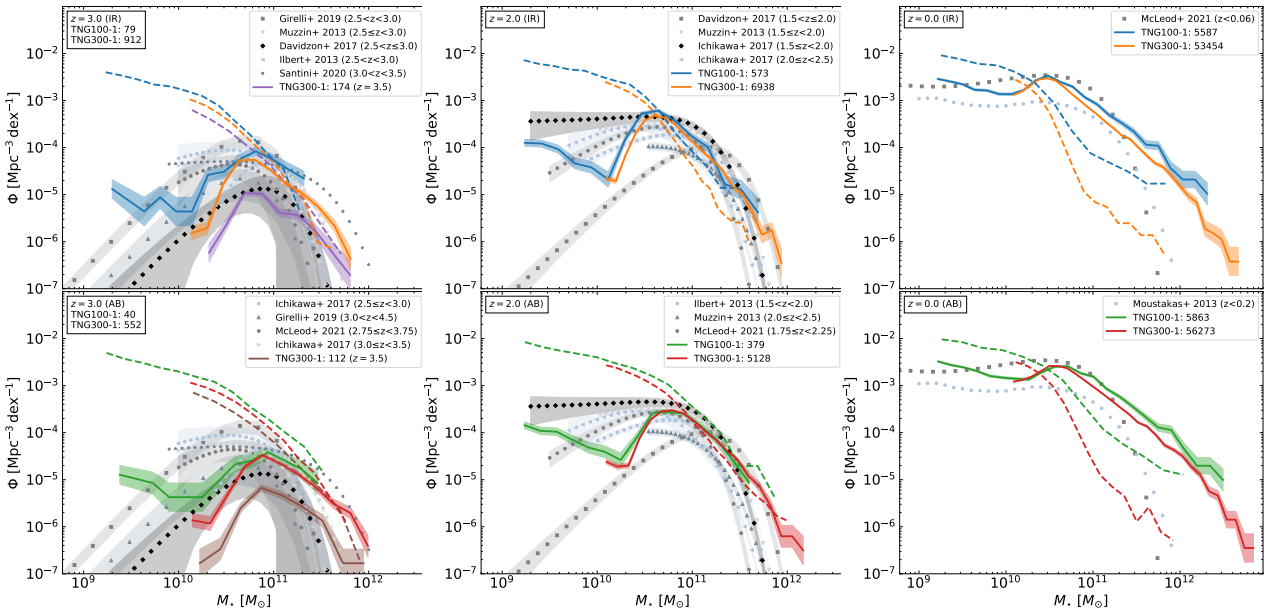


Figure 3.8: Quiescent (solid) and star-forming (dashed) galaxy stellar mass functions (GSMF) at $z = 0$ (right panels), at $z = 2$ (center panels) and at $z = 3$ (left panels). Two distinct GSMFs are drawn for both TNG100-1 (blue and green) and TNG300-1 (orange, red, purple and brown) for all-bound (AB) galaxies (bottom panels) and in-radius (IR) galaxies (top panels) as well as their associated Poisson error range. For each redshift, we specify the number of galaxies used for each GSMF calculations. A few simple and double Schechter function fits of observational data points are plotted with grey, blue and black symbols (Santini et al., 2020) with error-propagated uncertainty range (Girelli et al., 2019; Muzzin et al., 2013; Davidzon et al., 2017; Ilbert et al., 2013; Ichikawa et al., 2017; McLeod et al., 2021; Moustakas et al., 2013).

### 3.2.2 Quiescent Galaxy Stellar Mass Functions

Next, we investigate the quiescent and star-forming GSMFs at $z = 0$, $z = 2$ and $z = 3$ to test IllustrisTNG quiescent-defined galaxies coherence with observations. The same method used for the global GSMF is applied here with the exception this time of the display of all non-empty logarithmic stellar mass bins. The entire quiescent GSMF curves moved to higher values with decreasing redshift. The star-forming GSMFs indicate a similar evolution although much less apparent. With cosmic time, the quiescent GSMFs close the gap with the star-forming ones until it dominates beyond the characteristic Schechter mass $M_{CS}$ at $z = 2$. For the low mass end at $z = 0$, it is within 0.6dex. This is accompanied by a visible decline of $\mathcal{M}_{CS}$ from $\sim 10.9$ at $z = 3$ to $\sim 10.5$ at $z = 0$. From $z = 3$ to 2, there seems to be a slight steepening of the high-mass end slopes.

As said in Peng et al., 2010, the double Schechter function, associated to the quiescent group, is induced by two separate quenching mechanisms: one environment-related, which includes merger and satellite quenching, for low mass galaxies and one mass-associated for massive galaxies. For low-mass galaxies, satellite quenching becomes more predominant at low redshift as satellite galaxies migrate towards the center of large structure that develop with time. The mass quenching rate $\eta$ for massive galaxies is expected be proportional to $SFR$ in other words: $\eta \approx SFR/M_{CS}$ with $M_{CS}$ acting as a star-formation cut-off mass (Peng et al., 2010). This likely causes a decline of the high-mass end exponent with time because of a piling up of new massive quiescent galaxies around $M_{CS}$. This leads to GSMF maximums at low-mass and around $M_{CS}$. Our GSMFs coincide with Peng et al., 2010's insight on the shape and evolution of the GSMF of the QG population.

The quiescent IR GSMF curves are more consistent with observations than the quiescent AB GSMFs. This is likely due to the reason presented earlier (section 3.1). In Figure 3.4, the $0.3/t_H$ criterion was shown to lead to inconsistencies, between observations and the high-mass end of the GSMFs of the QG population at $z = 0$. Indeed, we found that massive galaxies with $sSFR$s between $MS - 0.7$ and $MS - 1$ were included into the quiescent population.

### 3.2.3 Quiescent Galaxy Fractions

We also check how well our fraction of quiescent galaxies $f_{QG}$ replicate observational fractions of this galaxy population at $z = 0$, $z = 2$ and $z = 3$. At first, we work on the mass evolution of $f_{QG}$ at these different redshifts (Figure 3.9). Since we are interested in the high-$z$ massive quiescent galaxies, we set a minimum galaxy stellar mass of $10^{10} M_{\odot}$. For each logarithmic mass bin, we calculated $f_{QG}$ using the number of quiescent $N_{QG}$ and total $N_G$ (quiescent and star-forming combined) galaxies per bin and a Poisson error range of $f_{QG}$ with error propagation providing $\sigma_{FQG} = \sqrt{2N_{QG}}/N_G$. We constrained the error range of $f_{QG}$ so that the lower Poisson error may not be below 0 and that the upper Poisson error may not be above 1. The physical reality of the $f_{QG}$ and of its associated error requires such constraints (0 to 1). We computed $f_{QG}$ for AB, IR galaxies with both quiescent criteria and so obtained four distinct curves. The $f_{QG}$ from TNG300-1 are systematically greater than those from TNG100-1. This appears to show that a larger simulation volume allows for the development of stronger quenching processes particularly for $\mathcal{M} > 11$ galaxies. At all redshifts, $f_{QG}$ grows with galaxy stellar mass, most dramatically for $10 < \mathcal{M} \lesssim 11$, and more steeply with decreasing redshift. At $z = 3$, $f_{QG}$ increases rather linearly. Super massive galaxies are most representative of the quiescent $z = 3$ population. Yet, with time, more and more lower mass galaxies join the quiescent sample. This is as if quiescent processes were mass-dependant (Domínguez Sánchez et al., 2011). They first affect the most massive galaxies before appearing in lesser and lesser massive galaxies. This trend is one aspect of what is often referred to as galaxy downsizing or anti-hierarchical trend in galaxy evolution. At $z = 0$, $f_{QG}$ reaches a plateau at $\mathcal{M} \sim 11$ between 0.8 and 1. Overall, the AB galaxy definition best reproduces high-$z$ observations.

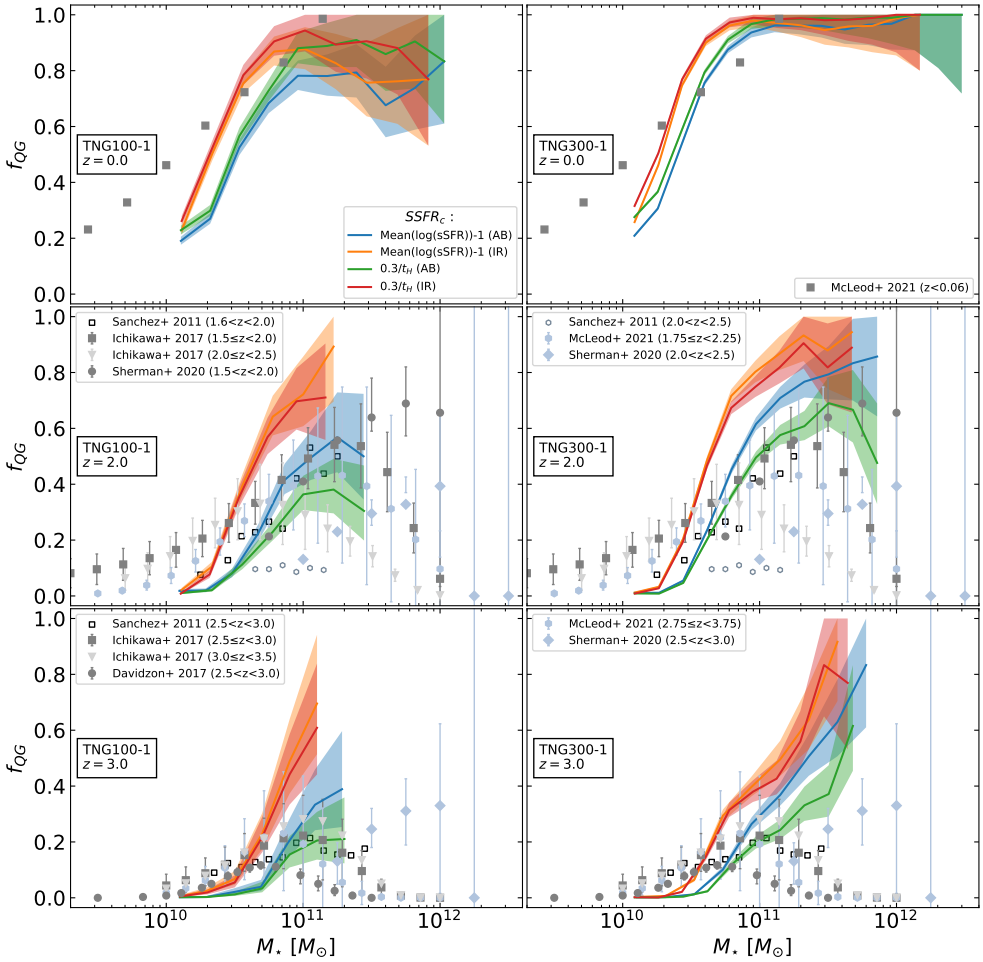


Figure 3.9: Fraction of quiescent galaxies ($f_{QG}$) in terms of galaxy stellar mass ($M_\star$) at $z = 0$ (top panels), $z = 2$ (center panels) and $z = 3$ (bottom panels). For each redshift and for both TNG100-1 (left panels) and TNG300-1 (right panels) galaxies, we distinguish four categories: all-bound galaxies (blue, green), in-rad galaxies (orange, red) using Genel et al., 2018's criterion and the $0.3/t_H$ $sSFR_c$ respectively. For each $f_{QG}$ category, we report the associated Poisson error range. Observational data points of this quiescent fraction are specified in grey, blue and black symbols (McLeod et al., 2021; Domínguez Sánchez et al., 2011; Ichikawa et al., 2017; Sherman et al., 2020; Davidzon et al., 2017).

This is somewhat striking as some observations (McLeod et al., 2021) use the half light radius which is more analogous to the IR definition than it is to the AB. Additionally, we notice large error ranges in the estimations of the quiescent galaxy fractions in the high-mass end in both our results and observations (Sherman et al., 2020; McLeod et al., 2021). This is due to the combination of small highly massive QG samples and to errors being dominated by Poisson errors.

Finally, we obtained the redshift evolution of the $f_{QG}$ from $z = 3.5$ to $z = 0$ (Figure 3.10). For this evolution, we selected only the $\mathcal{M} \geqslant 11$ quiescent galaxies. The AB quiescent galaxies produce a $f_{QG}$ curve more consistent with observations. This is despite the AB galaxy definition ever being used, in published observational literature, due to galaxy aperture

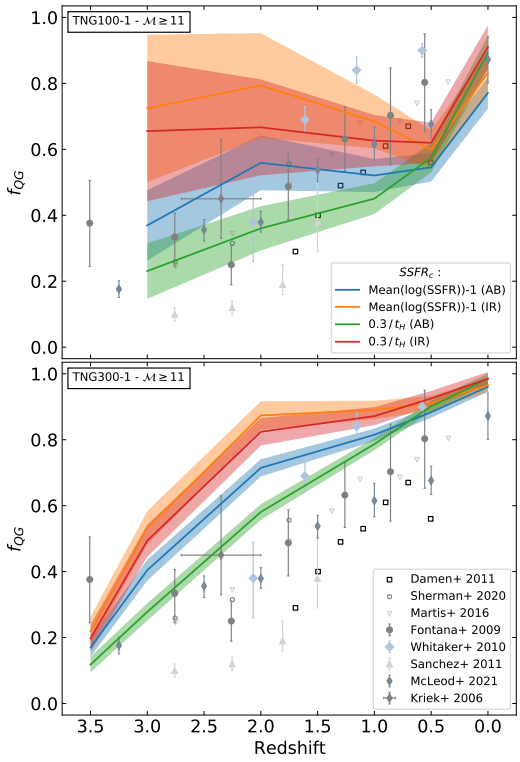


Figure 3.10: Redshift evolution of the fraction of quiescent galaxies ($f_{QG}$) with galaxy stellar masses of at least $10^{11}\,M_\star$. For both TNG100-1 (left panels) and TNG300-1 (right panels) quiescent galaxies, we distinguish four categories: all-bound galaxies (blue, green), in-rad galaxies (orange, red) using Genel et al., 2018's criterion and the $0.3/t_H$ $sSFR_c$ respectively. For each $f_{QG}$ category, we report the associated Poisson error range. Observational data points of this quiescent fraction are specified in grey, blue and black symbols (Damen et al., 2011; Sherman et al., 2020; Martis et al., 2016; Fontana et al., 2009; Whitaker et al., 2010; Domínguez Sánchez et al., 2011; McLeod et al., 2021; Kriek et al., 2006).

limitations. For TNG100-1 galaxies, the fraction has a two phase increase with decreasing redshift. $z = 1 - 0.5$ is the turning point between an earlier constant or weak increase and a later steeper rise. For TNG300-1, the order of the stages are flipped and the decisive epoch is at $z = 2$. However these two phases are not distinguishable for $0.3/t_H$ AB quiescent galaxies as rises linearly between $z = 3.5$ and $z = 0$. The global trend is better replicated by TNG100-1 as TNG300-1 once again over predicts the fraction.

For the observational $f_{QG}$, the galaxy stellar masses considered are $\mathcal{M} \geqslant 10.85$ (Fontana et al., 2009; Domínguez Sánchez et al., 2011), $\mathcal{M} \geqslant 11$ (Kriek et al., 2006; Whitaker et al., 2010; Damen et al., 2011), $\mathcal{M} = 11$ (Sherman et al., 2020), $10.55 \leqslant \mathcal{M} \leqslant 13$ (McLeod et al., 2021) and $10.9 \leqslant \mathcal{M} \leqslant 11.2$ (Martis et al., 2016). The quiescent fractions were deduced from either the ratio of the stellar mass density of QGs and of all galaxies (McLeod et al., 2021), the ratio of the quiescent and of the global $GSMF$ (Ichikawa et al., 2017) or the ratio of the number of quiescent galaxies and of the total number of galaxies (Damen et al., 2011; Domínguez Sánchez et al., 2011; Martis et al., 2016; Sherman et al., 2020).

### 3.2.4 Physical Properties of Quiescent Galaxies

#### Stellar Half Mass Radii

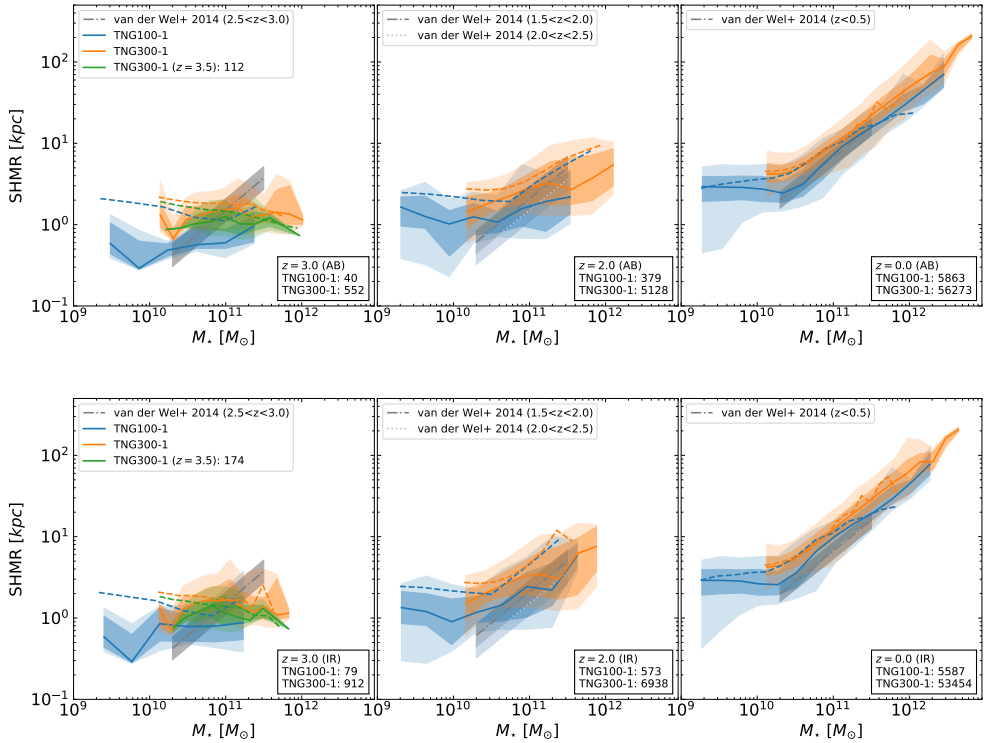


Figure 3.11: Stellar half mass radius (SHMR) of quiescent (solid) and star-forming (dashed) galaxies at $z = 3 - 3.5$ (left panels), $z = 2$ (center panels) and $z = 0$ (right panels) versus galaxy stellar mass ($M_\star$). For both TNG100-1 and TNG300-1 galaxies, we show the median, the $16^{th}/84^{th}$ and the $2^{nd}/98^{th}$ percentile ranges of all-bound (top panels) and in-radius (bottom panels) galaxies. The number of quiescent galaxies is indicated next to each simulation name. A few observational data points are plotted in grey lines with their error-propagated uncertainty range from van der Wel et al., 2014.

We are also interested in how well our two types of quiescent-defined galaxies reproduce the observations of galaxy effective radius. Initially, we study the size-mass relation at high and low redshifts (Figure 3.11) before continuing with the redshift evolution of the galaxy size (Figure 3.12). As said previously in Pillepich et al., 2018b, the global IllustrisTNG size-mass relation is calibrated to concur with $z = 0$ observations and so it does. We notice, already at $z = 2$, a gradual growth of the stellar half mass radius with stellar mass after $\mathcal{M} = 10.5$. At $z = 3.5 - 3$, the quiescent and star-forming selected sizes seem to be mass-independant and the $SHMR$ oscillates around $0.7 - 2$kpc. This is evidence of IllustrisTNG's inability to imitate observed mass-size relations at early times ($z = 3$). Star-forming galaxies remain in most cases less compact than quiescent ones even at lower redshifts. At all masses and redshifts, TNG300-1 returns star-forming and quiescent galaxy of greater sizes, by up to 0.4dex, than those from TNG100-1. This is a clear resolution effect: it is an artificial numerical effect and not physical effect. Given the higher resolution of TNG100, the galaxy sizes of both populations should be more reliable. This is a clear resolution effect (i.e. it's an artificial numerical effect, and not physical). Given the higher resolution of TNG100, the corresponding should be more reliable.

van der Wel et al., 2014 observations are related to an effective radius that takes into account half the total flux radius. For context, the average half-mass radius can represent

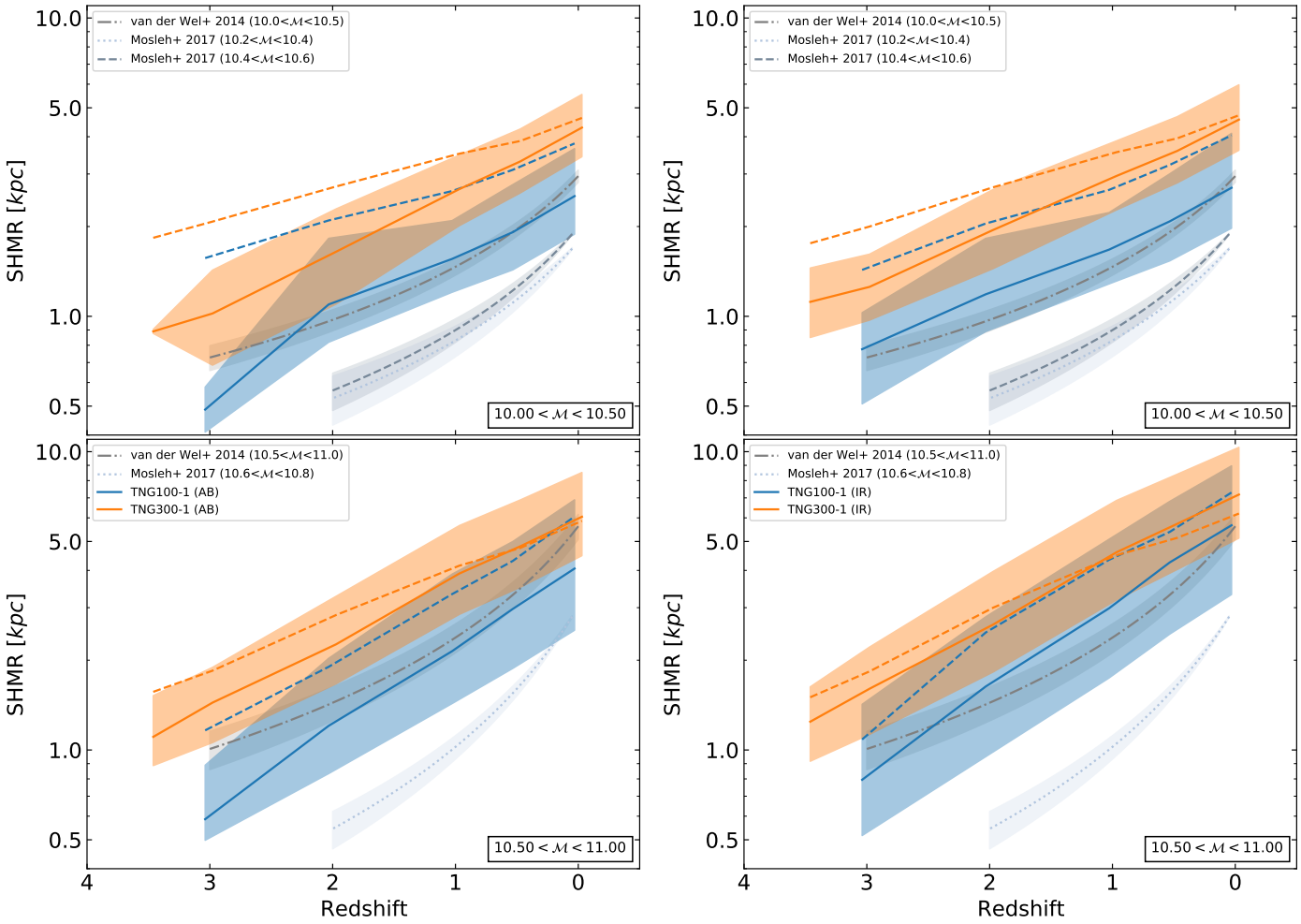


Figure 3.12: Redshift evolution of the stellar half mass radius (SHMR) of quiescent (solid) and star-forming (dashed) galaxies. For both TNG100-1 and TNG300-1 galaxies, we show the median and the $16^{th}/84^{th}$ percentile ranges of all-bound (left panels) and in-radius (right panels) galaxies. Galaxies shown are sorted into two galaxy stellar mass bins. A few observational data points are plotted in grey lines with their uncertainty range (van der Wel et al., 2014; Mosleh et al., 2017).

$30 - 50\%$ of the half light radius[3] (Mosleh et al., 2017). These estimated radii may vary according to the band filter. Genel et al., 2018 finds the IllustrisTNG size-mass relation to be coherent with $z = 2 - 0$ observations and so does ours.

The median $SHMR$ of two massive quiescent populations has more than tripled between $z = 3$ and $z = 0$. This is coherent with the stellar mass behaviour of QGs. Indeed, it has been observed that QGs become less and less compact with cosmic time as well as experience an expulsion of the central star formation towards the outer regions already at $z < 2.5$ (see subsection 1.4.3, Tacchella et al., 2017). The IR galaxies tend to be slightly larger than AB galaxies which generates less agreement with the measurement of the half total flux radius from van der Wel et al., 2014 and the half mass radius from Mosleh et al., 2017 of quiescent

[3]The half light radii were inferred with $H_{160}$ band for early-type galaxies

galaxies and so does TNG300-1 with regards to TNG100-1 by up to 0.3dex. The star-forming galaxies are constantly larger than passive ones. With time, the star-forming group grows in sizes and later on fills up the ranks of the quiescent category as their star formation is quenched.

### Velocity Dispersion

The velocity dispersion $\sigma_e$ associated to each galaxy corresponds to a one directional velocity dispersion estimated using all of the simulated particle and cells bound to it. The one directionality of the velocity dispersion is obtained by dividing the 3D dispersion velocity by a factor $\sqrt{3}$. We included all non-empty bins. For each redshift, we detect a rising of the velocity dispersion with increasing stellar mass and little scatter (Figure 3.13). Star-forming and quiescent galaxies are barely differentiable with regards to the mass evolution of $\sigma_e$ with the exception of less massive galaxies. For such galaxies, the gap is reduced from 0.5dex at $z = 3$ to $< 0.1$dex. Both TNG100-1 and TNG300-1 replicate some of the estimated stellar $\sigma_e$ of observed galaxies (Mendel et al., 2020; Stockmann et al., 2020; Esdaile et al., 2021). Yet again, AB galaxies with lower $\sigma_e$ than the IR ones are closer to observations. Due to the large scatter in the observations of $\sigma_e$, it is hard to make a concrete conclusion about an evolution in observations and to determine to what extent simulation predictions are consistent with observations. They certainly fail to predict a large enough scatter at a given mass bin. This can also point towards some short-comings in the simulations.

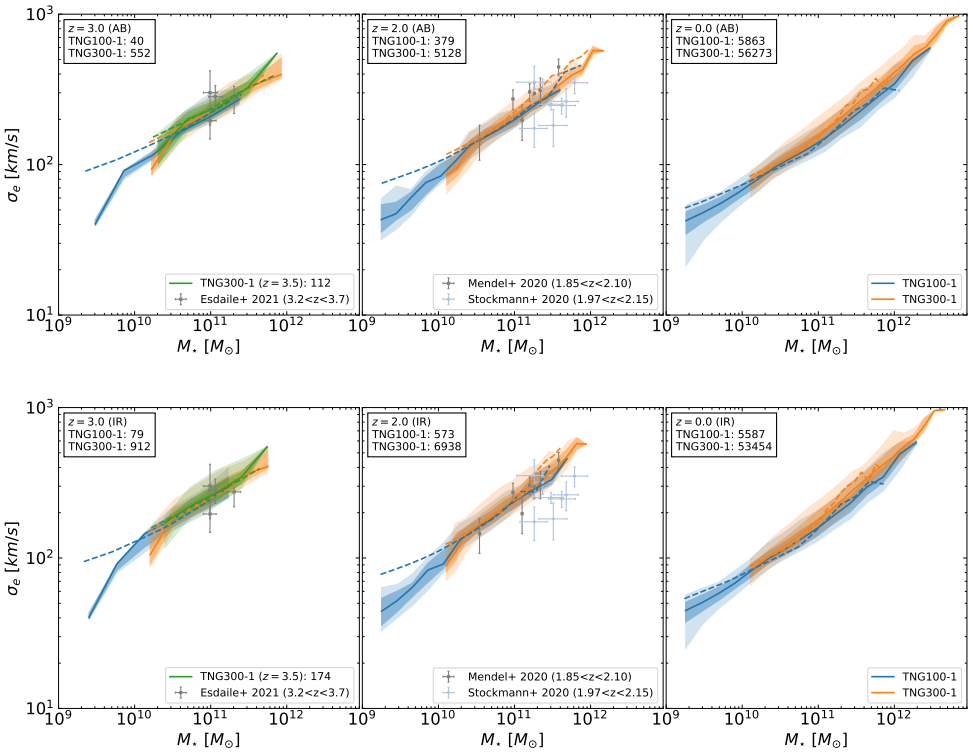


Figure 3.13: One dimensional velocity dispersion ($\sigma_e$) distribution of quiescent (solid) and star-forming (dashed) galaxies at $z = 3 - 3.5$ (left panels), $z = 2$ (center panels) and $z = 0$ (right panels) in terms of galaxy stellar mass ($M_\star$). For both TNG100-1 and TNG300-1 galaxies, we show the median, the $16^{th}/84^{th}$ and the $2^{nd}/98^{th}$ percentile ranges of all-bound (top panels) and in-radius (bottom panels) galaxies. The number of quiescent galaxies is indicated next to each simulation name. A few observational data points are plotted in grey and blue symbols with their uncertainty range (Esdaile et al., 2021; Mendel et al., 2020; Stockmann et al., 2020).

Afterwards, we divided our massive quiescent and star-forming sample into three galaxy stellar mass bins (Figure 3.14). On this occasion, IR quiescent galaxies were more consistent with $\sigma_e$ observations than AB passive galaxies. Since the IR galaxy definition is more alike the one chosen in observations than the AB one, it was expected that the $\sigma_e$ of IR-defined IllustrisTNG galaxies match those of observed galaxies more closely than those of AB galaxies. Hence our expectations were verified. Overall, the redshift evolution of the $\sigma_e$ decreases by $< 0.3$ dex with decreasing redshift. We also find that the more massive a galaxy, the greater the $\sigma_e$ is. $\sigma_e$ from TNG100-1 are slightly lower than those from TNG300-1. This is undoubtedly due to TNG100's high resolution.

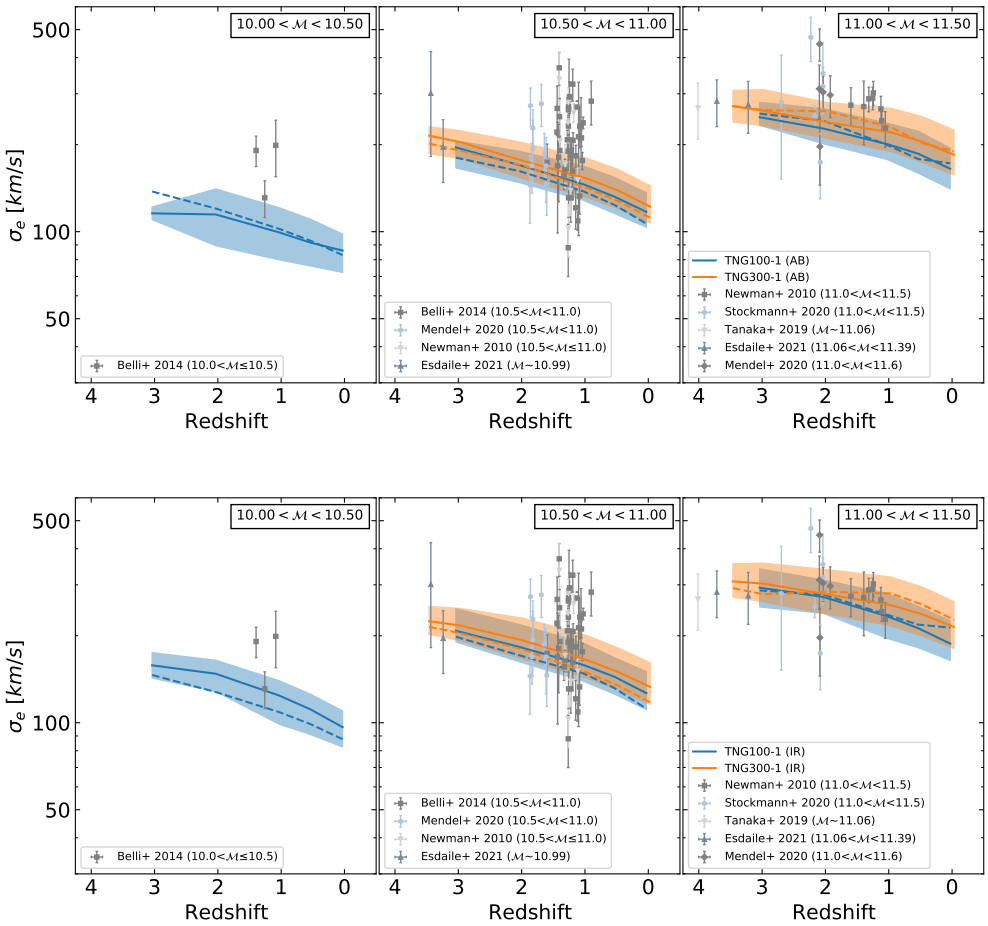


Figure 3.14: Redshift evolution of the one dimensional velocity dispersion ($\sigma_e$) of quiescent (solid) and star-forming (dashed) galaxies. For both TNG100-1 and TNG300-1 galaxies, we show the median and the $16^{th}/84^{th}$ percentile ranges of all-bound (top panels) and in-radius (bottom panels) galaxies. Galaxies shown are sorted into three galaxy stellar mass bins. A few observational data points are plotted in grey lines with their uncertainty range (Belli et al., 2014; Mendel et al., 2020; Newman et al., 2010; Esdaile et al., 2021;Stockmann et al., 2020; Tanaka et al., 2019).

### Velocity-Size Planes

Subsequently, we show the $\sigma_e$-$SHMR$ planes for all quiescent and star-forming galaxies with stellar masses above or equal to the critical galaxy stellar mass resolution adopted for TNG300-1. We split them into three galaxy stellar mass bins (Figure 3.15). We display all $SHMR$ bins with at least 7 counts.

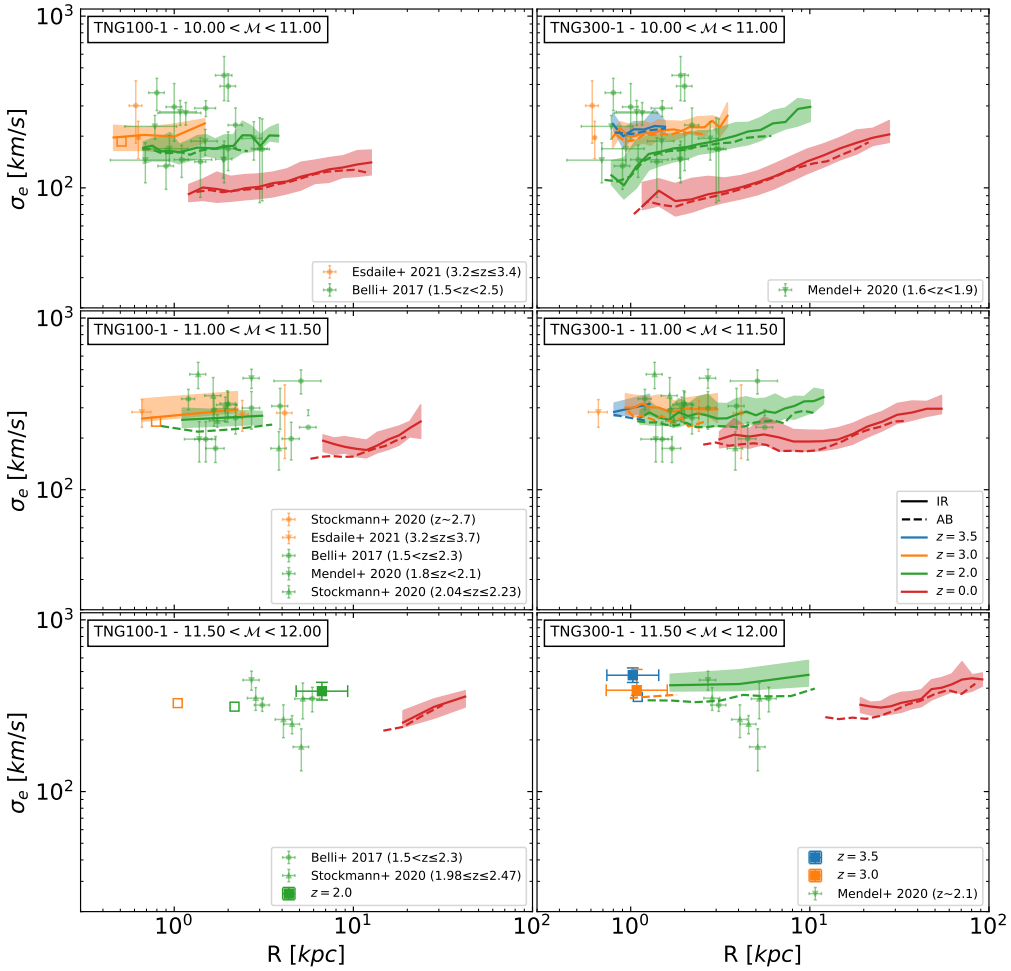


Figure 3.15: One dimensional velocity dispersion ($\sigma_e$) distribution of $z = 3.5 - 0$ quiescent galaxies in terms of the stellar half mass radius (SHMR) a characteristic radius (R). For both TNG100-1 (left panels) and TNG300-1 (right panels) galaxies, we show the median and the $16^{th}/84^{th}$ percentile ranges (in colored areas or in error bars if only one SHMR bin) of in-radius (solid) galaxies. Regarding all-bound (dashed) galaxies, we report only the median $\sigma_e$. All selected galaxies are sorted into three galaxy stellar mass bins. Half-light radius observational data points are also plotted in colored symbols with their uncertainty range (Esdaile et al., 2021; Belli et al., 2017; Belli et al., 2014; Mendel et al., 2020; Stockmann et al., 2020).

If the $\sigma_e - R$ plane is not divided into stellar mass bins, we report a mass dependency of this relation which intensifies with decreasing redshift. There is no pattern in terms of differences between IR and AB galaxies. For TNG300-1, the whole plane seems to be shifted to higher $SHMR$ and $\sigma_e$ and there is less scatter. In Figure 3.15, quiescent $\sigma_e$ and $SHMR$ are less correlated in TNG100 than in TNG300. The growth of $\sigma_e$, as a function of $SHMR$, flattens and the spread range of $SHMR$ narrows with decreasing redshift. These trends can be understood as the result of the quenching of more different types of massive galaxies as cosmic time roles out. They could be supported by the individual mass growth and quenching of the small low mass SFG population at high redshift as shown by (Figure 3.8). This is in

contradiction with the tendencies revealed by some observations. There is more diversity, in terms of $H\,\alpha$ emission lines, morphology and velocity dispersion, amongst the population of massive ($> 10^{11} M_{\odot}$) galaxies at high redshift ($1 < z < 1.5$) than can be observed in the local universe (van Dokkum et al., 2011). In time, more of these massive galaxies not yet quenched at $1 < z < 1.5$, will evolve to become quiescent (as seen in Figure 3.8). It appears that lower mass bins produce broader $SHMR$ ranges and steeper $\sigma_e$-$SHMR$ relations. Mass binning also improves the overlap of IllustrisTNG predictions and observations. This may be due to larger numbers of less massive QG populations than of more massive QG groups. The AB and IR relations are almost the same with IR galaxies sometimes having higher median $\sigma_e$. All of the observations are of half light radius and stellar velocity dispersion. This as well as the use of the 1D $\sigma_e$ could explain our under prediction of this relation and little scatter.

| **Simulation Name** | **Galaxy Type** | **Galaxy Definition** | $\mathcal{M}_1$ 10.0-10.5 | $\mathcal{M}_2$ 10.5-11.0 | $\mathcal{M}_3$ 11.0-11.5 | $\mathcal{M}_4$ 11.5-12.0 |
|---|---|---|---|---|---|---|
| TNG100-1 ($z = 2$) | Quiescent | All-bound | 18 (54.5%) | 99 (55.3%) | 38 (67.9%) | - |
| | | In-radius | 61 (51.7%) | 178 (56.9%) | 31 (77.5%) | - |
| | Star-forming | All-bound | 1164 (59.4%) | 422 (59.9%) | 65 (68.4%) | - |
| | | In-radius | 985 (60.3%) | 194 (61.2%) | 14 (73.7%) | - |
| TNG300-1 ($z = 2$) | Quiescent | All-bound | 150 (34.6%) | 2075 (59.6%) | 789 (71.1%) | - |
| | | In-radius | 647 (48.8%) | 3013 ( (62.4%) | 559 (75.3%) | - |
| | Star-forming | All-bound | 16088 (60.1%) | 5612 (61.8%) | 569 (69.6%) | - |
| | | In-radius | 13437 (60.2%) | 2657 (62.7%) | 107 (66.9%) | - |
| TNG100-1 ($z = 3$) | Quiescent | All-bound | - | 10 (58.8%) | 8 (57.1%) | - |
| | | In-radius | - | 26 (63.4%) | 15 (78.9%) | - |
| | Star-forming | All-bound | - | 152 (53.9%) | 33 (70.2%) | - |
| | | In-radius | - | 82 (54.5%) | 6 (60.0%) | - |
| TNG300-1 ($z = 3$) | Quiescent | All-bound | - | 160 (51.3%) | 135 (69.9%) | 24 (82.8%) |
| | | In-radius | - | 363 (55.1%) | 142 (76.3%) | 14 (82.4%) |
| | Star-forming | All-bound | - | 2345 (56.9%) | 363 (65.5%) | 26 (92.9%) |
| | | In-radius | - | 1399 (58.9%) | 145 (70.7%) | 3 (100%) |

Table 3.1: Number (and kept relative fraction) of main branch $z = 2$ and $z = 3$ galaxies for each galaxy category and galaxy stellar mass bin $\mathcal{M}_i$.

For a given radius, at high-$z$ and $\mathcal{M}$ between $10-11$, the observed stellar velocity dispersion has a much larger scatter compared to our results from IllustrisTNG simulations. Secondly, we observe that the IllustrisTNG simulation does not manage to predict as high velocity dispersion as the ones resulting from observations. This may point towards some short-coming of the simulations. Instead for most massive galaxies, at a given radius, the velocity dispersion, in IllustrisTNG galaxies, tends to be over-estimated. A deeper understanding of the origin of these discrepancies is needed, but that goes beyond the scope of this thesis.

## 3.3 Origin of Massive Quiescent at High-Redshift

We have seen in the last subsections, that we have a generally fair agreement between the statistics and properties of high-z MQGs in IllustrisTNG and current observational data. Thus, in this subsection, we can go a step further and take advantage of the merger trees to explore what the origin of MQGs at $z = 2 - 3$ is, i.e. which are the main physical processes driving this quenching of star-formation so early in time. In the following subsections, we will, specifically, investigate the role of feedback from accreting black holes and the time at which

black holes start growing in galaxies (in subsection 3.3.2) as well as the role of merger events (in subsection 3.3.3) for the quenching. These are some of the processes most often discussed in literature.

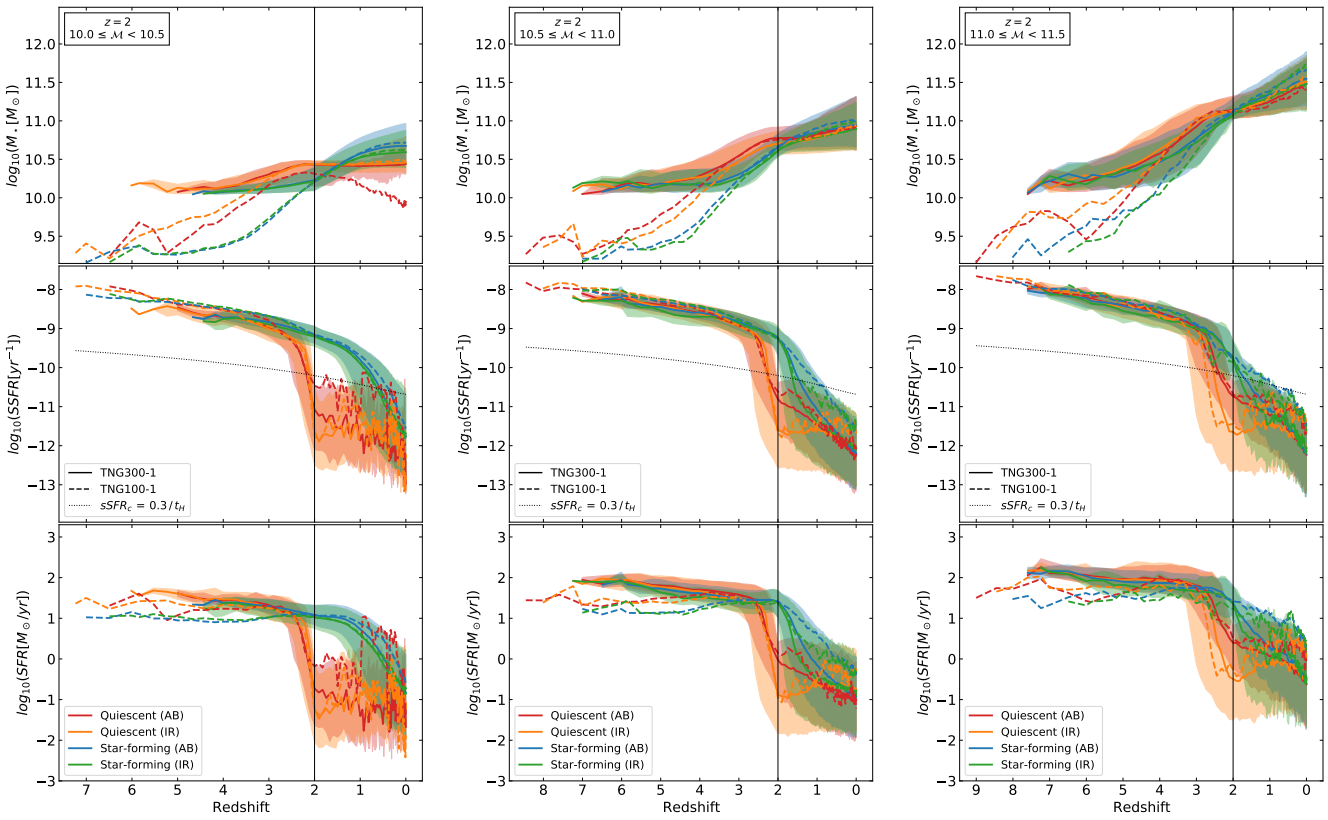


Figure 3.16: Redshift evolution of the galaxy stellar mass ($M_\star$) (top panels), the specific star formation rate ($sSFR$) (center panels) and the star formation rate ($SFR$) (bottom panels). We report these characteristics for TNG300-1 (solid) and TNG100-1 (dashed), quiescent (red and orange) and star-forming (blue and green) at $z = 2$, all-bound and in-radius galaxies. The selected galaxy stellar mass bin is specified in the top panel. For each sub-figure, the median is shown by a solid evolving line and the $16^{th}/86^{th}$ percentile range by a colored area. The dotted curve in the center panels represents the $sSFR_c = 0.3/t_H$ limit. The solid vertical black line marks the redshift at which these galaxies are quiescent or star-forming.

Using IllustrisTNG subhalo merger trees, we identify the descendants and progenitors belonging to the main branch of the $z = 0$ descendants of $z = 2$ and $z = 3$ quiescent and star-forming galaxies. Once identified, we extract certain galaxy characteristics which we then plot in terms of redshift. This allows the visualisation of the change of each of these characteristics. The characteristics we have chosen to look at first are: the galaxy stellar mass, the $sSFR$, the $SFR$, the black hole mass $M_{BH}$, the Eddington ratio $f_{Edd}$ and the AGN luminosity $L_{AGN}$.

In Table 3.1, we present the number of $z = 2$ and $z = 3$ galaxies used for every galaxy stellar mass bin and galaxy categories. To facilitate our analysis, we kept $z = 2$ and $z = 3$ galaxies that belong to the main branch with the most massive history. This ensures that none of these galaxies have common $z < 2$ or $z < 3$ descendants since there can only be one

main progenitor branch for each $z = 0$ descendant. This relative fraction of galaxies retained for each galaxy group is also provided in Table 3.1.

In addition, we excluded, from the median and the $16^{th}/84^{th}$ percentile ranges calculations, progenitor and descendant galaxies with galaxy stellar masses $\mathcal{M}_\star$ below 9.15 for TNG100-1 and 10.04 for TNG300-1 as well as all zero values.

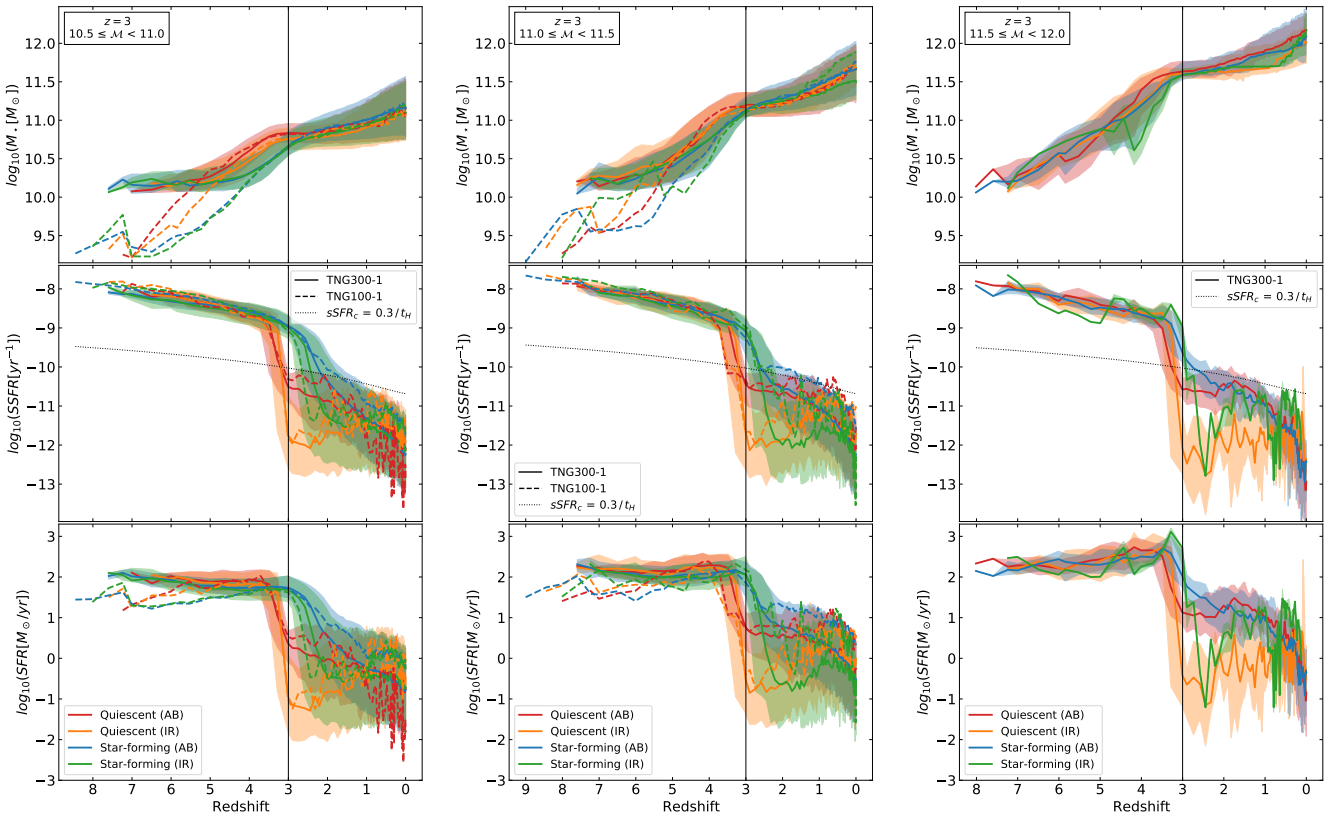


Figure 3.17: Redshift evolution of the galaxy stellar mass ($M_\star$) (top panels), the specific star formation rate ($sSFR$) (center panels) and the star formation rate ($SFR$) (bottom panels). We report these characteristics for TNG300-1 (solid) and TNG100-1 (dashed), quiescent (red and orange) and star-forming (blue and green) at $z = 3$, all-bound and in-radius galaxies. The selected galaxy stellar mass bin is specified in the top panel. For each sub-figure, the median is shown by a solid evolving line and the $16^{th}/86^{th}$ percentile range by a colored area. The dotted curve in the center panels represents the $sSFR_c = 0.3/t_H$ limit. The solid vertical black line marks the redshift at which these galaxies are quiescent or star-forming.

### 3.3.1 Redshift Evolution of Galaxy Properties

First off, we work on the redshift evolution of the galaxy stellar mass, the $sSFR$ and the $SFR$ for three different $z = 2$ and $z = 3$ galaxy stellar mass bins (Figure 3.16 and Figure 3.17). At $z \sim 2.5$ ($z \sim 3.5$) for $z = 2$ ($z = 3$), the progenitors of quiescent galaxies start seeing their $sSFR$ drop before reaching quenched levels. The quiescent galaxy stellar mass growth, on the other hand, begins at higher redshifts than the galaxy stellar mass growth of SFGs. This stellar mass growth has two phases with $z = 2$ and $z = 3$ being the changing redshifts.

Therefore the progenitors of quiescent galaxies at $z = 2$ and $z = 3$ start to assemble their stellar mass more quickly and earlier than the progenitors of their star-forming analogues. The rise in the first phase is more dramatic than in the second. At that same epoch, the star formation rate drops considerably before stabilising allowing the stellar mass to increase but this time less intensely as the $SFR$ weaker. The majority of the $z = 0$ descendants of $z = 3$ and $z = 2$ galaxies appear to be quiescent.

### 3.3.2 Redshift Evolution of Black Hole Properties and Role of Black Holes

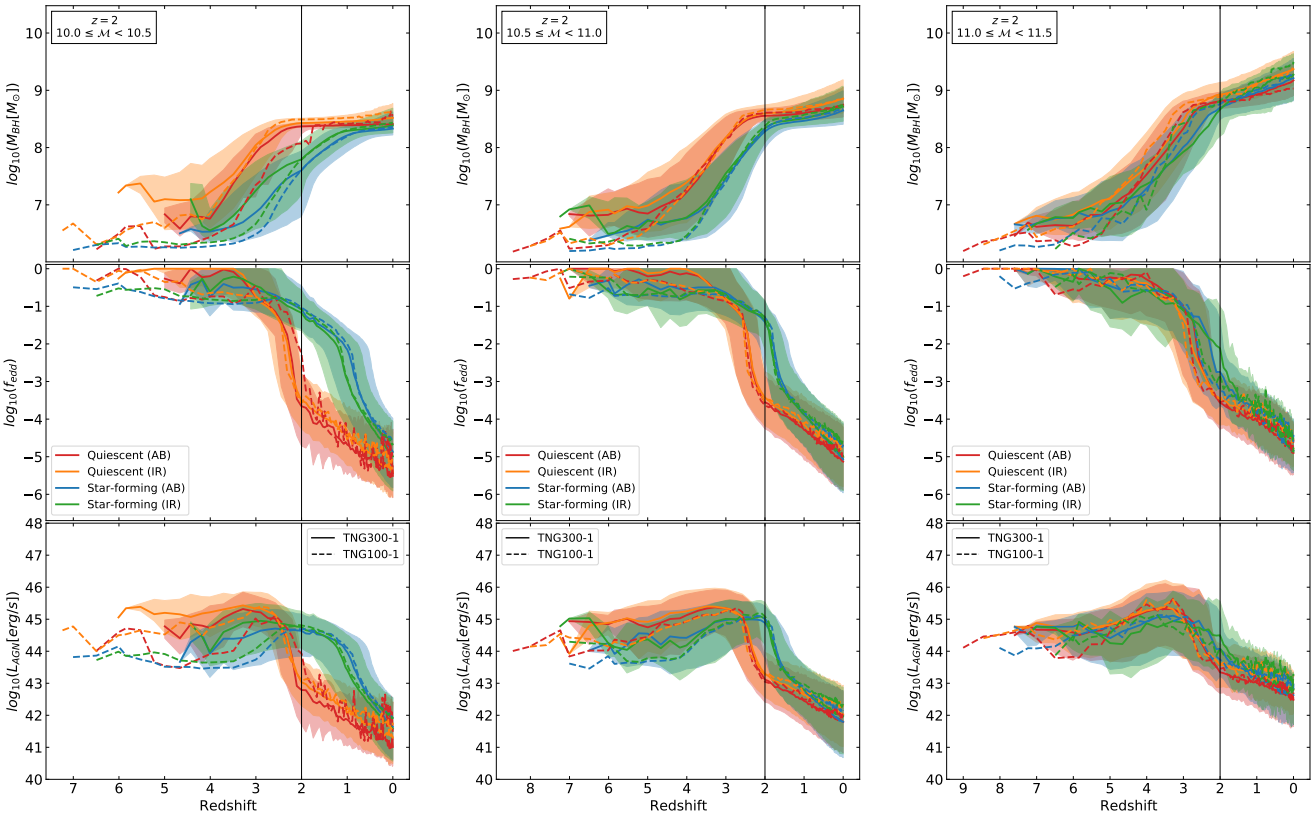


Figure 3.18: Redshift evolution of the black hole mass $M_{BH}$ (top panels), the Eddington ratio $f_{edd}$ (center panels) and the AGN luminosity $L_{AGN}$ (bottom panels). We report these characteristics for TNG300-1 (solid) and TNG100-1 (dashed), quiescent (red and orange) and star-forming (blue and green) at $z = 2$, all-bound and in-radius galaxies. The selected galaxy stellar mass bin is specified in the top panel. For each sub-figure, the median is shown by a solid evolving line and the $16^{th}/86^{th}$ percentile range by a colored area. The solid vertical black line marks the redshift at which these galaxies are quiescent or star-forming.

As of now, we will be testing the hypothesis that the quenching of star-formation of high-z massive galaxies is caused by the AGN feedback. For every galaxy at each redshift, the most massive black hole particle within twice the $SHMR$ was treated as the central supermassive black hole. From this black hole was first extracted its mass $M_{BH}$, its instantaneous accretion rate $\dot{M}$ and its Eddington accretion rate $\dot{M}_{Edd}$. We then calculated, as in Hirschmann et al., 2014, the Eddington ratio $f_{Edd} = \dot{M}/\dot{M}_{Edd}$ and the associated AGN (Active Galactic Nuclei)

luminosity $L_{AGN} = \varepsilon_r \dot{M} c^2$ with $\varepsilon_r = 0.2$. We also did not include AGN luminosities below $10^{40}$erg/s for median and percentile estimations.

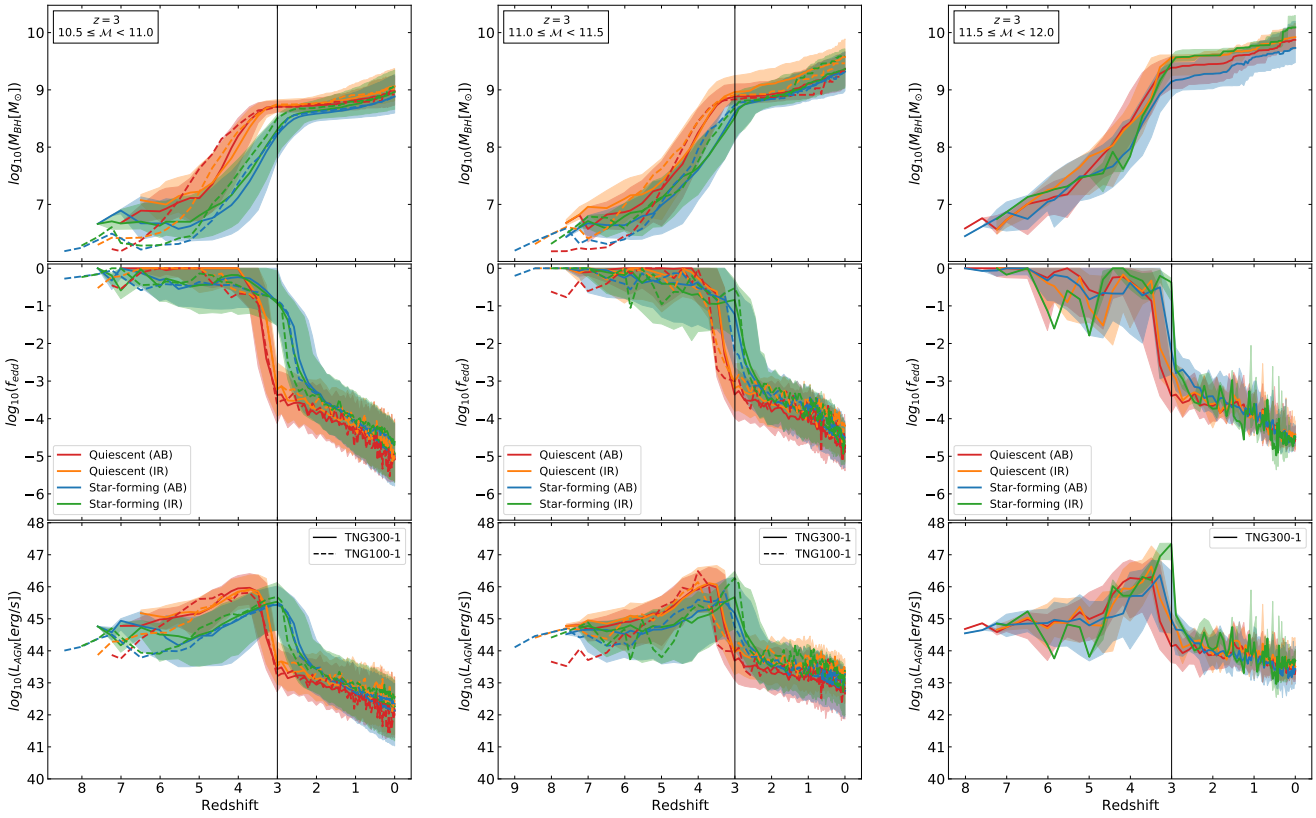


Figure 3.19: Redshift evolution of the black hole mass $M_{BH}$ (top panels), the Eddington ratio $f_{edd}$ (center panels) and the AGN luminosity $L_{AGN}$ (bottom panels). We report these characteristics for TNG300-1 (solid) and TNG100-1 (dashed), quiescent (red and orange) and star-forming (blue and green) at $z = 3$, all-bound and in-radius galaxies. The selected galaxy stellar mass bin is specified in the top panel. For each sub-figure, the median is shown by a solid evolving line and the $16^{th}/86^{th}$ percentile range by a colored area. The solid vertical black line marks the redshift at which these galaxies are quiescent or star-forming.

The growth of the black hole mass the progenitors and descendants of QGs, at high-$z$, has two stages. The first stage is a rapid rise followed by a second weaker/slower growth stage with $z = 2$ and $z = 3$ as the decisive redshifts (Figure 3.18; Figure 3.19). For the progenitors of quiescent galaxies, the $f_{edd}$ falls by almost 4 dex from $f_{edd} \approx 1$ at $z = 4 - 3.5$ for $z = 3$ and $z = 2$. The drop of the Eddington ratio of star-forming galaxies is shifted to higher redshifts as the galaxy stellar mass bin is greater. To summarise, for the progenitors of MQGs at high-$z$, the black hole mass grows much faster, the black hole accretion rates $f_{edd}$ are much higher and the AGN luminosity peaks at earlier times than for the progenitors of massive SFGs at high-$z$. This means that MQGs at high-$z$ have been exposed to higher levels of AGN feedback for a longer period of time. This trend is a bit less pronounced for galaxies in the highest mass bin, but this may be linked to lower statistics for MQGs, in particular at z=3.

The median value of the $f_{edd}$ of the star-forming progenitors of $z = 2$ and $z = 3$ QGs are superior to those of $z = 2$ and $z = 3$ SFGs. Black holes accreting at Eddington levels at

very high-$z$ appear to play important role in the star-formation quenching. The quiescent luminosity peaks at $\log(L_{AGN}) = 46 \pm 0.5$ at $z = 3$ ($z = 4$) for $z = 2$ ($z = 3$) immediately before declining by $\geqslant$ 2dex within a period of redshift.

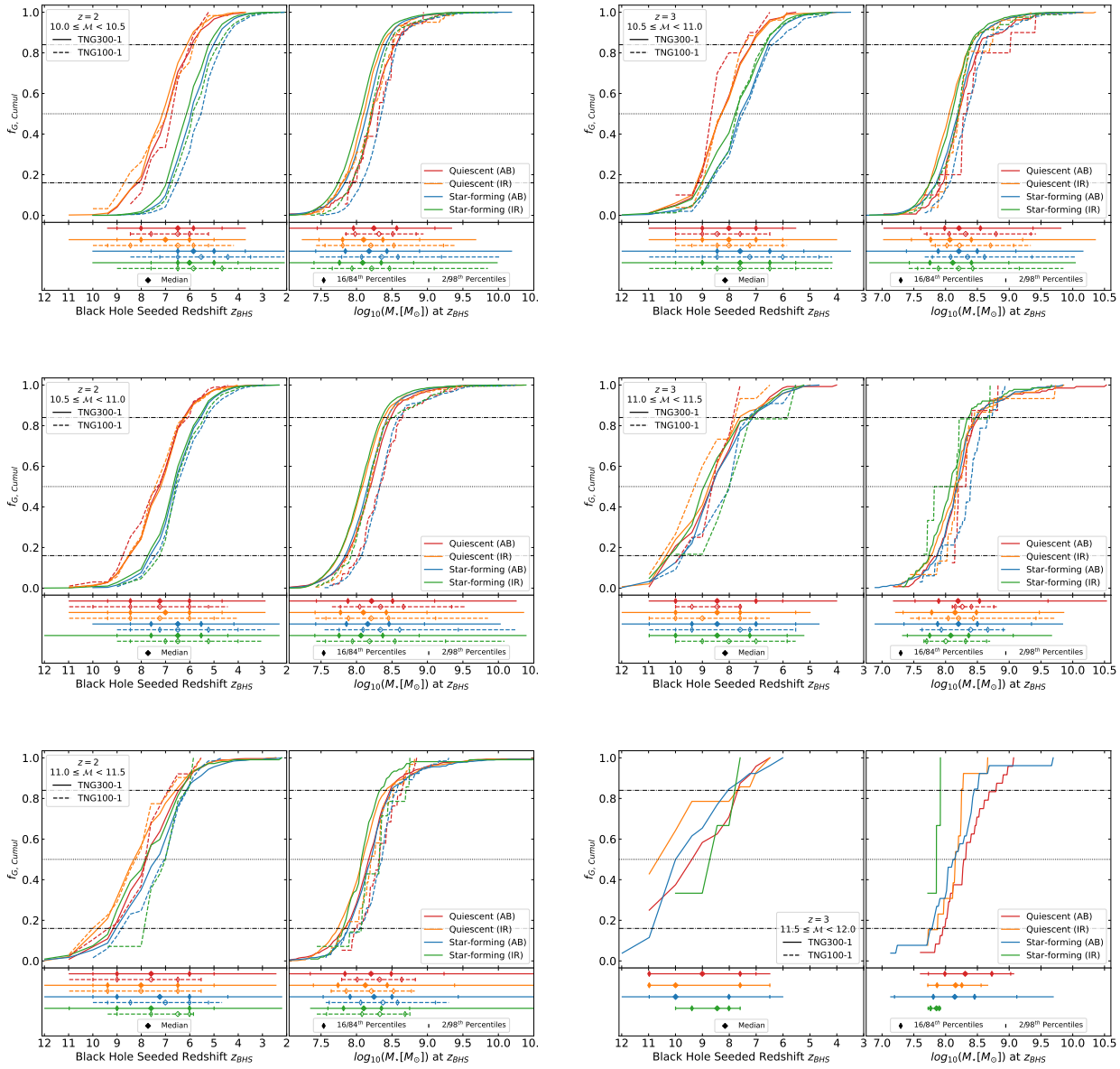


Figure 3.20: Cumulative relative fraction of galaxies with a given black hole seeded redshift ($z_{BHS}$) (left sub-panels) and with a given galaxy stellar mass at $z_{BHS}$ (right sub-panels). We report these fraction for TNG300-1 (solid) and TNG100-1 (dashed), quiescent (red and orange) and star-forming (blue and green) at $z = 2$ (left panels) and $z = 3$ (right panels), all-bound and in-radius galaxies. The selected galaxy stellar mass bin is specified in the left sub-panels.

Secondly, we study the redshift $z_{BHS}$ at which the black hole is seeded in a progenitor galaxy and the galaxy stellar mass at $z_{BHS}$ (Figure 3.20). We look for the highest redshift at which black holes are seeded into their host galaxy. As a reminder, a central black hole with $M_{BH} = 1.18 \times 10^6 M_\odot$ is seeded within a halo once the halo reaches a mass of $7.38 \times 10^{10} M_\odot$. We find that progenitors of MQGs have their central supermassive black hole seeded at earlier times than those of SFGs. Indeed, we find, for example, that the supermassive black holes of the progenitors of $10 < \mathcal{M} < 11$ MQGs at $z = 2$ are seeded at $7.2 - 6.5$ (referring to median)

while the supermassive black holes of the progenitors of $10 < \mathcal{M} < 11$ SFGs at $z = 2$ are seeded at $6.5 - 5.5$ (referring to median). There also seems to be a slight increasing trend

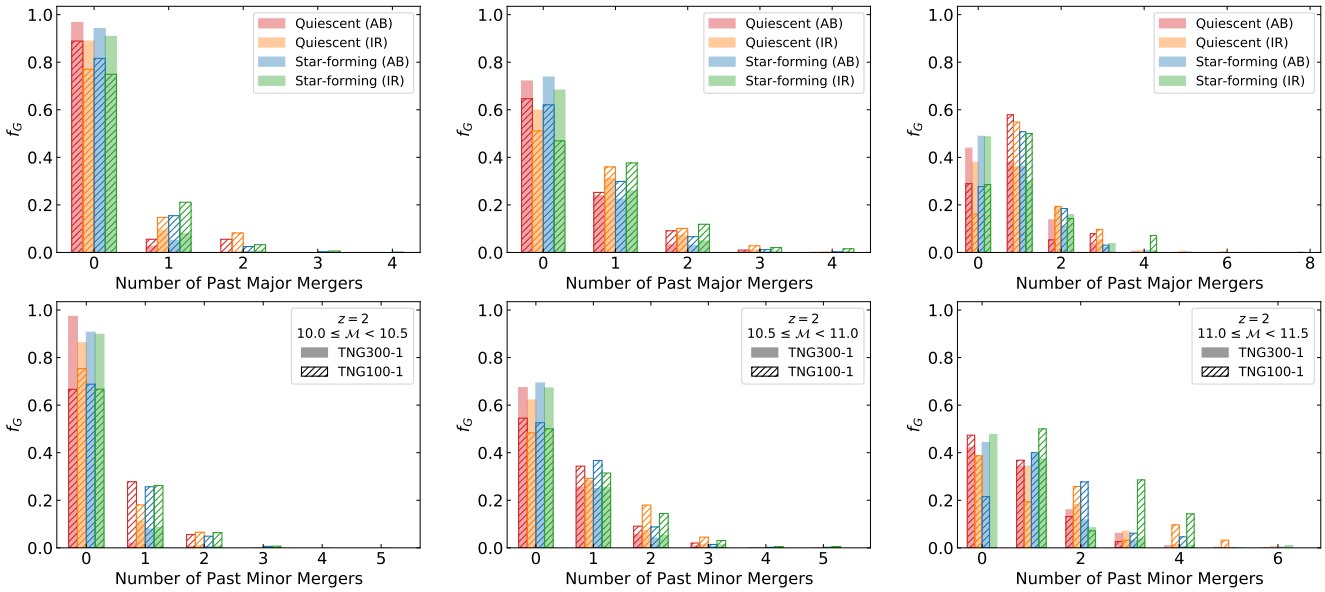


Figure 3.21: Relative fraction of galaxies resulting from a specific number of major (top panels) and minor (bottom panels) mergers. We report these fraction for TNG300-1 (full) and TNG100-1 (hatched), quiescent (red and orange) and star-forming (blue and green) at $z = 2$, all-bound and in-radius galaxies. The selected galaxy stellar mass bin is specified in the bottom panels.

for the median values of $z_{BHS}$ as the galaxy mass bin increases: from $z_{BHS} = 7 - 6.5$ for the progenitors of $10 < \mathcal{M} < 10.5$ MQGs at $z = 2$ to $z_{BHS} = 7.2 - 7$ for the progenitors of $10.5 < \mathcal{M} < 11$ MQGs at $z = 2$ and from $z_{BHS} = 6 - 5.5$ for the progenitors of $10 < \mathcal{M} < 10.5$ massive SFGs at $z = 2$ to $z_{BHS} = 6.5$ for the progenitors of $10.5 < \mathcal{M} < 11$ massive SFGs at $z = 2$. This remains a vague trend since the $16^{th}/86^{th}$ percentile range of $z_{BHS}$ for the progenitors of both QG and SFG populations, overlap considerably. This implies that the progenitors of $z = 2/3$ QGs reside earlier and in more massive halos than those of $z = 2/3$ SFGs since black holes are seeded once a specific halo mass is reached. This presupposes that the progenitors of MQGs at high-$z$ are exposed to black hole feedback for longer periods of time. This is likely to contribute to an earlier quenching of the progenitors of MQGs relative to those of massive SFGs. At $z_{BHS}$, the galaxy stellar mass of the progenitors of $z = 3$ and $z = 2$ SFGs and QGs are almost identical. It appears that, with larger galaxy stellar mass bins, the gap between values of $z_{BHS}$ associated to MQGs and to massive SFGs at high-$z$ is reduced. We understand this to be a statistical issue, as we have less highly massive galaxies than lower massive galaxies.

### 3.3.3 Role of Major and Minor Merger Events

In published literature (Belli et al., 2019; Girelli et al., 2019; Sherman et al., 2020;), galaxy mergers have frequently been brought forward as substantial candidates for the quenching of galaxies. This makes the research of galaxy mergers, both major and minor, particularly compelling for the study of the origin of MQGs at high-$z$. With this in mind, we studied quiescent and star-forming galaxies' past merging history. We categorised $1:1-1:4$ mergers as major mergers and $1:4-1:10$ mergers as minor mergers. We counted all the mergers

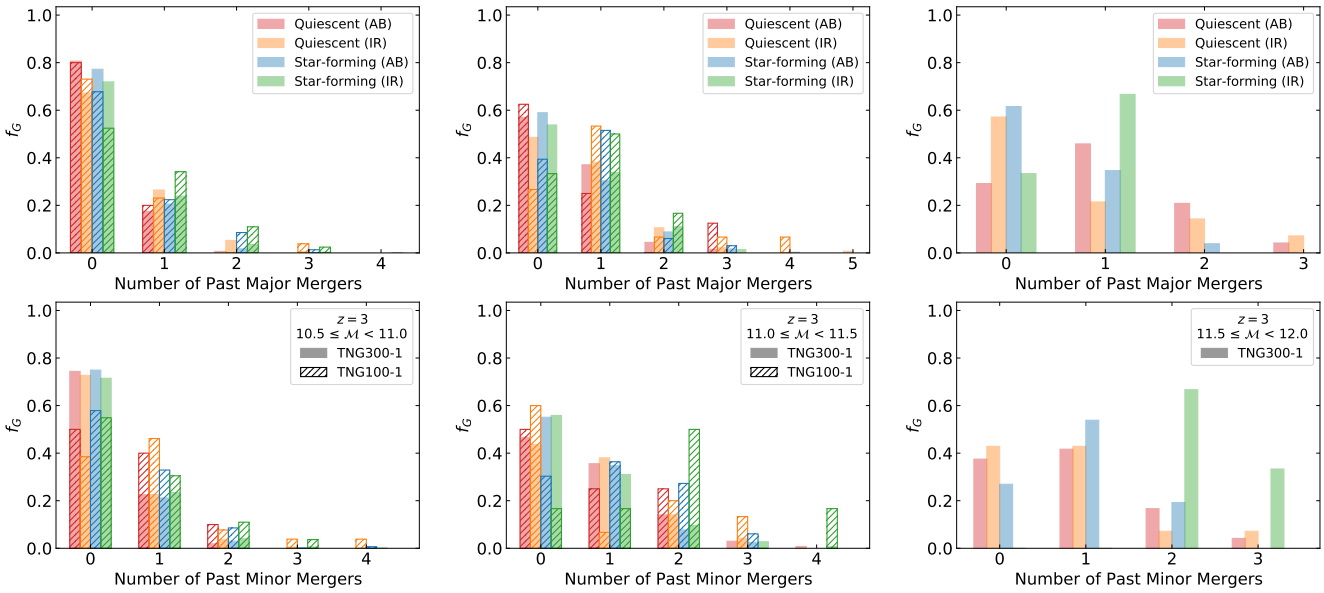


Figure 3.22: Relative fraction of galaxies resulting from a specific number of major (top panels) and minor (bottom panels) mergers. We report these fraction for TNG300-1 (full) and TNG100-1 (hatched), quiescent (red and orange) and star-forming (blue and green) at $z = 3$, all-bound and in-radius galaxies. The selected galaxy stellar mass bin is specified in the bottom panels.

occurring between the first progenitor to be beyond the galaxy stellar mass threshold and the redshift of the selection. We did not aim to account for galaxies that would oscillate around the mass threshold due to mergers and galaxy harassment although it is a possibility.

With increasing galaxy stellar mass bin, the number of galaxies having not been the product of a single major or minor merger decreases causing the number of galaxies with 1 and 2 recorded past mergers to increase (Figure 3.21; Figure 3.22). There seems to be no clear indication that MQGs have more or less past major or minor mergers than massive SFGs. Indeed, the relative fractions, across categories, are close to identical. Therefore, it is likely that galaxy mergers do not have a relevant role in the quenching process of MQGs at $z = 2/3$. They are definitely not necessary in the case of MQGs at $z = 2/3$.

## 3.4 Rejuvenation of Massive Quiescent Galaxies After z=2/3

Finally, IllustrisTNG subhalo merger trees also provide an opportunity to study the descendants of high-redshift massive quiescent galaxies such as their relative star-forming fraction $f_{SFG}$.

Ichikawa et al., 2017 has speculated on the possible star-formation rejuvenation of the passive galaxy population. Star-formation rejuvenation is to be understood as a sudden starburst leading a previously quiescent galaxy to become star-forming once again. Ichikawa et al., 2017 mentions minor mergers as possible events triggering star-formation rejuvenation. This study expects half of its recently QGs to have rejuvenated at $z > 1.5$. Interestingly, IllustrisTNG appears to predict such events (Figure 3.23). In fact, after $z = 3$ and $z = 2$, the $f_{SFG}$ of quiescent descendants rises to a high of about $5 - 35\%$ before vanishing shortly before $z = 0$. The greater the mass bin the greater the fraction of rejuvenated galaxies. It is the same for higher redshift total quenching leading to a more significant peak. TNG100-1 produces higher rejuvenation levels than TNG300-1. We did not linger on the individual

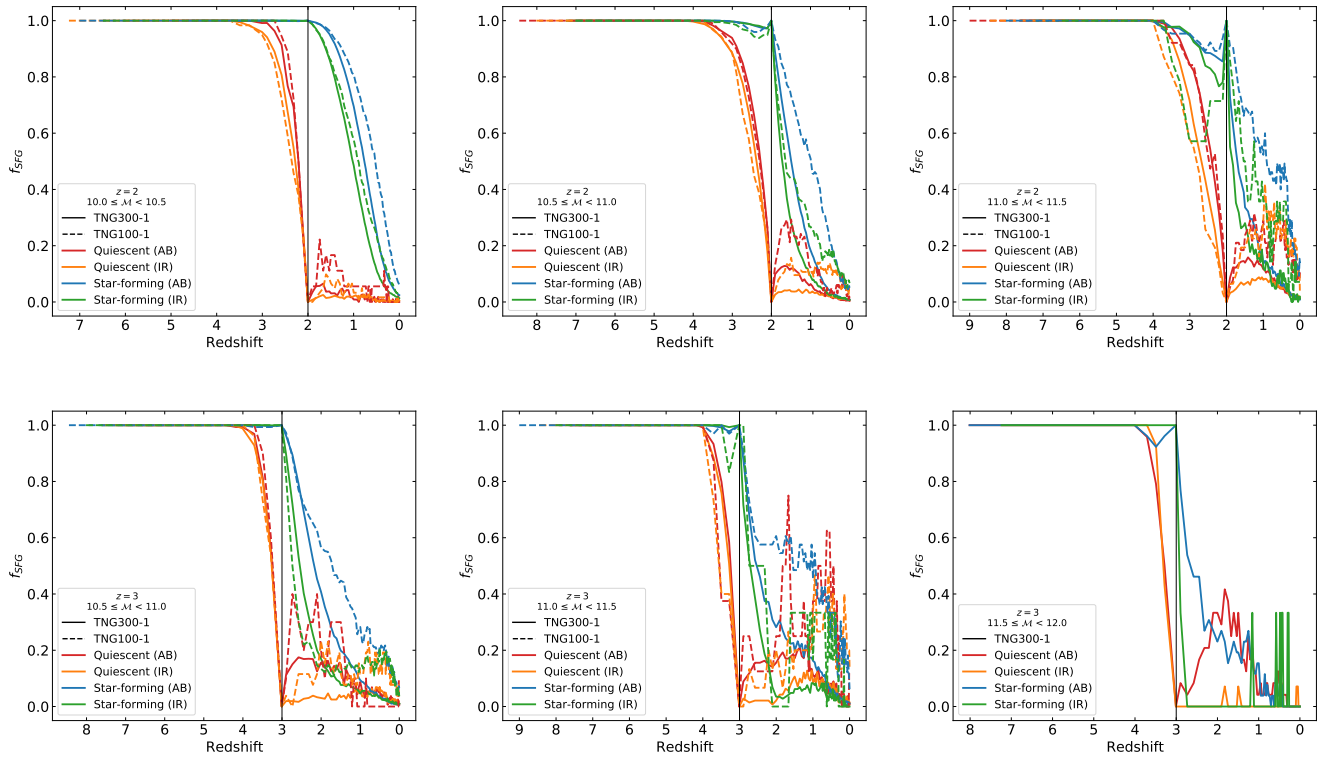


Figure 3.23: Redshift evolution of the relative star-forming fraction ($f_{SFG}$). We report TNG300-1 (solid) and TNG100-1 (dashed), quiescent (red and orange) and star-forming (blue and green) at $z = 2$ (top panels) and $z = 3$ (bottom panels), all-bound and in-radius galaxies. The selected galaxy stellar mass bin is specified in each panel. The solid vertical black line marks the redshift at which these galaxies are quiescent or star-forming.

galaxy rejuvenation level but we simply looked to check whether the galaxy's $sSFR$ surpasses the $sSFR_c$. It would be interesting to further understand the reasons behind some MQGs rejuvenating. This, however, goes beyond the scope of this thesis.

# Chapter 4

# Discussion

In this section, we will discuss our results while putting them into context. We will begin our discussion with the two (or five) galaxy definitions that we used in this work (see section 4.1). Then we will address the two criteria defining quiescence in IllustrisTNG galaxies, in section 4.2. Thirdly, in section 4.3, we will review the mass-size, mass-velocity dispersion and size-velocity dispersion relations. Afterwards, we will treat, in section 4.4, the origin of IllustrisTNG's massive quiescent galaxies at high-$z$. In the last two subsections, we will mention the various caveats we identified to explain the discrepancies between our IllustrisTNG results and observations. We will first look, in section 4.5, at those arising from IllustrisTNG and then those originating from observations (section 4.6).

## 4.1 Different Definitions for Galaxies

To start off, in order to compile this report, we tested two distinct galaxy definitions: an all-bound (AB) galaxy definition and an in-radius (IR) galaxy definition (see section 2.4). From the start, we expected the IR galaxy definition to provide better agreement between properties of observed galaxies and the properties of IllustrisTNG galaxies than AB galaxy definition. These expectations were based on the fact that IR galaxy definition describes galaxies in a way which is closer to the one adopted by observations.

What is more, these expectations were confirmed for all of the global and quiescent galaxy stellar mass functions especially at their high mass ends. By definition AB galaxies have greater galaxy stellar masses than IR galaxies. This explains the differences we see at the high mass end between AB galaxies, IR galaxies and observed galaxies. However, these expectations were also refuted when properties of AB galaxies were more aligned with observations than were the properties of IR galaxies. Such properties were: the fraction of quiescent galaxies at $z = 2$ and $z = 3$ (Figure 3.9), the stellar half mass radius of MQGs at redshift 0 (Figure 3.11) and the velocity dispersion of MQGs at high redshift (Figure 3.13).

We tested and found that the quiescent classification of galaxy is highly impacted by the galaxy aperture definition. Indeed as was highlighted in Donnari et al., 2019, the smaller the galaxy aperture the more IllustrisTNG galaxies categorised as quiescent. As a matter of fact, the existence of galaxies that are both quiescent under the IR galaxy definition as well as star-forming under the AB galaxy definition suggests some star-formation taking place in the outer ($> 2 \times SHMR$) region of galaxies. Interestingly, the idea that observed galaxies have been wrongly classified as quiescent galaxies, due to undetected star formation happening in the outer regions, has been presented in Merlin et al., 2019. In addition to star formation occurring outside of the central region, the ring-like structure of the star forming clouds (Figure 3.7, Figure A.2 and Figure A.1) supports the idea of an inside-out quenching or a heating of the central gas due to black hole feedback. Therefore the choice of the galaxy definition is paramount when studying quiescent galaxies.

## 4.2 Different Criteria for Quiescence

First of all, we checked the impact of the choice of criteria for quiescence on IllustrisTNG galaxies by using two different criteria: one $0.3/t_H$ and one $MS-1$ (see subsection 3.2.1). As was revealed by Figure 3.4, the $0.3/t_H$ selection is appropriate for galaxies at high-$z$ ($z > 1.5$) and below the $MS-1$ until $z > 0.75$. However, the $MS-1$ criterion should be considered a better option for low-$z$ galaxies.

These criteria are put into context by the main star-forming sequence from Speagle et al., 2014, which is a compilation of 25 studies of the $MSFS$ at $0 < z < 6$. In fact, these criteria allow for the infiltration, within the quiescent galaxy population, of super massive SFGs at $z < 0.75$. This leads to a degradation in the purity of our IllustrisTNG MQG sample at low redshift and even more so for the sample defined according to the $0.3/t_H$ criterion. The presence of SFG infiltrators in the IllustrisTNG MQG sample has negative affects on the properties of IllustrisTNG MQGs by distancing them from the observed MQG properties at low-$z$. Since our study relates to MQGs at high-$z$, this only truly affects our results of the future ($z < 3$ or $z < 2$) star-formation rejuvenation of MQGs at high redshift.

In order to improve the quiescent criteria and limit the effects mentioned above, we could, in future studies, create a new criteria for quiescence by combining the $0.3/t_H$ selection and the upper $sSFR$ limit provided by Fumagalli et al., 2014. It is worth mentioning that Donnari et al., 2019 obtained extremely similar quiescent fractions between the IllustrisTNG $UVJ$ and a linearly extrapolated $MS-1$ criteria. This goes to show that the two selections, although obtained differently, lead to a substantial overlap of their quiescent galaxy population. It was also the case, in our study, for quiescent galaxy fractions with differences in fractions primarily due to the choice of galaxy definition rather than that of the definition for quiescence. To conclude, the choice of galaxy definition is to be taken more seriously than the choice of definition for quiescence as differences arise predominately from the former.

## 4.3 Origin of Mass-Size and Mass-Velocity Dispersion Relation

We would like to focus on the possible origin of the stellar mass-size and stellar mass-velocity-dispersion relations arising in IllustrisTNG and often found in published literature (Newman et al., 2010; Belli et al., 2014; van der Wel et al., 2014; Belli et al., 2017; Mosleh et al., 2017; Tanaka et al., 2019; Mendel et al., 2020; Stockmann et al., 2020; Esdaile et al., 2021).

For low mass star-forming galaxies, galaxy size growth is monopolised by star-formation while for high mass quiescent galaxies, growth is due to mergers (van Dokkum et al., 2015). In Figure 3.21 and Figure 3.22, at $z > 2/3$, we already observed this size growth tendency for high-mass QGs. Indeed, at $z = 2/3$, more massive galaxies have been subjected to merging than it is the case for lower mass galaxies. This should explain the two phases of the stellar mass evolution of $SHMR$ seen in Figure 3.11 at $z < 2$. At $z = 3.5$ or $z = 3$, IllustrisTNG returns a rather flat relation which could be explained by quiescent galaxies having quenched very recently and no more frequent mergers than for star-forming galaxies. At $z = 2$, the median $SHMR$ of SFGs still remains greater than the median $SHMR$ of QGs. This insinuates that, although the two-phased $SHMR$ curves are now apparent, with mergers becoming more frequent, star formation is still the dominant $SHMR$ growth channel. With decreasing redshift, the $SHMR$ gap starts to close between MQGs and SFGs (Figure 3.12). In other words, MQGs grow into galaxy sizes more similar to SFG sizes as cosmic time unfolds. This can be explained by mergers becoming more frequent due the formation of large cosmological structures connecting halos together, also known as halo merging, at low-$z$. Large SFGs also join the QG population as they witness the quenching of their star-formation.

As highlighted in Savorgnan et al., 2016, there is less scatter for QGs (early-type galaxies) than for SFGs (late-type galaxies) in the $M_{BH}$-$M_{sph,\star}$ relation with $M_{sph,\star}$ the host spheroidal

stellar mass. This implies that, for QGs, their central supermassive black hole evolves with their spheroidal stellar mass in a way which is more common between each individual QG than it is between each individual SFG (Schneider, 2015). The $\sigma_e$ has also been shown to correlate with the black hole mass (Schneider, 2015). This supports the case for a close evolution between the central supermassive black hole and a galaxy's rotating spheroidal stellar component. All of this explains the likely origin of the stellar mass-$\sigma_e$ relation we observe.

As said earlier, the velocity dispersion used here is a one dimensional velocity dispersion of all particle and cell members of a given galaxy. All observations are two dimensional stellar velocity dispersion. This represents one caveat for comparison with observed $\sigma_e$. The other caveat relates to our use of $SHMR$ as a galaxy size (up to half of half-light radius (Mosleh et al., 2017). This likely explains some of the inconsistencies with observations.

## 4.4 Origin of Massive Quiescent Galaxies at High-Redshift

In addition to star formation occurring outside of the central region, the ring-like structure of the star forming clouds (Figure 3.7, Figure A.2 and Figure A.1) supports the idea of an inside-out quenching or a heating of the central gas due to black hole feedback. This is coherent with the stellar mass behaviour of QGs. Indeed, it has been observed that QGs become less and less compact with cosmic time as well as experience an expulsion of the central star formation towards the outer regions already at $z < 2.5$.

For quiescent $GSMF$s, recently quenched galaxies appear to be less massive with time. As presented in Peng et al., 2010, this is possibly due to galaxy migration towards the center of galaxy clusters. If the increase in galaxy stellar mass achieved through central star formation fueled by accreting cold gas from outside the galaxy (Sherman et al., 2020) is a significant mass growth channel and that the halo gas reservoir has already been depleted by already present galaxies, the galaxy migration will be highly efficient.

To summarise, for the progenitors of MQGs at high-$z$, the black hole mass grows much faster, the black hole accretion rates $f_{edd}$ are much higher and the AGN luminosity peaks at earlier times than for the progenitors of massive SFGs at high-$z$. This means that MQGs at high-$z$ have been exposed to higher levels of AGN feedback for a longer period of time. This trend is a bit less pronounced for galaxies in the highest mass bin, but this may be linked to lower statistics for MQGs, in particular at z=3.

Other than a drop in the fraction of galaxies $f_G$ with no past mergers and a rise of $f_G$ for those with at least one, there appears to be no obvious difference between the past merging history of high-$z$ quiescent and star-forming galaxies. Therefore, quenching in galaxies is not strikingly due to past major or minor mergers. TNG300-1 is more apt to larger $f_G$ with at least one past minor or major merger. SIMBA simulation also predicts that major mergers are not linked to quenching but do lead to starbursts (Weinberger et al., 2018; Rodríguez Montero et al., 2019).

The drop in black hole activity after an almost maximal accretion rate and little black hole mass increase may imply a lack of cold gas within a galaxy, an emptied halo gas reservoir (Moustakas et al., 2013), the dissipation of intergalactic filaments providing cold gas from the IGM (Sherman et al., 2020) or a stable gas disk (Martig et al., 2009) or ionised gas disk (van Dokkum et al., 2015). Future studies using the IllustrisTNG simulation could and should be directed in these fields by determining the redshift evolution cold gas fractions inside galaxies and in the parent halo. However as suggested in Schreiber et al., 2018, quiescent galaxies could still harbor significant amounts of gas reservoir. This would support the case for stable non-star-forming gas disk or the heating of the remaining gas via past thermal black hole feedback (Girelli et al., 2019). Since quenching progenitors of $z = 3/2$ quiescent galaxies witness a diminishing black hole accretion activity, the black hole-driven kinetic winds could

likely expel gas beyond the outer regions and outside of galaxies themselves (Girelli et al., 2019). Valentino et al., 2020 found that TNG300 did not predict all sub-millimeter galaxies to be progenitors of $z = 4 - 3$ quiescent galaxies. Weinberger et al., 2018 revealed that the quenching of IllustrisTNG $z = 0$ quiescent galaxies was associated to kinetic mode feedback from low black hole accretion. This also appears to be the case for IllustrisTNG $z = 3$ and $z = 2$ quiescent galaxies.

## 4.5 Caveats of IllustrisTNG Simulation

At high-$z$, of simulation limitations, we are unable to conclude with certainty on the mechanisms and processes causing quenching. We have found three caveats for the IllustrisTNG Simulation:

1. AB-defined galaxies better agree with observations than IR-defined galaxies for the fraction of quiescent galaxies at $z = 2$ and $z = 3$ (Figure 3.9), the stellar half mass radius of MQGs at redshift 0 (Figure 3.11) and the velocity dispersion of MQGs at high redshift (Figure 3.13);

2. At $z = 2 - 3$, the main star-forming sequence, resulting from our $0.3/t_H$ criterion for quiescence, was underestimated (outside of $16/84^{th}$ percentile ranges) with regards to the $MSFS$ from Speagle et al., 2014 (a compilation of 25 studies of $MSFS$). This underestimation of the $MSFS$ was also found to hold at $0.75 < z < 2.0$ (Donnari et al., 2019). The stellar feedback model requires improvements;

3. There seems to be an over estimation of $\mathcal{M} \geqslant 11$ MQGs at $z = 2$ (and to some degree at $z = 3$). This overestimation is regardless of the quiescent criteria;

## 4.6 Caveats of Observational Data

The reason for detailing the methods chosen in the papers we used is that IllustrisTNG allows for an intrinsic and instantaneous access to galaxy properties. It is not the case for galaxies in the observable universe as properties are inferred from galaxy spectra.

### 4.6.1 Observational Estimates of $SFR$

Spectral Energy Distribution (SED) fits using LePhare code (Arnouts et al., 2002; Ilbert et al., 2006) have been combined with several SFHs to witness the impact each SFH has on its associated $SFR$ estimates. As such, exponentially declining and delayed $\tau$ declining SFHs (Tasca et al., 2015; Davidzon et al., 2017) along with exponentially rising, power law rising, linearly rising and superimposition of a top hat and an exponentially declining SFHs (Speagle et al., 2014) for fixed redshifts were selected in the observations mentioned in the figures. Inputting spectroscopic redshifts lessens degeneracy (Tasca et al., 2015). $SFR$s have also been infered with $SFR_{IR} = 0.98 \times 10^{-10} L_{IR}$ (Bell et al., 2005) after extrapolating the total IR luminosity from observed $24\mu m$ flux using Bolzonella et al., 2000's HYPERZ program (as well as UV emission in addition to the IR for Damen et al., 2011) or source fitting algorithms, as presented in Labbé et al., 2005 and Wuyts et al., 2007 (Fumagalli et al., 2014). Brammer et al., 2008's EAZY (Sherman et al., 2020), Kriek et al., 2009's FAST and its C++ implementation FAST++ (Schreiber et al., 2018) have also been used to track $SFR$s (Whitaker et al., 2010; Barro et al., 2016 and Schreiber et al., 2018; Esdaile et al., 2021 respectively) while keeping in mind $H_\beta$ and $[OII]$ emission lines to determine $SFR$ upper limits (Valentino et al., 2020). iSEDfit, a Bayesian SED modeling code, linked to an Chabrier, 2003 IMF was employed in Moustakas et al., 2013 to evaluate the $SFR$s. The width of the $H_\alpha$ emission line gave an overview of the ongoing $SFR$s (Kriek et al., 2006). A further method for obtaining $SFR$s

is with Tanaka2015 photometric redshift code (Tanaka et al., 2019). Finally, the Bruzual A. et al., 1993's GISSEL 2000 SED fitting code was chosen to retrieve $SFR$s (Fontana et al., 2009).

### 4.6.2 Observational Estimates of Galaxy Sizes

The two dimensional surface brightness fitting algorithm GALFIT (Peng et al., 2002; Belli et al., 2017; Stockmann et al., 2020) and its $3^{rd}$ version (Peng et al., 2010; van der Wel et al., 2014; Mosleh et al., 2017; Mendel et al., 2020, Esdaile et al., 2021) were employed in the measurement of a majority of the half-light radii $HLR$.

GALFIT has been used to obtain galaxy half-light radius via flexible Sersic light profiles (van der Wel et al., 2014; Mendel et al., 2020; Stockmann et al., 2020; Esdaile et al., 2021). Belli et al., 2017 has shown major ellipse axis radii or semi-major radii to be more consistent with observations than circularized radii, differing only by a factor of $\sqrt{q}$ with $q$ the axis ratio. Estimated circularized radius has been noticeably smaller than face-on galaxy radius. Mosleh et al., 2017, after having inferred $HLR$s and galaxy stellar mass profiles via SED fits, deduced $SHMR$.

### 4.6.3 Observational Estimates of Stellar Velocity Dispersion

The velocity dispersion from other studies reported in our figures correspond to line of sight stellar velocity dispersion attained with the pPXF algorithm (which stands for Penalized Pixel-Fitting) from Cappellari et al., 2004 (Newman et al., 2010; Belli et al., 2014; Belli et al., 2017; Stockmann et al., 2020) or Cappellari, 2017 (Esdaile et al., 2021) along with the simple stellar population model from Vazdekis et al., 2010 (Tanaka et al., 2019). In Mendel et al., 2020, $\sigma_e$ were obtained through lognormal SFHs and solar metallicity which have unsignificantly biased the estimates. The Gaussian convolution of SFHs has been shown as a technique to provide $\sigma_e$ estimates (Valentino et al., 2020)

### 4.6.4 Observational Criteria for Quiescence Selection

As in Sherman et al., 2020, there have been three major criteria to distinguish between star-forming and quiescent galaxies: a rest-frame color magnitude-based selection, a $MSFS$-based selection and a $sSFR$-based selection. Rest-frame color magnitudes have been obtained through the integration of the best fitted observed SED synthetic spectrum (Belli et al., 2014). Merlin et al., 2018 has argued that spectral synthesis models dictates the quiescent classification of galaxies due to their key role in establishing selection regions in color planes and providing a method to estimate galaxy characteristics such as age, $SFR$, rest-frame color and stellar mass via SED fits.

In terms of rest-frame color magnitude-based selections, the most frequently used one has to be the $U-V$ vs $V-J$ plane ($UVJ$ hereafter). A $UVJ$ limit that has been commonly used (Belli et al., 2014; van der Wel et al., 2014; Martis et al., 2016, Belli et al., 2017; Mosleh et al., 2017; Schreiber et al., 2018), was developed in Williams et al., 2009:

$$\begin{aligned}
&(U-V) > 0.88 \times (V-J) + 0.69, \quad \text{for } z < 0.5 \\
&(U-V) > 0.88 \times (V-J) + 0.59, \quad \text{for } 0.5 < z < 1.0 \\
&(U-V) > 0.88 \times (V-J) + 0.49, \quad \text{for } 1.0 < z < 2.0 \\
&(U-V) > 1.3 \quad \text{and} \quad (V-J) < 1.6, \quad \text{for all z}
\end{aligned}$$

It was defined so as to maximize the $sSFR$ differences between the regions and contamination from unobscured and dusty star-forming galaxies. In Carnall et al., 2018 (referenced by

McLeod et al., 2021), Williams et al., 2009's for-$z < 0.5$ and for-all-z criteria were applied to a redshift range of $0.25 \geqslant z \geqslant 3.75$.

In Whitaker et al., 2011 (assumed by Belli et al., 2014; van der Wel et al., 2014; Belli et al., 2017; Mendel et al., 2020; Esdaile et al., 2021), most of the $UVJ$ limits from Williams et al., 2009 have been reused and $(U-V)$ and $(V-J)$ thresholds changing with redshift were implemented:

$$\begin{aligned}
&(U-V) > 0.88 \times (V-J) + 0.69, \quad \text{for } z < 0.5 \\
&(U-V) > 0.88 \times (V-J) + 0.59, \quad \text{for } z > 0.5 \\
&(U-V) > 1.3 \quad \text{and} \quad (V-J) < 1.6, \quad \text{for } z < 1.5 \\
&(U-V) > 1.3 \quad \text{and} \quad (V-J) < 1.5, \quad \text{for } 1.5 < z < 2.0 \\
&(U-V) > 1.2 \quad \text{and} \quad (V-J) < 1.4, \quad \text{for } 2.0 < z < 3.5
\end{aligned}$$

Other studies (Muzzin et al., 2013; Belli et al., 2017; Sherman et al., 2020; Stockmann et al., 2020) have decided to keep some of Whitaker et al., 2011 UVJ selection limits however with $U-V > 1.3$, $V-J < 1.5$ for all redshifts and $z = 1.0$ being the decisive redshift.

Fumagalli et al., 2014 opted for a $UVJ$ selection mixing those from Williams et al., 2009 and Whitaker et al., 2011 in other words: $U-V > 1.3$, $V-J < 1.5$, $(U-V) > 0.8 \times (V-J) + 0.7$ for all redshifts.

Whitaker et al., 2010, on the other hand, has gone for a quite distinct $UVJ$ selection (Brammer et al., 2009) involving $(U-V)$, dust reddening correction factor $\Delta UV = 0.47 A_V$ ($A_V$ the visual extinction built upon the Calzetti et al., 2000 dust extinction law), the Hubble time $t_H$ and the lookback time $t_{LB}$:

$$(U-V) - \Delta UV - (2.03 - 0.77 \times t_{LB}/t_H) > -0.4$$

The expected time evolving mean linear color is described by the third term. The final results have turned out to be very similar to those provided from a Williams et al., 2009 $UVJ$ selection despite Brammer et al., 2009 being more conservative (Brammer et al., 2009). Merlin et al., 2018 has found $UVJ$ diagrams to not be ideal at classifying passive galaxies since galaxies with low levels of dust and sudden quenching SFH have been to detected outside the quiescent zone of the $UVJ$ plane 0.5Gyr after star formation suppression.

Another rest-frame color magnitude-based selection has been put forward in Ilbert et al., 2013 and made use of $NUV - r^+$ vs $r^+ - J$ plane ($NUVrJ$) with $NUV$ being the 0.23065$\mu$m-centered GALEX filter and $r^+$ a broad band filter centered at 0.62318$\mu$m. Ilbert et al., 2013 has set it in the following way:

$$\begin{aligned}
&(NUV - r) > 3\,(r-J) + 1, \quad \text{for } 0.2 < z < 2.0 \\
&(NUV - r) > 3.1, \quad \text{for } 0.2 < z < 2.0
\end{aligned}$$

These criteria were adopted in Davidzon et al., 2017 and in Ichikawa et al., 2017. Ichikawa et al., 2017 has added a third critical threshold $r - J = 0.5$ for the distinction between recently and long-time quenched galaxies. This selection has taken into account the 0.2Gyr period prior to star-formation quenching if assuming a single burst model (Ichikawa et al., 2017). Under $UVJ$ rest-frame color selections, there has been little distinction between $\log(sSFR) < -11$ and $\log(sSFR) \approx -10$. This is not the case for $NUVrJ$ as it has been shown to be more suitable to past $10^6 - 10^8$yr star formation (Davidzon et al., 2017). In addition, $NUVrJ$ has been found to be more robust at high-$z$ than $NUVrK$ ($NUV - r^+$ vs $r^+ - K$ plane) due to more unknown surrounding the $k$-correction (Davidzon et al., 2017). $NUV - r^+$ versus $r^+ - J$ color-color diagrams have provided a clearer contrast between quiescent and dusty star-forming galaxies than their analogous $U-V/V-J$ as well as minimised the observational

uncertainties as they deal with larger dynamical ranges (Ilbert et al., 2013). Half of the star-forming population, using the latter diagram, was regarded as part of the red galaxy population, and so a quiescent one, but this was due to the reddening effect of high levels of obscuring dust (Muzzin et al., 2013). Recently, $FUV$ color-based criterion have been found, via Bayesian methods, to have an even greater correlation with $sSFR$ compared to $NUV$ color-based selection (Leja et al., 2019).

Further confirmation of the $UVJ$-quiescent nature of observed galaxies was achieved with a $\log(sSFR) < -11$ (Ilbert et al., 2013) or a $sSFR < 0.15\text{Gyr}^{-}1$ (Schreiber et al., 2018) selection. Girelli et al., 2019 used a $sSFR$ criterion $\log(sSFR[\text{yr}^{-}1]) < -10.5$ and two near-IR band selection $JK$ vs $IRAC[3.6]$-$IRAC[4.5]$ and $JK$ vs $IRAC[3.6]$ to define quiescent galaxies. Certain studies preferred a $\log(sSFR) < -11$ selection to characterise quenched galaxies (Domínguez Sánchez et al., 2011; Sherman et al., 2020).

Some quiescent galaxies are classified only using a $\log(SFR) < -0.49 + 0.65\log(M - 10) + 1.07(z - 0.1)$ criterion (Moustakas et al., 2013), a $sSFR < 0.1\text{Gyr}^{-}1$ (Barro et al., 2016) criterion or the $MS - 1$ criterion (Ellison et al., 2015). Yet Fontana et al., 2009 went on to separate red or dead galaxies ($\log(sSFR) < -11$) from quiescent galaxies with $sSFR < 1/t_U(z)$ for which $t_U(z)$ is the age of the universe at a given redshift. Damen et al., 2011 has remained the study with which we share the closest quiescent definition as $sSFR < 1/3t_H$ with $t_H$ the Hubble time. Tanaka et al., 2019 opted for a mixture of a $sSFR$-based and a $MSFS$-based selection by insisting on the $1\sigma$ upper limit of estimated $sSFR$ being below $\log(sSFR) < 9.5$ (Tanaka et al., 2019).

In Santini et al., 2020, galaxies have had to meet the following requirements: $H < 27$, detection significance within $1\sigma$ in K, IR1, IR2 bands, best top hat SFH fit with $SFR = 0$ in the passive phase, high quiescent ($> 30\%$) and low star-forming ($> 5\%$) best-fit solutions to be considered quiescent. While in Kriek et al., 2006, galaxies with emission lines best fitted by evolved stellar population models were categorized as quiescent.

Donnari et al., 2019 obtained similar quiescent fractions between the IllustrisTNG $UVJ$ and a linearly extrapolated $MS - 1$ criteria.

$sSFR$ classification has been found to be stricter than color classification at high-$z$ (Ilbert et al., 2013)

# Chapter 5

# Conclusion

In this report, we were exploring the massive quiescent galaxies at high-$z$ provided by the IllustrisTNG simulation. We started off by analysing the simulation's reproducibility of certain high-$z$ MQG properties such as: galaxy stellar mass, quiescent fraction, $SHMR$, $\sigma_e$ and $\sigma_e - SHMR$ plane.

After this was verified, we went on to studying the origin of the early quenching of massive galaxies at high-$z$ by taking advantage of the assembly histories from subhalo merger trees. This lead us to turning our attention to the redshift evolution of galaxy and black hole of both MQGs and SFGs at $z = 2/3$.

A summary of our results and conclusions are presented below:

1. The GSMF and the $f_{QG}$ of MQGs strongly depend on the galaxy definition criteria rather than on the quiescent selection. When we select an IR galaxy definition then our IllustrisTNG results are in fair agreement. This is partly due to large uncertainties in the observation of properties of MQGs at high-$z$. From GSMF and $f_{QG}$ of MQGs, we find traces of a galaxy downsizing (or anti-hierarchical trend) in galaxy formation which is often discussed in literature;

2. Both galaxy sizes ($SHMR$) and velocity dispersion ($\sigma_e$) of simulated MQGs are in rough agreement with observations. There are cases when $SHMR$ and $\sigma_e$ of simulated MQGs are not in agreement. For example, at $z = 3$, the simulation fails to replicate the previously observed and reported correlation between $SHMR$ and galaxy stellar mass for MQGs. IllustrisTNG is equally unsuccessful at predicting the large scatter shown by observations relating to the $\sigma_e$-$M$ plane.

3. When looking at the past evolution of MQGs and massive SFGs, we detect a difference in the starting redshift for the rapid mass increase of their central black hole (as well as for their galaxy stellar mass). For MQGs at $z = 2$ ($z = 3$) it starts earlier, at $z \sim 5$ ($z \sim 6$), than it does for their analogue SFGs;

4. At fixed galaxy stellar mass, SFGs are characterised by lower ($\sim 0.2 - 0.3$) Eddington ratios at higher redshift while MQGs maintain a near 1 Eddington ratio until $z = 3 - 4$;

5. Importantly, we note that the Eddington ratios of progenitors of MQGs at high-$z$ are higher than those of SFGs for a given stellar mass. This implies that their central black hole typically grows faster than the SFGs' central black hole releasing more energy and resulting in highly efficient feedback;

6. Both MQGs and SFGs present near identical relative fractions of galaxies having experienced 0 or 1 major or minor mergers. Therefore, there is no clear indication that past, major or minor, mergers impact the $sSFR$ of galaxies;

7. The central black hole of MQGs is seeded at higher redshift than it is for SFGs'. For example, for $10 < \mathcal{M} < 11$ galaxies at $z = 2$, seeding occurs at $6.5 < z < 7.2$ for the

progenitors of MQGs while it does so at $5.5 < z < 6.5$ for the progenitors of their analogue SFGs. At both of these times, the progenitors of these MQGs and SFGs have almost identical stellar masses ($8.0 < \mathcal{M} < 8.5$). The earlier seeding of faster growing black holes in the progenitors of MQGs at high-$z$ means that these progenitors have been exposed to black hole feedback for a longer period of time (and residing in massive halos at earlier times);

8. Finally, we find that MQGs at $z = 2/3$ experience, at later times ($z < 3 - 2$), star-formation rejuvenation. As a matter of fact, there is a clear rise of 0.2 in their $1 < z < 3$ (for those at $z = 3$) and $1 < z < 2$ (for those at $z = 2$)-descendants' relative star-forming galaxy fraction. For SFGs, their $z = 3 - 4$-progenitors have the lowest past relative star-forming fraction at $0.8 - 0.9$. This fraction will then be 1 at $z = 2/3$ before slowly decreasing until $z = 0$. Due to the chosen $0.3/t_H$ criterion for quiescence definition, the fraction of rejuvenated MQGs may be overestimated at $z < 0.75$;

This study has not been able to sufficiently quantify central supermassive black holes and its feedback as the origin of MQGs at high-$z$ although it does suggest that they are.

In the future, this could be further established by obtaining fractions of galaxies at very high redshift ($z > 6$) with highly accreting supermassive black holes whose descendants are MQGs at $z = 2/3$. Additionally, in order to be able to properly confirm the role of black holes in the quenching of star-formation in massive galaxies at high-$z$, zoom-in cosmological simulations would be a preferable option. Zoom-in are less computationally expensive in the switching on and off of black hole feedback. In addition, it would be worthwhile looking at the past assembly history all of IllustrisTNG MQGs at $z = 2/3$ and not only, as done in our research, those belonging to main progenitor branches of $z = 0$ IllustrisTNG galaxies. Using our MQG sample and studying the redshift evolution of the cold gas fractions (the cold gas mass relative to the stellar and cold gas masses) of MQGs at $z = 2/3$ could help understand the inflow, the consumption and the expelling of cold gas. This is relevant as cold gas represents the basis of star formation. On the one hand, if we were to find that the redshift evolution of the cold gas fraction of MQGs at $z = 2/3$ was different, prior to $z = 2/3$, to that of SFGs then we could assume quenching to originate from the internal depletion of the galaxy cold gas. On the other hand, if these redshift evolution of cold gas fraction were to be close to identical then we would have to further investigate the gas reservoir inside the parent halo. This might allow for a conclusion that quenching is, perhaps, due to halo reservoir cold gas depletion in the IllustrisTNG universe. When dealing with IllustrisTNG MQGs at high-$z$, the study of their emission lines retracing their quenching mechanisms could help the diagnosis of galaxies subjected to quiescence and detected by the JWST/NIRSpec instrument in the observable universe.

This study was made possible using the multi-processing powers of Copenhagen University's HPC (High Performance Computing) system attributed to the DARK research team. In addition, we used Copenhagen University's ERDA (Electronic Research Data Archive) to store our results.

# Appendix A

# Impact of Galaxy Definition

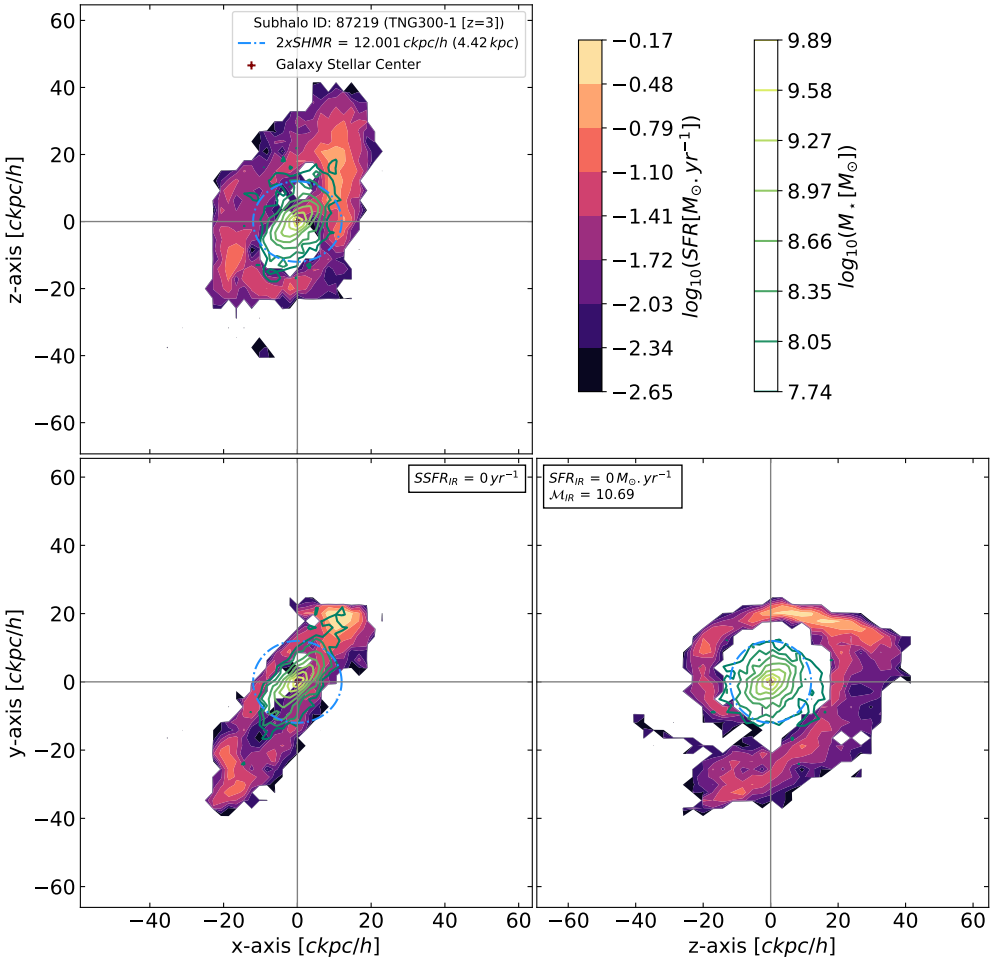


Figure A.1: Spatial comoving distributions within $10 \times SHMR$ of the star formation rate ($SFR$) (black-to-purple-to-yellow shaded areas) and of the galaxy stellar mass ($M_\star$) (green-to-yellow contour lines). The galaxy's stellar center of mass (red symbol) is taken as the origin of all three plots. The blue circle indicates the $2 \times SHMR$ perimeter. We also specify the total $SFR$, specific $SFR$ and galaxy stellar mass within $2 \times SHMR$.

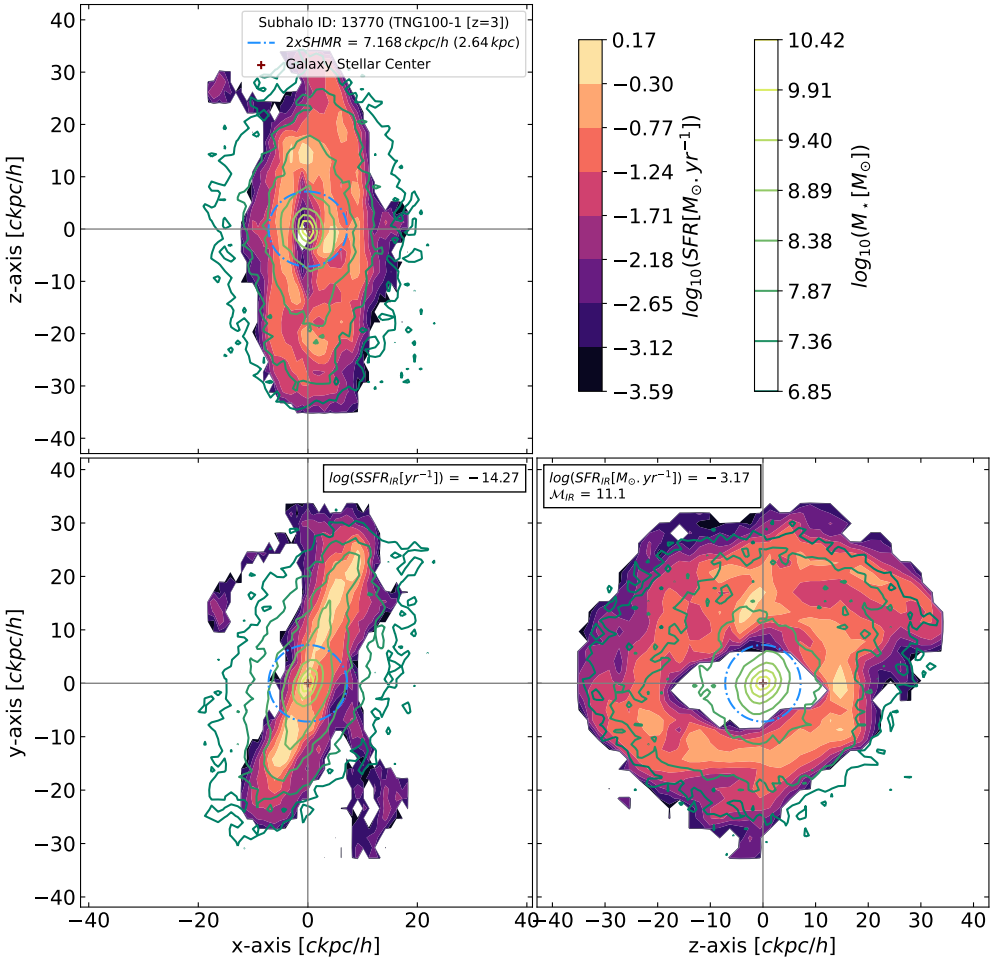


Figure A.2: Spatial comoving distributions within $10 \times SHMR$ of the star formation rate ($SFR$) (black-to-purple-to-yellow shaded areas) and of the galaxy stellar mass ($M_\star$) (green-to-yellow contour lines). The galaxy's stellar center of mass (red symbol) is taken as the origin of all three plots. The blue circle indicates the $2 \times SHMR$ perimeter. We also specify the total $SFR$, specific $SFR$ and galaxy stellar mass within $2 \times SHMR$.

# Appendix B

# Galaxy Stellar Mass Distribution of $sSFR$

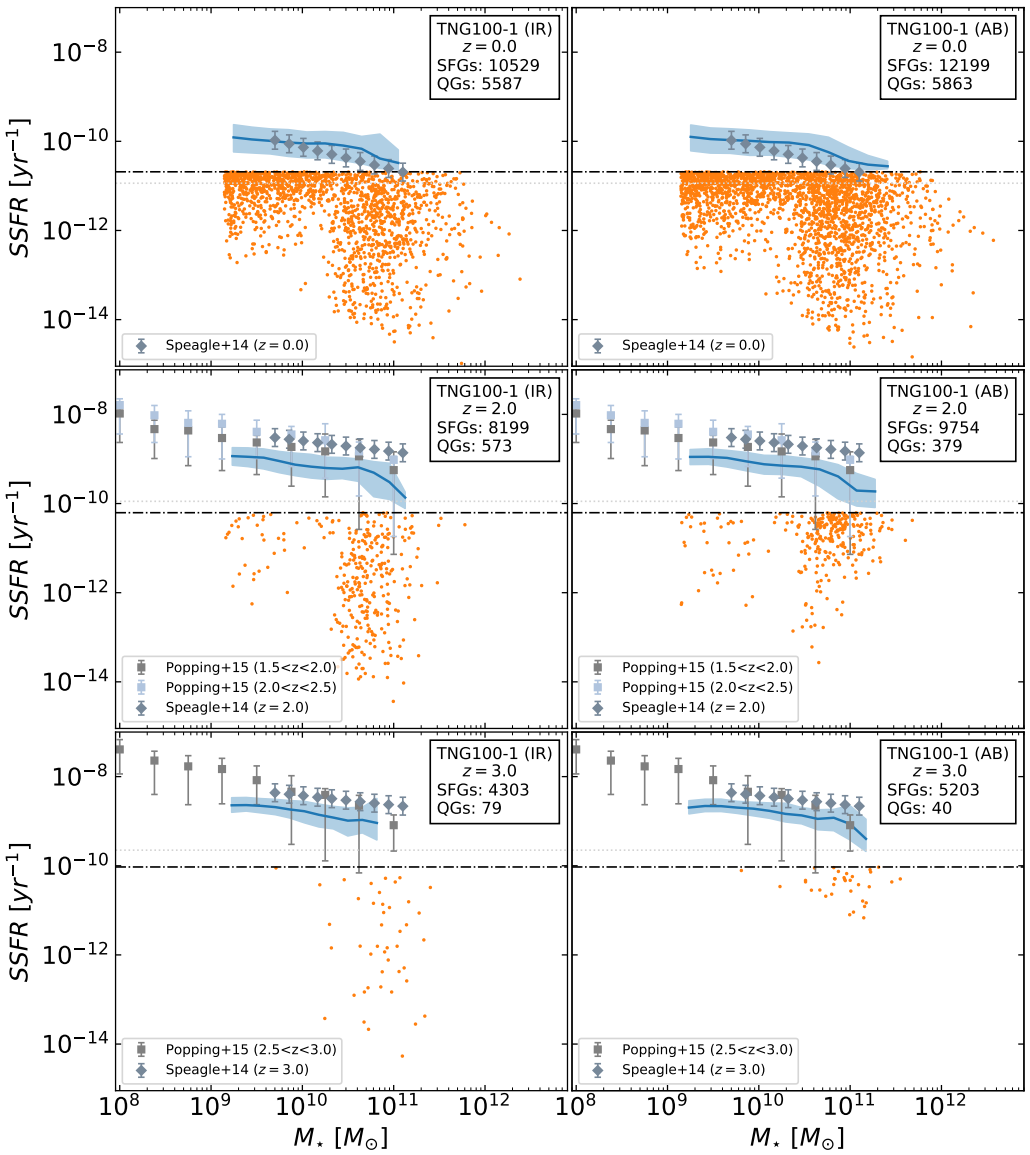


Figure B.1: Specific star formation rate $sSFR$ distribution as a function of the in-radius (left panels) and all-bound (right panels) galaxy stellar mass ($M_\star$). In these plots, we present the $z = 0$ (top panels), $z = 2$ (center panels) and $z = 3$ (bottom panels) TNG100-1 galaxies. For each redshift, we report the median (solid blue) and the $16/84^{th}$ percentile ranges (blue shaded area) of the IllustrisTNG main star-forming sequence and quiescent galaxies (orange dots). The adopted $0.3/t_H$ critical $sSFR$ and the Genel et al., 2018 critical $sSFR$ are represented as black dash-dotted lines and the grey dotted lines respectively. We also show the main star-forming sequence from Speagle et al., 2014 and Popping et al., 2015's $sSFR$ distribution.

# Bibliography


Schneider, P. (2015). *Extragalactic Astronomy and Cosmology: An Introduction.*

Oesch, P. A. et al. (Mar. 2016). "A Remarkably Luminous Galaxy at z=11.1 Measured with Hubble Space Telescope Grism Spectroscopy". In: 819.2, 129, p. 129. DOI: 10.3847/0004-637X/819/2/129. arXiv: 1603.00461 [astro-ph.GA].

Jiang, Linhua et al. (Jan. 2021). "Evidence for GN-z11 as a luminous galaxy at redshift 10.957". In: *Nature Astronomy* 5, pp. 256–261. DOI: 10.1038/s41550-020-01275-y. arXiv: 2012.06936 [astro-ph.HE].

Bouwens, R. J. et al. (Apr. 2015). "UV Luminosity Functions at Redshifts z $\sim$ 4 to z $\sim$ 10: 10,000 Galaxies from HST Legacy Fields". In: 803.1, 34, p. 34. DOI: 10.1088/0004-637X/803/1/34. arXiv: 1403.4295 [astro-ph.CO].

Kriek, Mariska et al. (Oct. 2006). "Spectroscopic Identification of Massive Galaxies at z ~2.3 with Strongly Suppressed Star Formation". In: 649.2, pp. L71–L74. DOI: 10.1086/508371. arXiv: astro-ph/0608446 [astro-ph].

Fontana, A. et al. (July 2009). "The fraction of quiescent massive galaxies in the early Universe". In: 501.1, pp. 15–20. DOI: 10.1051/0004-6361/200911650. arXiv: 0901.2898 [astro-ph.GA].

Muzzin, Adam et al. (Nov. 2013). "The Evolution of the Stellar Mass Functions of Star-forming and Quiescent Galaxies to z = 4 from the COSMOS/UltraVISTA Survey". In: 777.1, 18, p. 18. DOI: 10.1088/0004-637X/777/1/18. arXiv: 1303.4409 [astro-ph.CO].

Ilbert, O. et al. (Aug. 2013). "Mass assembly in quiescent and star-forming galaxies since z  4 from UltraVISTA". In: 556, A55, A55. DOI: 10.1051/0004-6361/201321100. arXiv: 1301.3157 [astro-ph.CO].

Martis, Nicholas S. et al. (Aug. 2016). "The Evolution of the Fractions of Quiescent and Star-forming Galaxies as a Function of Stellar Mass Since z = 3: Increasing Importance of Massive, Dusty Star-forming Galaxies in the Early Universe". In: 827.2, L25, p. L25. DOI: 10.3847/2041-8205/827/2/L25. arXiv: 1606.04090 [astro-ph.GA].

Fumagalli, Mattia et al. (Nov. 2014). "How Dead are Dead Galaxies? Mid-infrared Fluxes of Quiescent Galaxies at Redshift 0.3 < z < 2.5: Implications for Star Formation Rates and Dust Heating". In: 796.1, 35, p. 35. DOI: 10.1088/0004-637X/796/1/35. arXiv: 1308.4132 [astro-ph.CO].

van der Wel, A. et al. (June 2014). "3D-HST+CANDELS: The Evolution of the Galaxy Size-Mass Distribution since z = 3". In: 788.1, 28, p. 28. DOI: 10.1088/0004-637X/788/1/28. arXiv: 1404.2844 [astro-ph.GA].

Popping, G. et al. (Dec. 2015). "The inferred evolution of the cold gas properties of CANDELS galaxies at 0.5 < z < 3.0". In: 454.2, pp. 2258–2276. DOI: 10.1093/mnras/stv2136. arXiv: 1509.04720 [astro-ph.GA].

Santini, P. et al. (Feb. 2012). "The evolving slope of the stellar mass function at $0.6 \leqslant z < 4.5$ from deep WFC3 data". In: 538, A33, A33. DOI: 10.1051/0004-6361/201117513. arXiv: 1111.5728 [astro-ph.CO].

Barro, G. et al. (Aug. 2016). "Sub-kiloparsec ALMA Imaging of Compact Star-forming Galaxies at z ~2.5: Revealing the Formation of Dense Galactic Cores in the Progenitors of Compact Quiescent Galaxies". In: 827.2, L32, p. L32. DOI: 10.3847/2041-8205/827/2/L32. arXiv: 1607.01011 [astro-ph.GA].

Tasca, L. A. M. et al. (Sept. 2015). "The evolving star formation rate: $M_\star$ relation and sSFR since z  5 from the VUDS spectroscopic survey". In: 581, A54, A54. DOI: 10.1051/0004-6361/201425379. arXiv: 1411.5687 [astro-ph.GA].

Domínguez Sánchez, H. et al. (Oct. 2011). "The evolution of quiescent galaxies at high redshifts ($z \geqslant 1.4$)". In: 417.2, pp. 900–915. DOI: 10.1111/j.1365-2966.2011.19263.x. arXiv: 1106.3194 [astro-ph.CO].

Kajisawa, M. et al. (Sept. 2009). "MOIRCS Deep Survey. IV. Evolution of Galaxy Stellar Mass Function Back to z ~3". In: 702.2, pp. 1393–1412. DOI: 10.1088/0004-637X/702/2/1393. arXiv: 0907.0133 [astro-ph.CO].

Cheung, Edmond et al. (May 2016). "Suppressing star formation in quiescent galaxies with supermassive black hole winds". In: 533.7604, pp. 504–508. DOI: 10.1038/nature18006. arXiv: 1605.07626 [astro-ph.GA].

Kriek, Mariska et al. (Dec. 2016). "A massive, quiescent, population II galaxy at a redshift of 2.1". In: 540.7632, pp. 248–251. DOI: 10.1038/nature20570. arXiv: 1612.02001 [astro-ph.GA].

Belli, Sirio, Andrew B. Newman, and Richard S. Ellis (Jan. 2017). "MOSFIRE Spectroscopy of Quiescent Galaxies at $1.5 < z < 2.5$. I. Evolution of Structural and Dynamical Properties". In: 834.1, 18, p. 18. DOI: 10.3847/1538-4357/834/1/18. arXiv: 1608.00608 [astro-ph.GA].

Schreiber, C. et al. (Oct. 2018). "Near infrared spectroscopy and star-formation histories of $3 \leqslant z \leqslant 4$ quiescent galaxies". In: 618, A85, A85. DOI: 10.1051/0004-6361/201833070. arXiv: 1807.02523 [astro-ph.GA].

Belli, Sirio, Andrew B. Newman, and Richard S. Ellis (Mar. 2019). "MOSFIRE Spectroscopy of Quiescent Galaxies at $1.5 < z < 2.5$. II. Star Formation Histories and Galaxy Quenching". In: 874.1, 17, p. 17. DOI: 10.3847/1538-4357/ab07af. arXiv: 1810.00008 [astro-ph.GA].

Tanaka, Masayuki et al. (Nov. 2019). "Stellar Velocity Dispersion of a Massive Quenching Galaxy at $z = 4.01$". In: 885.2, L34, p. L34. DOI: 10.3847/2041-8213/ab4ff3. arXiv: 1909.10721 [astro-ph.GA].

Valentino, Francesco et al. (Feb. 2020). "Quiescent Galaxies 1.5 Billion Years after the Big Bang and Their Progenitors". In: 889.2, 93, p. 93. DOI: 10.3847/1538-4357/ab64dc. arXiv: 1909.10540 [astro-ph.GA].

Esdaile, James et al. (Feb. 2021). "Consistent Dynamical and Stellar Masses with Potential Light IMF in Massive Quiescent Galaxies at $3 < z < 4$ Using Velocity Dispersions Measurements with MOSFIRE". In: 908.2, L35, p. L35. DOI: 10.3847/2041-8213/abe11e. arXiv: 2010.09738 [astro-ph.GA].

Bezanson, Rachel et al. (June 2009). "The Relation Between Compact, Quiescent High-redshift Galaxies and Massive Nearby Elliptical Galaxies: Evidence for Hierarchical, Inside-Out Growth". In: 697.2, pp. 1290–1298. DOI: 10.1088/0004-637X/697/2/1290. arXiv: 0903.2044 [astro-ph.CO].

Newman, Andrew B. et al. (July 2010). "Keck Spectroscopy of z $>$ 1 Field Spheroidals: Dynamical Constraints on the Growth Rate of Red "Nuggets"". In: 717.2, pp. L103–L107. DOI: 10.1088/2041-8205/717/2/L103. arXiv: 1004.1331 [astro-ph.CO].

Belli, Sirio, Andrew B. Newman, and Richard S. Ellis (Mar. 2014). "Velocity Dispersions and Dynamical Masses for a Large Sample of Quiescent Galaxies at z $>$ 1: Improved Measures of the Growth in Mass and Size". In: 783.2, 117, p. 117. DOI: 10.1088/0004-637X/783/2/117. arXiv: 1311.3317 [astro-ph.CO].

Whitaker, Katherine E. et al. (Aug. 2010). "The Age Spread of Quiescent Galaxies with the NEWFIRM Medium-band Survey: Identification of the Oldest Galaxies Out to z ~2". In: 719.2, pp. 1715–1732. DOI: 10.1088/0004-637X/719/2/1715. arXiv: 1006.5453 [astro-ph.CO].

Vernet, J. et al. (Dec. 2011). "X-shooter, the new wide band intermediate resolution spectrograph at the ESO Very Large Telescope". In: 536, A105, A105. DOI: 10.1051/0004-6361/201117752. arXiv: 1110.1944 [astro-ph.IM].

Stockmann, Mikkel et al. (Jan. 2020). "X-shooter Spectroscopy and HST Imaging of 15 Massive Quiescent Galaxies at z $\gtrsim$ 2". In: 888.1, 4, p. 4. DOI: 10.3847/1538-4357/ab5af4. arXiv: 1912.01619 [astro-ph.GA].

Strateva, Iskra et al. (Oct. 2001). "Color Separation of Galaxy Types in the Sloan Digital Sky Survey Imaging Data". In: 122.4, pp. 1861–1874. DOI: 10.1086/323301. arXiv: astro-ph/0107201 [astro-ph].

van Dokkum, Pieter G. et al. (Dec. 2011). "First Results from the 3D-HST Survey: The Striking Diversity of Massive Galaxies at z $>$ 1". In: 743.1, L15, p. L15. DOI: 10.1088/2041-8205/743/1/L15. arXiv: 1108.6060 [astro-ph.CO].

Pacucci, Fabio et al. (June 2016). "First identification of direct collapse black hole candidates in the early Universe in CANDELS/GOODS-S". In: 459.2, pp. 1432–1439. DOI: 10.1093/mnras/stw725. arXiv: 1603.08522 [astro-ph.GA].

Bell, Eric F. et al. (Dec. 2003). "The Optical and Near-Infrared Properties of Galaxies. I. Luminosity and Stellar Mass Functions". In: 149.2, pp. 289–312. DOI: 10.1086/378847. arXiv: astro-ph/0302543 [astro-ph].

Budavári, Tamás et al. (Sept. 2003). "Angular Clustering with Photometric Redshifts in the Sloan Digital Sky Survey: Bimodality in the Clustering Properties of Galaxies". In: 595.1, pp. 59–70. DOI: 10.1086/377168. arXiv: astro-ph/0305603 [astro-ph].

Blanton, Michael R. et al. (Sept. 2003). "The Broadband Optical Properties of Galaxies with Redshifts 0.02$<$z$<$0.22". In: 594.1, pp. 186–207. DOI: 10.1086/375528. arXiv: astro-ph/0209479 [astro-ph].

Hogg, David W. et al. (Mar. 2003). "The Overdensities of Galaxy Environments as a Function of Luminosity and Color". In: 585.1, pp. L5–L9. DOI: 10.1086/374238. arXiv: astro-ph/0212085 [astro-ph].

Baldry, Ivan K. et al. (Jan. 2004b). "Quantifying the Bimodal Color-Magnitude Distribution of Galaxies". In: 600.2, pp. 681–694. DOI: 10.1086/380092. arXiv: astro-ph/0309710 [astro-ph].

Baldry, I. K. et al. (Dec. 2004a). "Color bimodality: Implications for galaxy evolution". In: *The New Cosmology: Conference on Strings and Cosmology*. Ed. by Roland E. Allen, Dimitri V.

Nanopoulos, and Christopher N. Pope. Vol. 743. American Institute of Physics Conference Series, pp. 106–119. DOI: 10.1063/1.1848322. arXiv: astro-ph/0410603 [astro-ph].

Cirasuolo, M. et al. (Sept. 2007). "The evolution of the near-infrared galaxy luminosity function and colour bimodality up to z ~= 2 from the UKIDSS Ultra Deep Survey Early Data Release". In: 380.2, pp. 585–595. DOI: 10.1111/j.1365-2966.2007.12038.x. arXiv: astro-ph/0609287 [astro-ph].

Glazebrook, Karl et al. (Apr. 2017). "A massive, quiescent galaxy at a redshift of 3.717". In: 544.7648, pp. 71–74. DOI: 10.1038/nature21680. arXiv: 1702.01751 [astro-ph.GA].

Santini, P. et al. (Nov. 2020). "The emergence of passive galaxies in the early Universe". In: *arXiv e-prints*, arXiv:2011.10584, arXiv:2011.10584. arXiv: 2011.10584 [astro-ph.GA].

Tully, R. B., J. R. Mould, and M. Aaronson (June 1982). "A color-magnitude relation for spiral galaxies". In: 257, pp. 527–537. DOI: 10.1086/160009.

Merlin, E. et al. (Jan. 2018). "Chasing passive galaxies in the early Universe: a critical analysis in CANDELS GOODS-South". In: 473.2, pp. 2098–2123. DOI: 10.1093/mnras/stx2385. arXiv: 1709.00429 [astro-ph.GA].

Girelli, Giacomo, Micol Bolzonella, and Andrea Cimatti (Dec. 2019). "Massive and old quiescent galaxies at high redshift". In: 632, A80, A80. DOI: 10.1051/0004-6361/201834547. arXiv: 1910.07544 [astro-ph.GA].

Merlin, E. et al. (Dec. 2019). "Red and dead CANDELS: massive passive galaxies at the dawn of the Universe". In: 490.3, pp. 3309–3328. DOI: 10.1093/mnras/stz2615. arXiv: 1909.07996 [astro-ph.GA].

Barrufet, Laia et al. (Mar. 2021). *Quiescent or dusty? Unveiling the nature of extremely red galaxies at z>3*. JWST Proposal. Cycle 1.

Nanayakkara, Themiya et al. (Mar. 2021). "Massive High-Redshift Quiescent Galaxies With JWST". In: *arXiv e-prints*, arXiv:2103.01459, arXiv:2103.01459. arXiv: 2103.01459 [astro-ph.GA].

Newman, Andrew B. et al. (Aug. 2018). "Resolving Quiescent Galaxies at z $\gtrsim$ 2. I. Search for Gravitationally Lensed Sources and Characterization of Their Structure, Stellar Populations, and Line Emission". In: 862.2, 125, p. 125. DOI: 10.3847/1538-4357/aacd4d. arXiv: 1806.06814 [astro-ph.GA].

Bruzual, G. and S. Charlot (Oct. 2003). "Stellar population synthesis at the resolution of 2003". In: 344.4, pp. 1000–1028. DOI: 10.1046/j.1365-8711.2003.06897.x. arXiv: astro-ph/0309134 [astro-ph].

Moustakas, John et al. (Apr. 2013). "PRIMUS: Constraints on Star Formation Quenching and Galaxy Merging, and the Evolution of the Stellar Mass Function from z = 0-1". In: 767.1, 50, p. 50. DOI: 10.1088/0004-637X/767/1/50. arXiv: 1301.1688 [astro-ph.CO].

McLeod, D. J. et al. (May 2021). "The evolution of the galaxy stellar-mass function over the last 12 billion years from a combination of ground-based and HST surveys". In: 503.3, pp. 4413–4435. DOI: 10.1093/mnras/stab731. arXiv: 2009.03176 [astro-ph.GA].

Davidzon, I. et al. (Sept. 2017). "The COSMOS2015 galaxy stellar mass function . Thirteen billion years of stellar mass assembly in ten snapshots". In: 605, A70, A70. DOI: 10.1051/0004-6361/201730419. arXiv: 1701.02734 [astro-ph.GA].

Mosleh, Moein et al. (Mar. 2017). "Connection between Stellar Mass Distributions within Galaxies and Quenching Since z = 2". In: 837.1, 2, p. 2. DOI: 10.3847/1538-4357/aa5f14. arXiv: 1702.02392 [astro-ph.GA].

Tacchella, Sandro et al. (July 2017). "On the Evolution of the Central Density of Quiescent Galaxies". In: 844.1, L1, p. L1. DOI: 10.3847/2041-8213/aa7cfb. arXiv: 1707.00695 [astro-ph.GA].

van Dokkum, Pieter G. et al. (Nov. 2015). "Forming Compact Massive Galaxies". In: 813.1, 23, p. 23. DOI: 10.1088/0004-637X/813/1/23. arXiv: 1506.03085 [astro-ph.GA].

Sherman, Sydney et al. (Dec. 2020). "Investigating the growing population of massive quiescent galaxies at cosmic noon". In: 499.3, pp. 4239–4260. DOI: 10.1093/mnras/staa3167. arXiv: 2010.04741 [astro-ph.GA].

Martig, Marie et al. (Dec. 2009). "Morphological Quenching of Star Formation: Making Early-Type Galaxies Red". In: 707.1, pp. 250–267. DOI: 10.1088/0004-637X/707/1/250. arXiv: 0905.4669 [astro-ph.CO].

Peng, Ying-jie et al. (Sept. 2010). "Mass and Environment as Drivers of Galaxy Evolution in SDSS and zCOSMOS and the Origin of the Schechter Function". In: 721.1, pp. 193–221. DOI: 10.1088/0004-637X/721/1/193. arXiv: 1003.4747 [astro-ph.CO].

Ichikawa, Akie and Yoshiki Matsuoka (July 2017). "Recently Quenched Galaxies at z = 0.2-4.8 in the COSMOS UltraVISTA Field". In: 843.1, L7, p. L7. DOI: 10.3847/2041-8213/aa78f8. arXiv: 1706.03438 [astro-ph.GA].

Querejeta, M. et al. (Apr. 2016). "Gravitational torques imply molecular gas inflow towards the nucleus of M 51". In: 588, A33, A33. DOI: 10.1051/0004-6361/201527536. arXiv: 1510.03440 [astro-ph.GA].

Mendel, J. Trevor et al. (Aug. 2020). "The Kinematics of Massive Quiescent Galaxies at 1.4 $<$ z $<$ 2.1: Dark Matter Fractions, IMF Variation, and the Relation to Local Early-type Galaxies". In: 899.1, 87, p. 87. DOI: 10.3847/1538-4357/ab9ffc. arXiv: 2006.13949 [astro-ph.GA].

Vogelsberger, Mark et al. (Oct. 2014). "Introducing the Illustris Project: simulating the coevolution of dark and visible matter in the Universe". In: 444.2, pp. 1518–1547. DOI: 10.1093/mnras/stu1536. arXiv: 1405.2921 [astro-ph.CO].

Genel, Shy et al. (Nov. 2014). "Introducing the Illustris project: the evolution of galaxy populations across cosmic time". In: 445.1, pp. 175–200. DOI: 10.1093/mnras/stu1654. arXiv: 1405.3749 [astro-ph.CO].

Sijacki, Debora et al. (Sept. 2015). "The Illustris simulation: the evolving population of black holes across cosmic time". In: 452.1, pp. 575–596. DOI: 10.1093/mnras/stv1340. arXiv: 1408.6842 [astro-ph.GA].

Schaye, Joop et al. (Jan. 2015). "The EAGLE project: simulating the evolution and assembly of galaxies and their environments". In: 446.1, pp. 521–554. DOI: 10.1093/mnras/stu2058. arXiv: 1407.7040 [astro-ph.GA].

Furlong, M. et al. (Feb. 2017). "Size evolution of normal and compact galaxies in the EAGLE simulation". In: 465.1, pp. 722–738. DOI: 10.1093/mnras/stw2740. arXiv: 1510.05645 [astro-ph.GA].

Davé, Romeel et al. (June 2019). "SIMBA: Cosmological simulations with black hole growth and feedback". In: 486.2, pp. 2827–2849. DOI: 10.1093/mnras/stz937. arXiv: 1901.10203 [astro-ph.GA].

Pillepich, Annalisa et al. (Jan. 2018b). "Simulating galaxy formation with the IllustrisTNG model". In: 473.3, pp. 4077–4106. DOI: 10.1093/mnras/stx2656. arXiv: 1703.02970 [astro-ph.GA].

Pillepich, Annalisa et al. (Mar. 2018a). "First results from the IllustrisTNG simulations: the stellar mass content of groups and clusters of galaxies". In: 475.1, pp. 648–675. DOI: 10.1093/mnras/stx3112. arXiv: 1707.03406 [astro-ph.GA].

Springel, Volker et al. (Mar. 2018). "First results from the IllustrisTNG simulations: matter and galaxy clustering". In: 475.1, pp. 676–698. DOI: 10.1093/mnras/stx3304. arXiv: 1707.03397 [astro-ph.GA].

Nelson, Dylan et al. (Mar. 2018). "First results from the IllustrisTNG simulations: the galaxy colour bimodality". In: 475.1, pp. 624–647. DOI: 10.1093/mnras/stx3040. arXiv: 1707.03395 [astro-ph.GA].

Naiman, Jill P. et al. (June 2018). "First results from the IllustrisTNG simulations: a tale of two elements - chemical evolution of magnesium and europium". In: 477.1, pp. 1206–1224. DOI: 10.1093/mnras/sty618. arXiv: 1707.03401 [astro-ph.GA].

Marinacci, Federico et al. (Nov. 2018). "First results from the IllustrisTNG simulations: radio haloes and magnetic fields". In: 480.4, pp. 5113–5139. DOI: 10.1093/mnras/sty2206. arXiv: 1707.03396 [astro-ph.CO].

Rodríguez Montero, Francisco et al. (Dec. 2019). "Mergers, starbursts, and quenching in the SIMBA simulation". In: 490.2, pp. 2139–2154. DOI: 10.1093/mnras/stz2580. arXiv: 1907.12680 [astro-ph.GA].

Weinberger, Rainer et al. (Sept. 2018). "Supermassive black holes and their feedback effects in the IllustrisTNG simulation". In: 479.3, pp. 4056–4072. DOI: 10.1093/mnras/sty1733. arXiv: 1710.04659 [astro-ph.GA].

Planck Collaboration et al. (Sept. 2016). "Planck 2015 results. XIII. Cosmological parameters". In: 594, A13, A13. DOI: 10.1051/0004-6361/201525830. arXiv: 1502.01589 [astro-ph.CO].

Springel, Volker (Jan. 2010). "E pur si muove: Galilean-invariant cosmological hydrodynamical simulations on a moving mesh". In: 401.2, pp. 791–851. DOI: 10.1111/j.1365-2966.2009.15715.x. arXiv: 0901.4107 [astro-ph.CO].

Springel, Volker et al. (Dec. 2001). "Populating a cluster of galaxies - I. Results at [formmu2]z=0". In: 328.3, pp. 726–750. DOI: 10.1046/j.1365-8711.2001.04912.x. arXiv: astro-ph/0012055 [astro-ph].

Rodriguez-Gomez, Vicente et al. (May 2015). "The merger rate of galaxies in the Illustris simulation: a comparison with observations and semi-empirical models". In: 449.1, pp. 49–64. DOI: 10.1093/mnras/stv264. arXiv: 1502.01339 [astro-ph.GA].

Donnari, Martina et al. (June 2019). "The star formation activity of IllustrisTNG galaxies: main sequence, UVJ diagram, quenched fractions, and systematics". In: 485.4, pp. 4817–4840. DOI: 10.1093/mnras/stz712. arXiv: 1812.07584 [astro-ph.GA].

Springel, Volker and Lars Hernquist (Feb. 2003). "Cosmological smoothed particle hydrodynamics simulations: a hybrid multiphase model for star formation". In: 339.2, pp. 289–311. DOI: 10.1046/j.1365-8711.2003.06206.x. arXiv: astro-ph/0206393 [astro-ph].

Kennicutt Robert C., Jr. (Jan. 1998). "Star Formation in Galaxies Along the Hubble Sequence". In: 36, pp. 189–232. DOI: 10.1146/annurev.astro.36.1.189. arXiv: astro-ph/9807187 [astro-ph].

Chabrier, Gilles (July 2003). "Galactic Stellar and Substellar Initial Mass Function". In: 115.809, pp. 763–795. DOI: 10.1086/376392. arXiv: astro-ph/0304382 [astro-ph].

Nelson, Dylan et al. (Dec. 2019). "First results from the TNG50 simulation: galactic outflows driven by supernovae and black hole feedback". In: 490.3, pp. 3234–3261. DOI: 10.1093/mnras/stz2306. arXiv: 1902.05554 [astro-ph.GA].

Genel, Shy et al. (Mar. 2018). "The size evolution of star-forming and quenched galaxies in the IllustrisTNG simulation". In: 474.3, pp. 3976–3996. DOI: 10.1093/mnras/stx3078. arXiv: 1707.05327 [astro-ph.GA].

Rodriguez-Gomez, Vicente et al. (Mar. 2019). "The optical morphologies of galaxies in the IllustrisTNG simulation: a comparison to Pan-STARRS observations". In: 483.3, pp. 4140–4159. DOI: 10.1093/mnras/sty3345. arXiv: 1809.08239 [astro-ph.GA].

Schechter, P. (Jan. 1976). "An analytic expression for the luminosity function for galaxies." In: 203, pp. 297–306. DOI: 10.1086/154079.

Baldry, I. K., K. Glazebrook, and S. P. Driver (Aug. 2008). "On the galaxy stellar mass function, the mass-metallicity relation and the implied baryonic mass function". In: 388.3, pp. 945–959. DOI: 10.1111/j.1365-2966.2008.13348.x. arXiv: 0804.2892 [astro-ph].

Bernardi, M. et al. (Nov. 2013). "The massive end of the luminosity and stellar mass functions: dependence on the fit to the light profile". In: 436.1, pp. 697–704. DOI: 10.1093/mnras/stt1607. arXiv: 1304.7778 [astro-ph.CO].

Baldry, I. K. et al. (Mar. 2012). "Galaxy And Mass Assembly (GAMA): the galaxy stellar mass function at z $<$ 0.06". In: 421.1, pp. 621–634. DOI: 10.1111/j.1365-2966.2012.20340.x. arXiv: 1111.5707 [astro-ph.CO].

Speagle, J. S. et al. (Oct. 2014). "A Highly Consistent Framework for the Evolution of the Star-Forming "Main Sequence" from z ~0-6". In: 214.2, 15, p. 15. DOI: 10.1088/0067-0049/214/2/15. arXiv: 1405.2041 [astro-ph.GA].

Ellison, S. L., D. R. Patton, and R. C. Hickox (July 2015). "Galaxy pairs in the Sloan Digital Sky Survey - XII. The fuelling mechanism of low-excitation radio-loud AGN." In: 451, pp. L35–L39. DOI: 10.1093/mnrasl/slv061. arXiv: 1504.06255 [astro-ph.GA].

Franx, Marijn et al. (Dec. 2008). "Structure and Star Formation in Galaxies out to z = 3: Evidence for Surface Density Dependent Evolution and Upsizing". In: 688.2, pp. 770–788. DOI: 10.1086/592431. arXiv: 0808.2642 [astro-ph].

Huang, Kuang-Han et al. (Mar. 2017). "Relations between the Sizes of Galaxies and Their Dark Matter Halos at Redshifts 0 $<$ z $<$ 3". In: 838.1, 6, p. 6. DOI: 10.3847/1538-4357/aa62a6. arXiv: 1701.04001 [astro-ph.GA].

Damen, M. et al. (Jan. 2011). "The SIMPLE Survey: Observations, Reduction, and Catalog". In: 727.1, 1, p. 1. DOI: 10.1088/0004-637X/727/1/1. arXiv: 1011.2764 [astro-ph.CO].

Hirschmann, Michaela et al. (Aug. 2014). "Cosmological simulations of black hole growth: AGN luminosities and downsizing". In: 442.3, pp. 2304–2324. DOI: 10.1093/mnras/stu1023. arXiv: 1308.0333 [astro-ph.CO].

Savorgnan, Giulia A. D. et al. (Jan. 2016). "Supermassive Black Holes and Their Host Spheroids. II. The Red and Blue Sequence in the $M_{BH}$-$M_{*,sph}$ Diagram". In: 817.1, 21, p. 21. DOI: 10.3847/0004-637X/817/1/21. arXiv: 1511.07437 [astro-ph.GA].

Arnouts, S. et al. (Jan. 2002). "Measuring the redshift evolution of clustering: the Hubble Deep Field South". In: 329.2, pp. 355–366. DOI: 10.1046/j.1365-8711.2002.04988.x. arXiv: astro-ph/0109453 [astro-ph].

Ilbert, O. et al. (Oct. 2006). "Accurate photometric redshifts for the CFHT legacy survey calibrated using the VIMOS VLT deep survey". In: 457.3, pp. 841–856. DOI: 10.1051/0004-6361:20065138. arXiv: astro-ph/0603217 [astro-ph].

Bell, Eric F. et al. (May 2005). "Toward an Understanding of the Rapid Decline of the Cosmic Star Formation Rate". In: 625.1, pp. 23–36. DOI: 10.1086/429552. arXiv: astro-ph/0502246 [astro-ph].

Bolzonella, M., J. M. Miralles, and R. Pelló (Nov. 2000). "Photometric redshifts based on standard SED fitting procedures". In: 363, pp. 476–492. arXiv: astro-ph/0003380 [astro-ph].

Labbé, Ivo et al. (May 2005). "IRAC Mid-Infrared Imaging of the Hubble Deep Field-South: Star Formation Histories and Stellar Masses of Red Galaxies at z>2". In: 624.2, pp. L81–L84. DOI: 10.1086/430700. arXiv: astro-ph/0504219 [astro-ph].

Wuyts, Stijn et al. (Jan. 2007). "What Do We Learn from IRAC Observations of Galaxies at $2 < z < 3.5$?" In: 655.1, pp. 51–65. DOI: 10.1086/509708. arXiv: astro-ph/0609548 [astro-ph].

Brammer, Gabriel B., Pieter G. van Dokkum, and Paolo Coppi (Oct. 2008). "EAZY: A Fast, Public Photometric Redshift Code". In: 686.2, pp. 1503–1513. DOI: 10.1086/591786. arXiv: 0807.1533 [astro-ph].

Kriek, Mariska et al. (July 2009). "An Ultra-Deep Near-Infrared Spectrum of a Compact Quiescent Galaxy at $z = 2.2$". In: 700.1, pp. 221–231. DOI: 10.1088/0004-637X/700/1/221. arXiv: 0905.1692 [astro-ph.CO].

Bruzual A., Gustavo and Stephane Charlot (Mar. 1993). "Spectral Evolution of Stellar Populations Using Isochrone Synthesis". In: 405, p. 538. DOI: 10.1086/172385.

Peng, Chien Y. et al. (July 2002). "Detailed Structural Decomposition of Galaxy Images". In: 124.1, pp. 266–293. DOI: 10.1086/340952. arXiv: astro-ph/0204182 [astro-ph].

Cappellari, Michele and Eric Emsellem (Feb. 2004). "Parametric Recovery of Line-of-Sight Velocity Distributions from Absorption-Line Spectra of Galaxies via Penalized Likelihood". In: 116.816, pp. 138–147. DOI: 10.1086/381875. arXiv: astro-ph/0312201 [astro-ph].

Cappellari, Michele (Apr. 2017). "Improving the full spectrum fitting method: accurate convolution with Gauss-Hermite functions". In: 466.1, pp. 798–811. DOI: 10.1093/mnras/stw3020. arXiv: 1607.08538 [astro-ph.GA].

Vazdekis, A. et al. (June 2010). "Evolutionary stellar population synthesis with MILES - I. The base models and a new line index system". In: 404.4, pp. 1639–1671. DOI: 10.1111/j.1365-2966.2010.16407.x. arXiv: 1004.4439 [astro-ph.CO].

Williams, Rik J. et al. (Feb. 2009). "Detection of Quiescent Galaxies in a Bicolor Sequence from Z = 0-2". In: 691.2, pp. 1879–1895. DOI: 10.1088/0004-637X/691/2/1879. arXiv: 0806.0625 [astro-ph].

Carnall, A. C. et al. (Nov. 2018). "Inferring the star formation histories of massive quiescent galaxies with BAGPIPES: evidence for multiple quenching mechanisms". In: 480.4, pp. 4379–4401. DOI: 10.1093/mnras/sty2169. arXiv: 1712.04452 [astro-ph.GA].

Whitaker, Katherine E. et al. (July 2011). "The NEWFIRM Medium-band Survey: Photometric Catalogs, Redshifts, and the Bimodal Color Distribution of Galaxies out to z ~3". In: 735.2, 86, p. 86. DOI: 10.1088/0004-637X/735/2/86. arXiv: 1105.4609 [astro-ph.CO].

Brammer, G. B. et al. (Nov. 2009). "The Dead Sequence: A Clear Bimodality in Galaxy Colors from z = 0 to z = 2.5". In: 706.1, pp. L173–L177. DOI: 10.1088/0004-637X/706/1/L173. arXiv: 0910.2227 [astro-ph.CO].

Calzetti, Daniela et al. (Apr. 2000). "The Dust Content and Opacity of Actively Star-forming Galaxies". In: 533.2, pp. 682–695. DOI: 10.1086/308692. arXiv: astro-ph/9911459 [astro-ph].

Leja, Joel, Sandro Tacchella, and Charlie Conroy (July 2019). "Beyond UVJ: More Efficient Selection of Quiescent Galaxies with Ultraviolet/Mid-infrared Fluxes". In: 880.1, L9, p. L9. DOI: 10.3847/2041-8213/ab2f8c. arXiv: 1907.02970 [astro-ph.GA].